



3 1176 01503 8814

N67-37199

THE **BOEING** COMPANY

CODE IDENT. NO. 81205

DOCUMENT NO. D2-100293 -1TITLE: PICTURE DATA SYSTEMS ANALYSISMODEL LUNAR ORBITER CONTRACT NO. NAS 1-3800

| | |
|-----------|-----------|
| ISSUE NO. | ISSUED TO |
|-----------|-----------|

LIBRARY COPY

DEC 4 - 1964

LANGLEY RESEARCH CENTER
LIBRARY, NASA
LANGLEY STATION
HAMPTON, VIRGINIA

Distribution of this report is provided in the interest of information exchange. Responsibility for the contents resides in the author or organization that prepared it.

PREPARED BY Electronics TechnologySUPERVISED BY J. A. Retka J. A. Retka Dec 7, 1964
ELECTRONICS TECHNOLOGYAPPROVED BY T. T. Yamauchi T. T. Yamauchi 12-9-64
SYSTEM ENGINEERING & TECHNOLOGY MANAGER

APPROVED BY _____

APPROVED BY J. A. Retka 12-9-64**BOEING**NO. D2-100293-1

SH.

Page 1

. LTR:

Contributions to the analyses of the Picture Data System included in this document have been made by:

| | |
|------------------|---|
| J. T. Andreika | Communications System |
| J. A. Barton | Radiation |
| R. E. Douglass | Transfer Functions, Optics, Image Smear |
| D. W. Exner, Jr. | Nominal System Analysis |
| R. E. Harris | G.R.E. |
| J. H. Lincoln | Photometry, Meteoroid Environment |

2-3142-2

TABLE OF CONTENTS

| | Page |
|---|------|
| 1.0 Nominal System End-to-End Analysis | 13 |
| 1.1 Block Diagram | 13 |
| 1.2 Assumptions | 14 |
| 1.3 Nominal System Performance | 14 |
| 1.3.1 Signal Analysis | 14 |
| 1.3.2 Noise Analysis | 20 |
| 1.3.3 Signal to Noise Ratio | 29 |
| 2.0 Off Nominal System Performance | 38 |
| 2.1 Effects of Off Nominal Values of Variables | 38 |
| 2.1.1 Variations in Exposure | 38 |
| 2.1.1.1 Variation Due to Target Characteristics | 38 |
| 2.1.1.2 Variations Due to Space Environment | 39 |
| 2.1.1.3 Variations Due to System Errors | 39 |
| 2.1.1.4 Effects of Exposure Variation on System Performance | 40 |
| 2.1.2 Off Nominal Variations in Transfer Functions | 42 |
| 2.1.3 Variations in Contrast Ratio | 51 |
| 2.1.4 Variation in Filter Characteristics | 52 |
| 2.1.5 Off Nominal Smear Conditions | 56 |
| 3.0 Contrast Ratio and Exposure | 58 |
| 3.1 Factors Affecting Surface Brightness | 58 |
| 3.1.1 Geometrical Effects | 58 |
| 3.1.2 Albedo | 60 |
| 3.2 Determination of Contrast Ratio | 64 |
| 3.3 Variations in Contrast Ratio | 67 |
| 3.3.1 Target Model Studies | 67 |
| 3.3.2 Lunar Surface Photometric Variations | 73 |

TABLE OF CONTENTS

(Continued)

| | Page |
|--|------|
| 4.0 Signal and Noise | 89 |
| 4.1 Transfer Functions | 93 |
| 4.2 Film Noise | 97 |
| 4.3 Filter Characteristics | 99 |
| 4.4 Communications System | 100 |
| 4.4.1 System Description | 100 |
| 4.4.1.1 Spacecraft | 100 |
| 4.4.1.2 Earth Terminal | 102 |
| 4.4.2 Signal Processing | 102 |
| 4.4.2.1 General | 102 |
| 4.4.2.2 Signal Processing in the Spacecraft | 104 |
| 4.4.2.3 R-F Link Performance | 107 |
| 4.4.2.4 Signal Processing in the Receiving Equipment | 108 |
| 4.4.3 Noise Effects | 110 |
| 4.4.3.1 Noise Sources | 110 |
| 4.4.3.2 Noise Processing | 114 |
| 4.4.4 System Performance | 114 |
| 4.4.4.1 Video Signal-to-noise Ratio | 114 |
| 4.4.4.2 Relative Output Noise Power Density | 115 |
| 4.4.4.3 Margin at the Demodulator Threshold | 116 |
| 4.4.4.4 Effect of Subcarrier Insertion Phase Error | 118 |
| 5.0 Image Smear | 122 |
| 6.0 Natural Environment | 123 |
| 6.1 Radiation | 123 |
| 6.1.1 Radiation Environment | 123 |
| 6.1.1.1 Geomagnetically Trapped Radiation | 123 |
| 6.1.1.2 Galactic Cosmic Radiation | 123 |
| 6.1.1.3 The Solar Wind | 123 |

TABLE OF CONTENTS

(Continued)

| | Page |
|---|------|
| 6.1.1.4 Solar Particle Event Radiation | 128 |
| 6.1.1.5 Solar Electromagnetic Radiation | 131 |
| 6.1.2 Radiation Dose to the Film | 131 |
| 6.1.3 Film Damage Criteria | 139 |
| 6.2 Meteoric Particles | 145 |
| 6.2.1 Flux of Particles Impacting the Moon | 145 |
| 6.2.2 Effects of Impacts | 150 |
| 6.2.3 Meteoroid Hazard to the Photographic System | 151 |
| 7.0 Monitoring Techniques | 150 |
| 7.1 Pre-Exposed Film Edge Data | 150 |
| 7.1.1 Resolving Power Bar Charts | 150 |
| 7.1.2 Gray Scale | 152 |
| 7.1.3 Linearity Marks | 152 |
| 7.1.4 Recovery Test Pattern | 153 |
| 7.1.5 Identification | 153 |
| 7.1.6 Reassembly Reference | 153 |
| 7.2 Time Track | 153 |
| 7.3 Telemetry Data | 164 |

ABSTRACT

An analysis of the Lunar Orbiter Picture Data System performance has been made for both nominal and off-nominal values of significant variables. Modulation transfer functions and signal-to-noise analysis of the individual and combined optical, photographic, and electronic components have been used to assess their characteristics and effects on the resolution capabilities of the system. Variables studied to provide the basis for determining their effects or limitations on the system include those related to orbital parameters, the lunar surface being photographed, the observational geometry, the environmental factors of ionizing radiation and meteoroid flux, and the communication link. Monitoring techniques for control and calibration of the photographs are described. These factors have been analyzed to establish the capability of the system to produce photographs of the specified resolution and quality. It is shown that 1 meter surface resolution specification can be met by the high resolution camera on-axis from the nominal altitude of 46 Km and a sun angle between 50° and 75°. Resolution will be degraded to less than 2 meters at the field edge. The low resolution requirement of 8 meter surface resolution will be met under favorable conditions.

KEY WORD LIST

Lunar Orbiter

Spacecraft

Moon

Lunar Surface

Photography

Cameras

Transfer Function

Resolution

Photometry

Albedo

Photometric Function

Signal/Noise Ratio

Communication

Telemetry

Image Motion Compensation

Image Smear

Target Model

Ground Reconstruction

Equipment

Scanner

Radiation

Solar Radiation

Radiation Dose

Meteoroid

Reconnaissance

Signal Analysis

LIST OF ILLUSTRATIONS

| FIGURE | TITLE | PAGE |
|----------|---|------|
| 1 | Lunar Orbiter Photographic System | 12 |
| 1.1-1 | Block Diagram | 15 |
| 1.3-1 | Lens-Film Response | 16 |
| 1.3-2 | Scanner Element Responses | 17 |
| 1.3-3 | Communications Subsystem Response | 18 |
| 1.3-4 | Over-all CRS Response | 19 |
| 1.3-5 | Densitometer Response | 21 |
| 1.3-6 | Readout Transmission vs. Log Exposure | 22 |
| 1.3-7 | Assumed Sensitometric Properties - Type 5374 Film | 23 |
| 1.3-8 | Signal vs. Lines per MM | 24 |
| 1.3-9 | Signal to Noise Ratio using Sine Wave Bars and 1/2 Meter Equivalent Aperture | 30 |
| 1.3-10 | Signal to Noise Ratio Using Square Wave Bars and 1/2 Meter Equivalent Aperture | 32 |
| 1.3-11 | Signal to Noise Ratio Using Sine Wave Bars and 1 Meter Equivalent Aperture | 33 |
| 1.3-12 | Signal to Noise Ratio using Square Wave Bars and 1 Meter Equivalent Aperture. | 34 |
| 2.1.1-1 | Readout Density vs. Exposure SO 243 Film, Bimat Processing | 41 |
| 2.1.2-1 | Eastman Kodak Specification to Pacific Optical: 24" E.L. Lens, SO 243 Film, D-19, 2/1 Contrast | 44 |
| 2.1.2-2 | 3" Lens Off-Axis Performance. | 45 |
| 2.1.2-3 | Postulated Off-Axis Transfer Functions for 24" Lens | 46 |
| 2.1.2-3a | Off-Axis Transfer Functions Computed from 24" Lens Formula | 47 |
| 2.1.2-4 | 24" Lens Measured Data, 2/1 Contrast. | 49 |
| 2.1.2-5 | Postulated MTF for 24" Lens when 0.002 Inch Out of Focus. | 50 |
| 2.1.4-1 | Variation of Phase with Frequency | 54 |
| 2.1.4-2 | System Edge Response for Various Group Delay Variations | 55 |
| 2.1.5-1 | Modulation Transfer Function for Off-Nominal Smear. | 57 |
| 3.1-1 | Photometric Function of Lunar Maria According to Fedorets | 59 |
| 3.1-2 | The Apparent Brightness of Different Details on the Lunar Surface as a Function of Phase Angle before and after Full Moon | 62 |
| 3.1-3 | Geometrical Relationships Affecting Surface Brightness | 63 |
| 3.3-1 | Variations in Relative Brightness with Off-Axis Line of Sight as a Function of Surface Slope and Sun Angle | 63 |

LIST OF ILLUSTRATIONS (Continued)

| FIGURE | TITLE | PAGE |
|--------|--|------|
| 3.3-2 | NASA Targets at Limiting Resolution | 69 |
| 3.3-3 | The Illumination of a Target Cone | 70 |
| 3.3-4 | Maximum-Minimum Contrast Ratio Across a 2 m. Base, 0.5 m. High Cone as a Function of Sun Angle | 71 |
| 3.3-5 | Contrast Ratio Across a 2 m. Base, 0.5 m. High Cone as a Function of Off-Axis Line of Sight, with Sun Angles of 50° and 75° | 72 |
| 3.3-6 | Distribution of Slopes on a Lunar Mare Area | 76 |
| 3.3-7 | Distribution of Slopes on a Lunar Upland Area | 77 |
| 3.3-8 | Distribution of Slopes on a Lunar Mare and an Upland Area. | 78 |
| 3.3-9 | Distribution of Slope Lengths of a Profile through Upland Area North of Ptolemaeus | 80 |
| 3.3-10 | Variation in Luminance of the Lunar Surface Along the Equator between 50° E. Long. and 70° W Long. with the Sub-Solar Point at 0° Lat., 0° Long. | 83 |
| 3.3-11 | Variation in Luminance of the Lunar Surface along the Equator. Sub-Solar Points at 0° Lat., 90° E. Long. and 0° Lat: 90° W. Long. | 84 |
| 3.3-12 | Distribution of Section Lengths in Luminance Profiles | 85 |
| 3.3-13 | Distribution of Luminance Ratios or Contrast Ratios between Adjacent Sections of Luminance Profile with Sun Angle between 50° and 75°. On Camera Axis at Nadir. | 87 |
| 4.1-1 | Image Spread Function of Airy Disc for an f/5.6 Optical System at 5500 Å | 91 |
| 4.1-2 | Modulation Transfer Function (Fourier Transform) of Diffraction Limited (Airy Spread Function) f/5.6 Optics at 5500 Å | 92 |
| 4.1-3 | Representation of Sine Wave Response Measurement. | 94 |
| 4.1-4 | Modulation Transfer Analysis of Signal through Processor and Minimum Modulation Required for Detection. | 96 |
| 4.4-1 | Block Diagram of Communications System: Spacecraft | 101 |
| 4.4-2 | Block Diagram of Communications System: Ground | 103 |
| 5.0-1 | Smear Budget. | 119 |
| 5.0-2 | Modulation Transfer Function for Image Smear. | 121 |

LIST OF ILLUSTRATIONS (Continued)

| FIGURE | TITLE | PAGE |
|--------|---|------|
| 6.1-1 | Integral Energy Spectrum of Primary Galactic Cosmic Radiation | 127 |
| 6.1-2 | Dose Point Coordinate System and Sector Angle Relations | 135 |
| 6.1-3 | Probability of Receiving a Cumulative Flux in 30 Days with J_0 | 138 |
| 6.1-4 | Radiation Effects in Eastman Kodak SO 243, Bimat Process | 140 |
| 6.1-5 | Radiation Effects in Eastman Kodak SO 243, Bimat Process, 53.5 Mev Protons. | 141 |
| 6.1-6 | Radiation Effects in Eastman Kodak SO 243, Bimat Process, 132.5 Mev Protons | 142 |
| 6.2-1 | Flux of Extraterrestrial Objects | 146 |
| 6.2-2 | Cumulative Frequency-Mass Distributions for Interplanetary Meteoric Particles | 147 |
| 6.2-3 | Ejecta from 28 Kilometer Per Second Impacts. Ratio of Ejected Mass to Impacting Particle Mass Above the Lunar Surface | 153 |
| 6.2-4 | Estimated Number of Particle Impacts per Day on Lens Area at Perilune Altitude of 46 Kilometers. | 155 |
| 6.2-5 | Percent of Lens Area Pitted per Day by Particle Impacts at Perilune | 156 |
| 6.2-6 | Percent of Lens Surface Pitted Per Day at Perilune as a Function of the Flux of Meteoric Particles | 157 |
| 7.1-1 | Edge Data Format. | 161 |

LIST OF TABLES

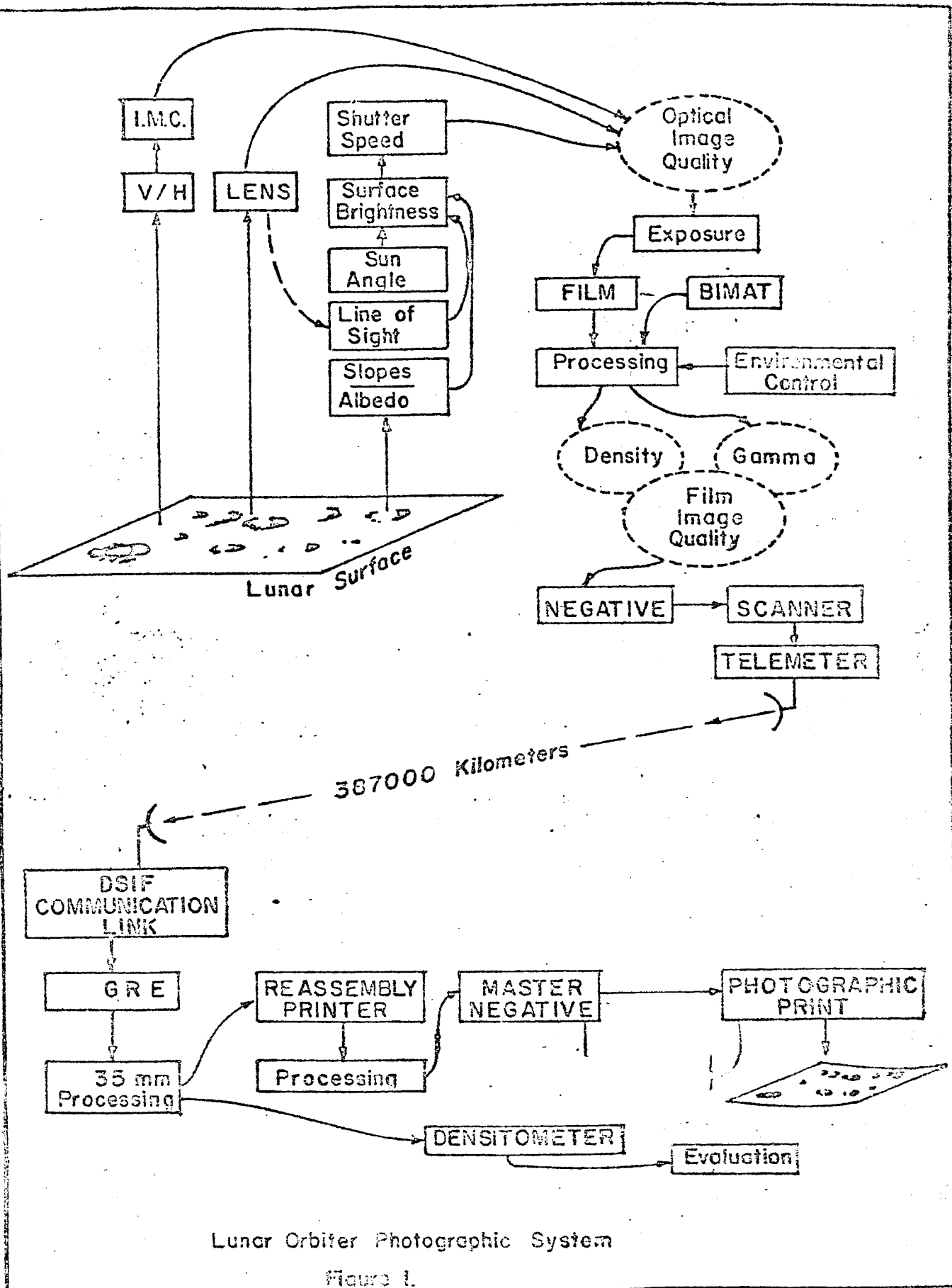
| <u>TABLE</u> | <u>TITLE</u> | <u>PAGE</u> |
|--------------|--|-------------|
| 1.3-1 | Calculated Signal Levels at Each Step in System, Sine Wave Bars, 1/2 m. Aperture | 25 |
| 1.3-2 | Calculated Signal Levels at Each Step in System, 1/2 m. Aperture | 28 |
| 1.3-3 | Fourier Components of Square Wave Test Bars, 1/2 m. Aperture. | 31 |
| 1.3-4 | System Signal Level for Sine Wave Bars, 1 m. Aperture. . . | 35 |
| 1.3-5 | System Noise Level, 1 m. Aperture. | 35 |
| 1.3-6 | Fourier Components of Square Wave Test Bars, 1 m. Aperture. | 36 |
| 3.1-1 | Normal Albedos of Lunar Areas. | 61 |
| 3.3-1 | Variations of Lunar Surface Brightness Ratios due to Off-Axis Line of Sight, as a Function of Slope and Sun Angles. | 65 |
| 3.3-2 | Effect of 6.6° Traverse on Surface Contrasts | 74 |
| 3.3-3 | Contrasts Due to Albedo Differences Across a 200 Km Traverse | 74 |
| 4.4-1 | R-F Link Parameters. | 107 |
| 4.4-2 | Frequency Interval | 115 |
| 6.1-1 | Lunar Orbiter Trajectories | 124 |
| 6.1-2 | Trapped Radiation Fluxes Encountered by the Lunar Orbiter | 125 |
| 6.1-3 | Flux of Cosmic Radiation Particles per M ² per Second with Energy Greater than E | 126 |
| 6.1-4 | Solar Wind Model | 129 |
| 6.1-5 | Peak Flux of Protons/cm ² Above 10 Mev and Corresponding Characteristic Rigidity P ₀ Solar Cycle 19 | 132 |
| 6.1-6 | Solar Alpha Particle Event Peak Fluxes. Solar Cycle 19. . | 133 |
| 6.1-7 | X-Ray Intensities. | 134 |
| 6.1-8 | Dose Table for Lunar Orbiter Trajectories. | 157 |
| 7.3-1 | Photo Subsystem Telemetry Points | 165 |

Preface

The function of the Picture Data System is to produce detailed photographs of specified areas of the lunar surface. The fidelity of the photographs and their suitability for extracting the required information are the primary measures of the system's capability. Its function requires formation of an image and its sequential translation into forms suitable for each step of the path extending from the lunar surface to the photograph being examined by an interpreter. This is shown schematically in Figure 1. Each translation and step imposes limitations on the amount and type of information, may modify or distort it, and may introduce spurious signals and noise.

This document examines the significant factors which influence performance of the picture data system, and assesses their effects on system capability. An analysis has been made of the operational characteristics of the system components under both nominal and off-nominal conditions. This provides the basis for establishing the limitations on the capabilities of the system to produce photographs of the specified resolution and quality. The first two Sections summarize the effects of variables; the first for nominal conditions and values of the variables, and the second for the off-nominal cases. The Sections which follow present the detailed analyses which are the basis for the system evaluation.

The analysis included in this document has been the responsibility of The Boeing Company. The contribution of basic data by Eastman Kodak and RCA on their respective subsystems is acknowledged.



Lunar Orbiter Photographic System

Figure 1.

U3 400 2000 REV. 3/64

REV 5/64

NO. D2-100293-1

PAGE

23

1.0

Nominal System End-to-End Analysis

The image of the lunar surface may be considered as a signal which is received by the camera collecting optics, imaged on film and subsequently converted into forms compatible with transmission to and reconstruction by the ground equipment. Since no element or function can attain absolute fidelity of output to input signal, a progressive degradation of the signal occurs as it passes through the system. The elements in the data chain may alter or distort the signal and they may introduce spurious values, or noise.

The relationship between the signal and noise is of major concern, since differentiation between the two is essential to the transfer of useful information. The signal to noise ratio, then, becomes a major criterion in defining the capabilities of a system to transmit useful information. This section contains an analysis of the signal and noise relationships throughout the system under nominal conditions.

1.1

Block Diagram

Because the system operations are, in general, sequential, the signal changes and noise contributions usually are additive. Transfer functions, which are quantitative expressions of the effect of a system element on the signal, provide a means of examining signal progress through the system and the individual and combined effects of the elements. For the purpose of analysis, the target may be considered to consist of a series of bars varying sinusoidally in brightness, with constant peak amplitude, but varying in spatial frequency. Ideally, the system should respond with a signal of constant peak amplitude over the range of frequencies presented. In practice, however, the signal amplitude will be modulated as some function of the frequency, usually decreasing with increasing frequency. This is, to simplify, the transfer function. In addition, noise is added to the signal as it passes through the system.

A block diagram representing the signal and noise flow of the Picture Data System is shown in Figure 1.1-1. The clear blocks represent those components or functions whose effects can be expressed as transfer functions. The hatched blocks represent sources of noise within the system. The Smear and Kell factor blocks do not represent physical hardware, but are functions having a determinable effect on the system capability. The densitometer is not a part of the Picture Handling System, but is used in the analysis of the photographs to provide quantitative evaluation in place of subjective visual assessment.

Assumptions

The following assumptions are made:

- Scene contrast ratio is 3:1 This corresponds to an initial signal modulation of 0.50.
- The film is exposed to an average density of 0.8 in the vicinity of the center of the field.
- Smear is negligible

1.3

Nominal System Performance

The nominal system performance is based upon the system with design values for those parameters that are subject to variation. Variations in these parameters from nominal are analyzed in Section 2.0. Data given is for the on-axis only. Off-axis conditions are analyzed in Section 2.1.2.

1.3.1

Signal Analysis

The signal analysis through the system is presented in terms of modulation transfer functions (MTF). An MTF can be determined for each element of the system and for the total system. A review of the meaning of the modulation transfer function is given in Section 4.1.

Figure 1.3-1 shows the combined lens-film transfer function. The data is from the Eastman Kodak Technical Proposal for Lunar Orbiter Project and represents laboratory measurements.

Figure 1.3-2 shows the transfer functions of the contributing parts of the scanner, i.e., spot and scan lens (combined) and video amplifier. Included in the video amplifier response curve are 12 db pre-emphasis with a first break point of 20 kcps and the filter characteristics required to achieve total photo subsystem roll-off of -25 db at 270 kcps and -40 db at 390 kcps.

Figure 1.3-3 shows the data link transfer function.

Figure 1.3-4 shows the various components of the GRS² transfer function including the Kell factor. The Kell factor is a statistical function derived from sampling theory as applied to the quantization of information in the direction perpendicular to the scan lines. The MTF includes the de-emphasis network to

* GRS - Ground Reconstruction System
GRE - Ground Reconstruction Equipment

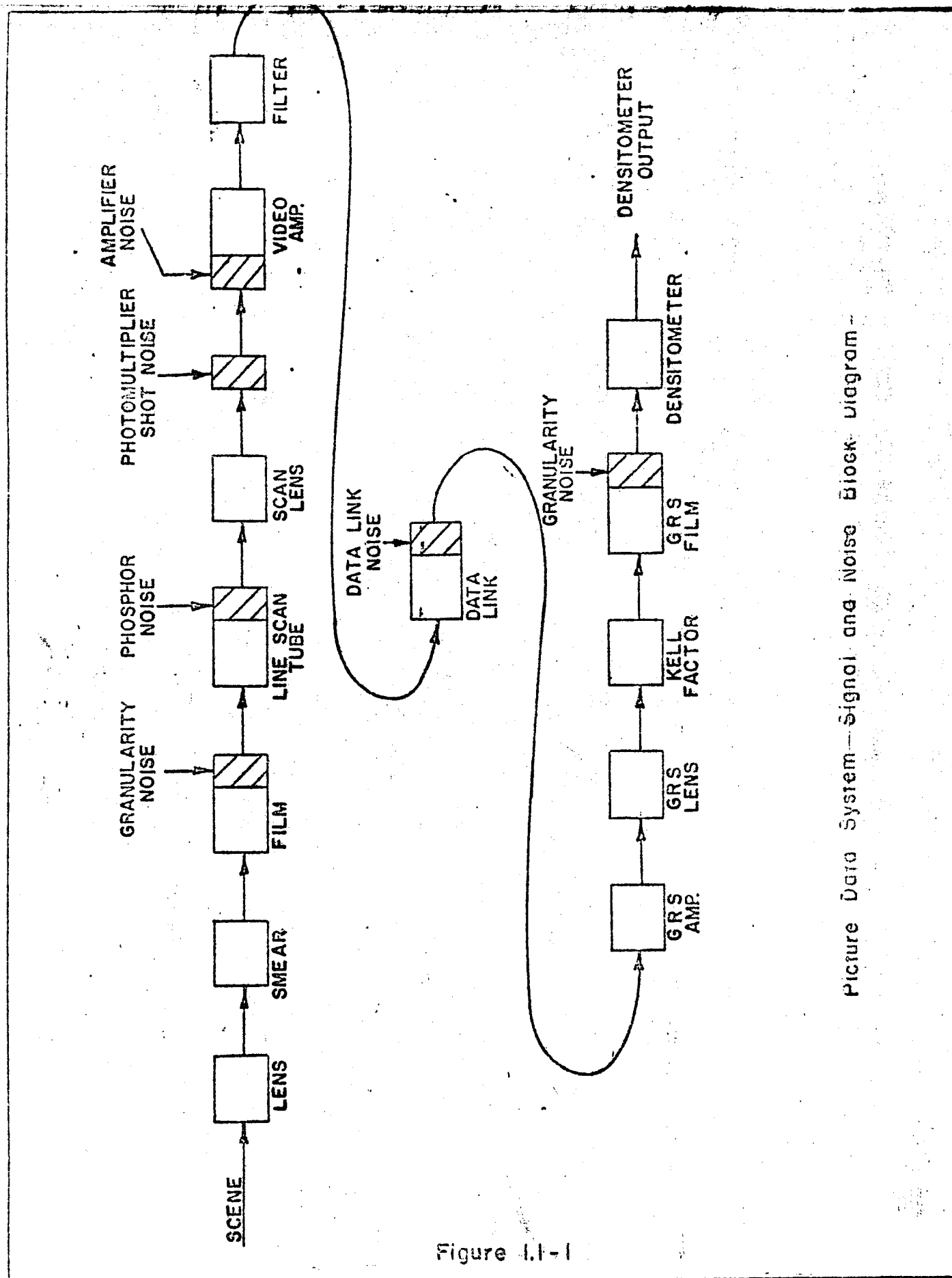
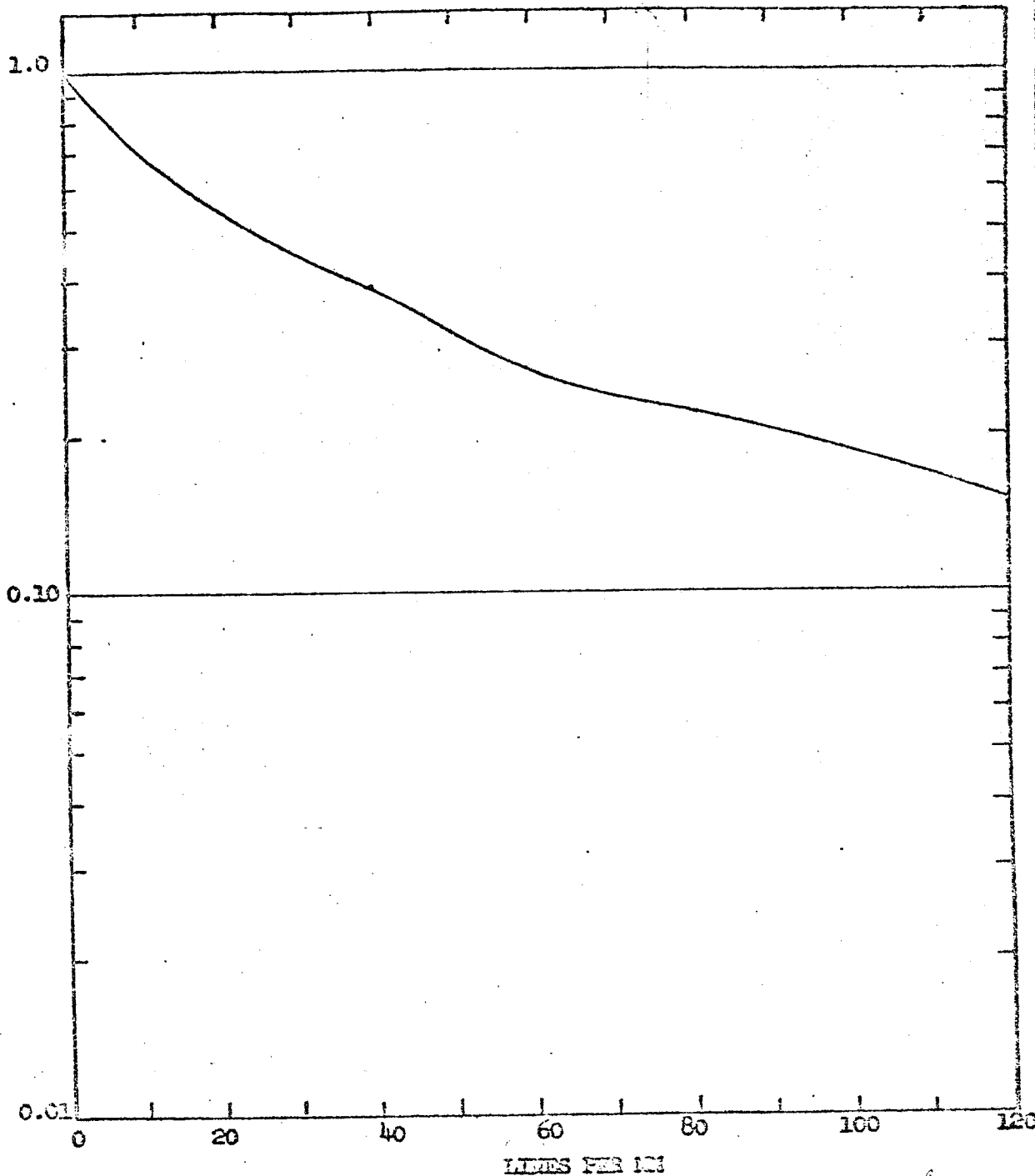


Figure I.1-1

Picture Data System—Signal and Noise Block Diagram

TRANSFER FUNCTIONS $T(N)$



LENS-FILM RESPONSE

FIGURE 1.3-1

US 4233 2000 REV. 2/64

REV SYM _____

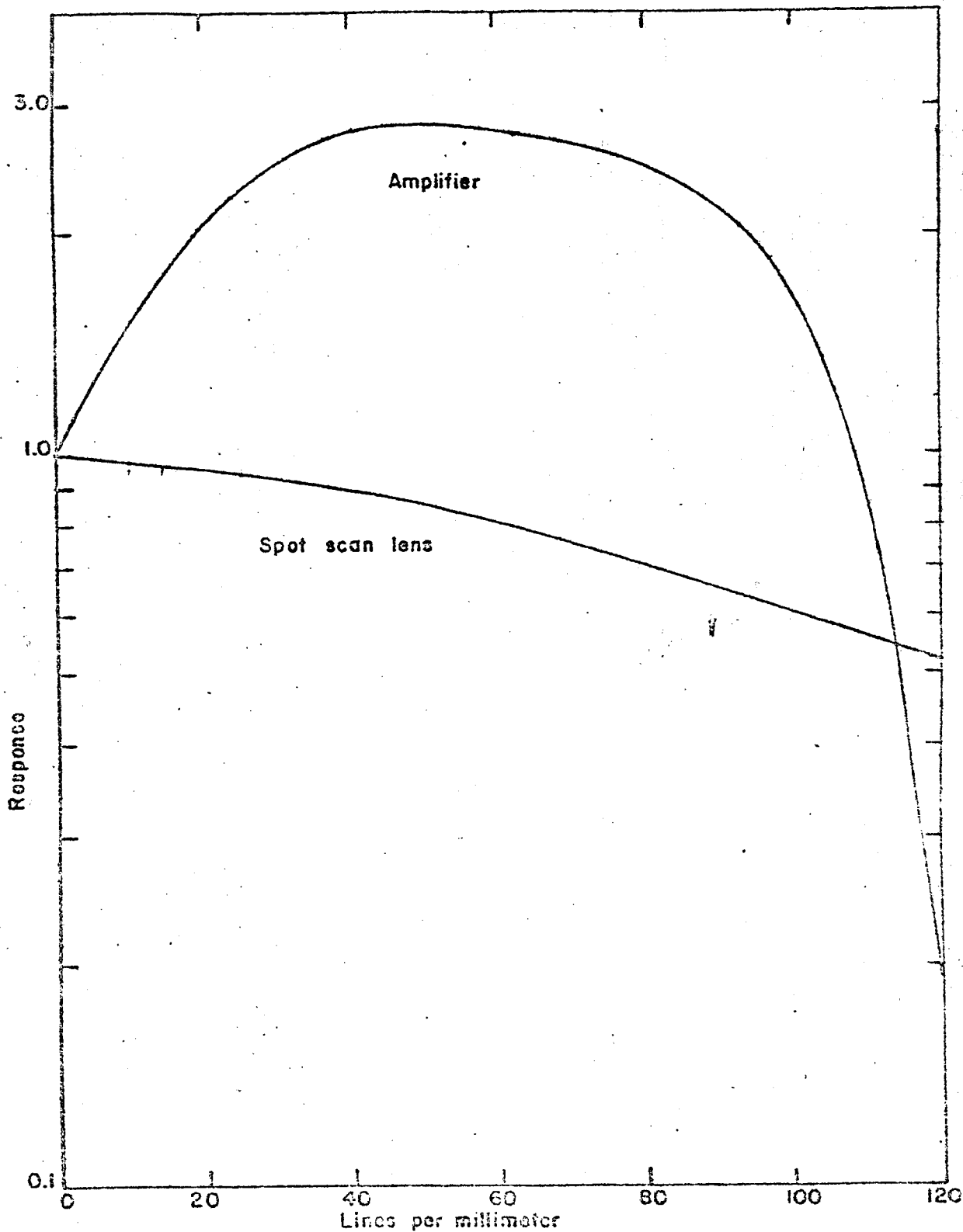
~~SECRET~~

NO.

D2-100293-1

PAGE

15



SCANNER ELEMENT RESPONSES

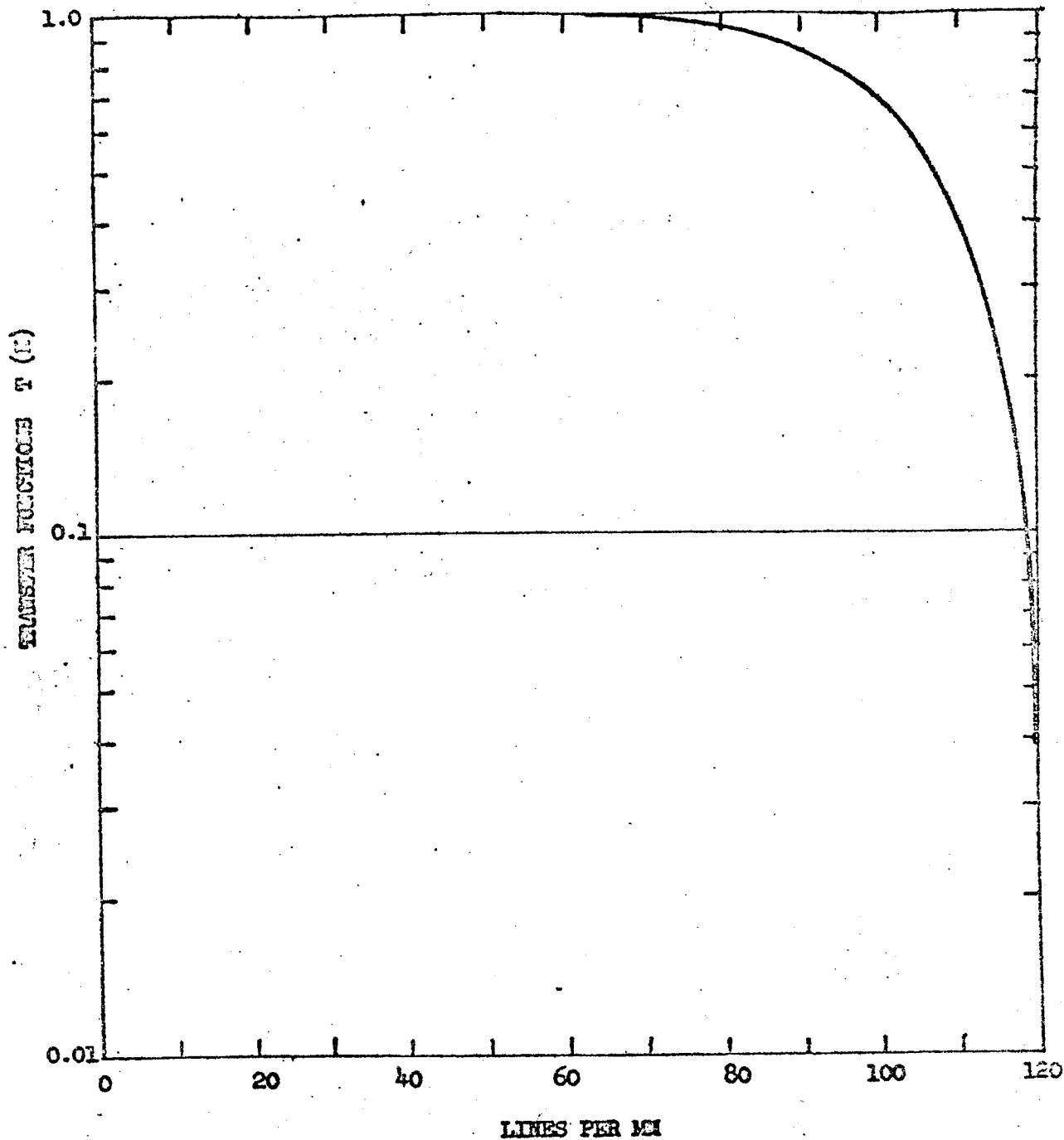
Figure 1.3-2

US 4183 2000 REV. 2/64

REV SYM

NO. D2-100093-1

PAGE 17



COMMUNICATIONS SUBSYSTEM RESPONSE

FIGURE 1.3-3

U3 4263 2000 REV. 2/62

T-5142-1

REV SYM _____

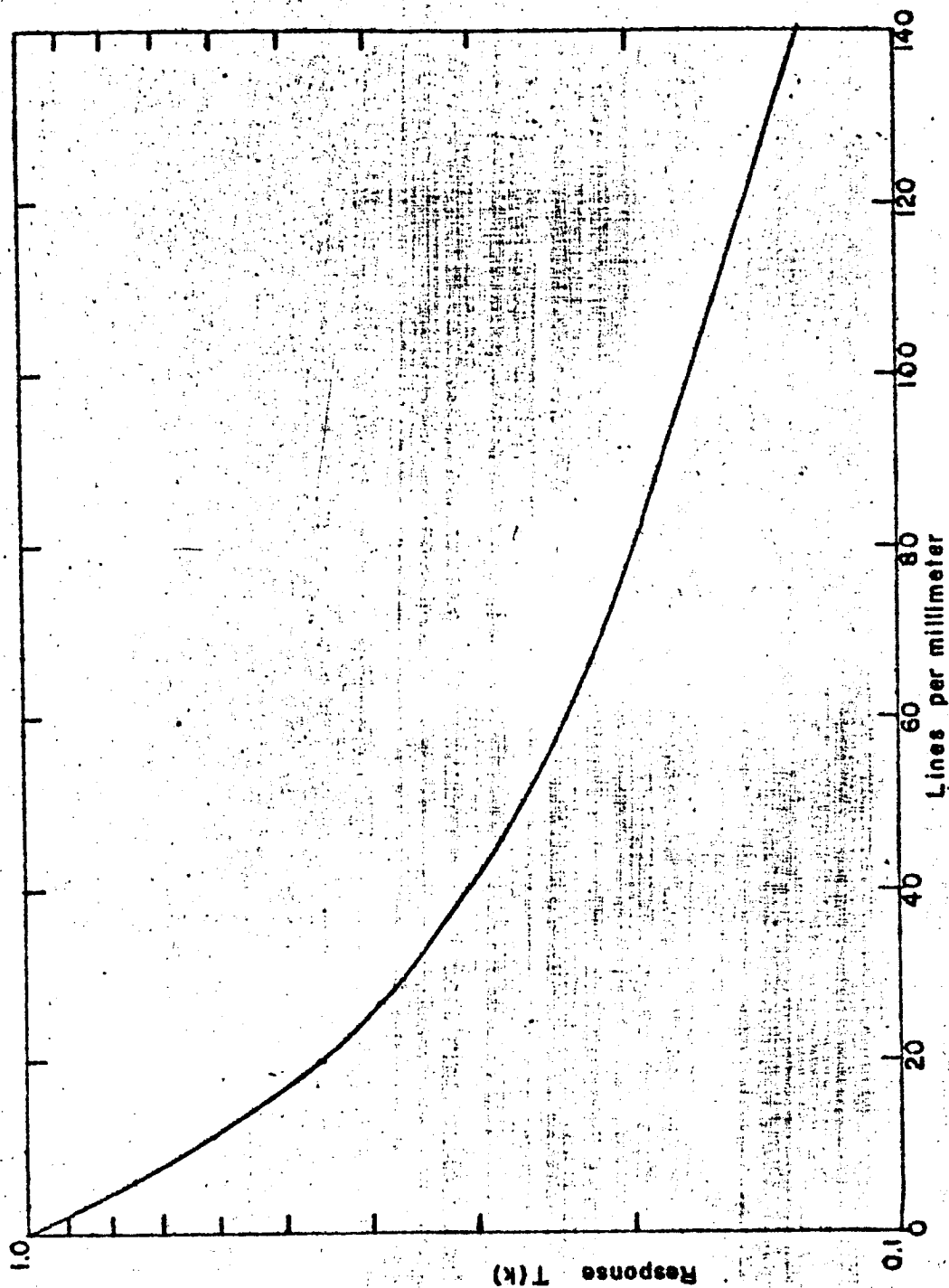
BOEING

NO.

D2-100293-1

SECT.

PAGE 18



Over-all GRS response.

Figure 1.3-4

1.3.1

(Continued)

compensate for the pre-emphasis in the spacecraft. Figure 1.3-5 shows the transfer function of the densitometer.

In using these response functions to permit tracing the actual signal through the system under nominal conditions, it is necessary to convert into the proper terms at each state; e.g., from percent modulation to log E; to transmission on the film; to volts for the scanner, data link, and GRE response; to exposure (at the kinescope) for the GRS film; to transmission for the densitometer; and to volts at the densitometer output.

Figure 1.3-6 shows the relationship for converting from illumination (E) to transmission for the spacecraft film. Figure 1.3-7 shows the conversion from illumination to transmission for the GRE film.

Table 1.3-1 shows the calculated signal levels at each step as the signal is traced through the system. The scanner and densitometer responses are given in volts per unit transmission and have the dimension of volts.

Figure 1.3-8 shows the signal levels at the photo subsystem output and at the densitometer output.

1.3.2

Noise Analysis

The noise analysis is performed on the basis of noise density² spectra in order to assess the effects of transfer functions of the portions of the data link which follow the noise sources. All noises are assumed to be gaussian, or "white" at their sources as shown by their location in Figure 1.1-1. The exception to this is the phosphor noise. This actually consists of two components; beam current fluctuations and phosphor granularity and non-uniformity.

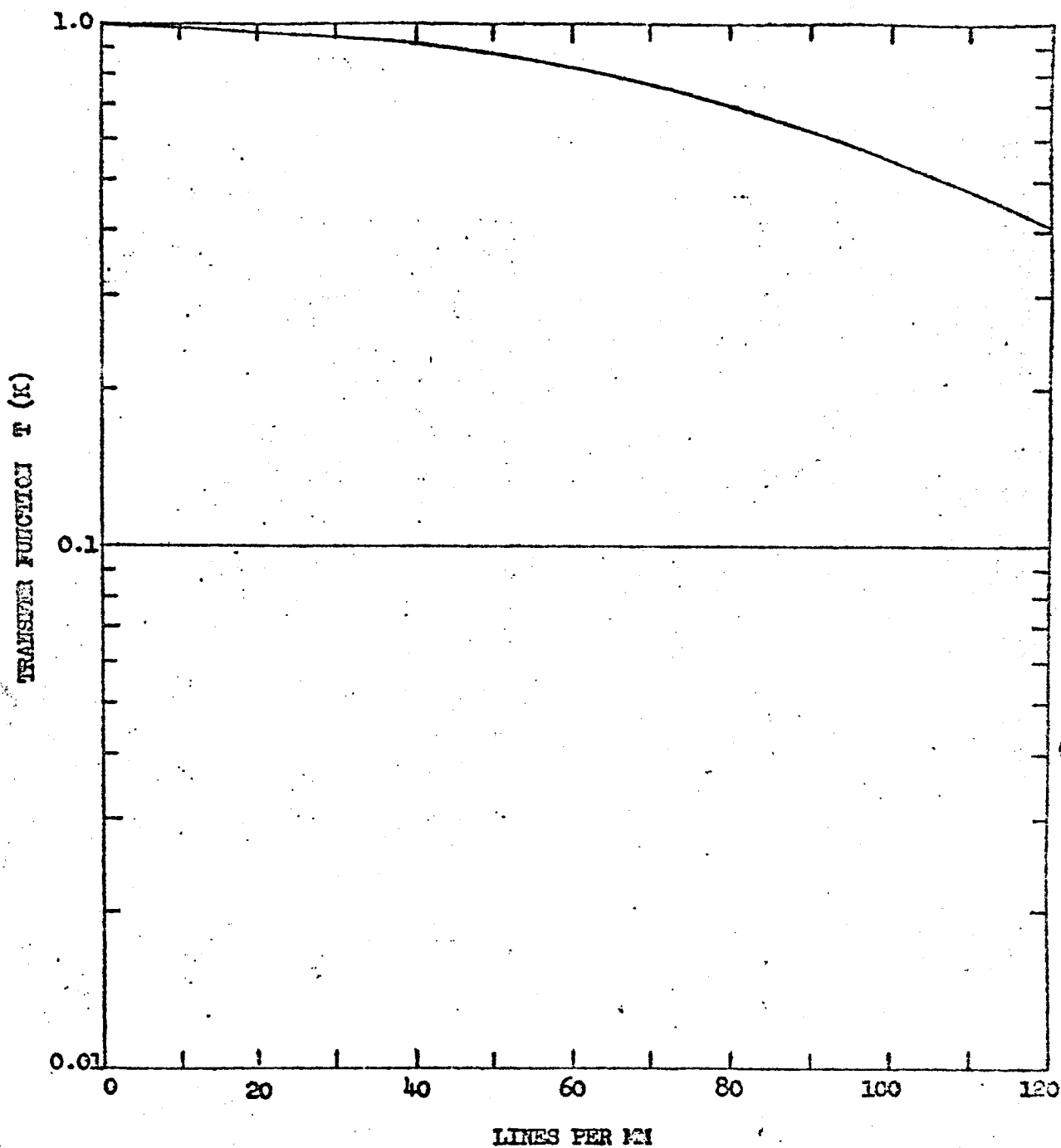
The division of this noise is not known at this time; therefore, it is assumed to all be due to beam current fluctuations. In any event, the contribution of this noise source to the RMS total is negligible.

The RMS granularity noise of the spacecraft film is calculated from the empirical formula:

$$\sigma(D) = .07 (D - 0.15)^{.428}$$

This formula applies for measurements made with a microdensitometer with an aperture diameter of 5 microns. Assuming the power density spectrum of the noise is flat (Stulz and Zweig) and assuming an ideal densitometer with response as shown in Figure 1.3-5, the noise density is 0.56% (1/mm) $\frac{1}{2}$ in terms of density.

*The noise density spectra is the distribution of noise as a function of frequency. Units are volts/(lines/mm)^{1/2}.



DENSITOMETER RESPONSE

FIGURE 1.3-5

U3 4208 2000 REV. 8/62

2-5142-2

REV SYM. _____

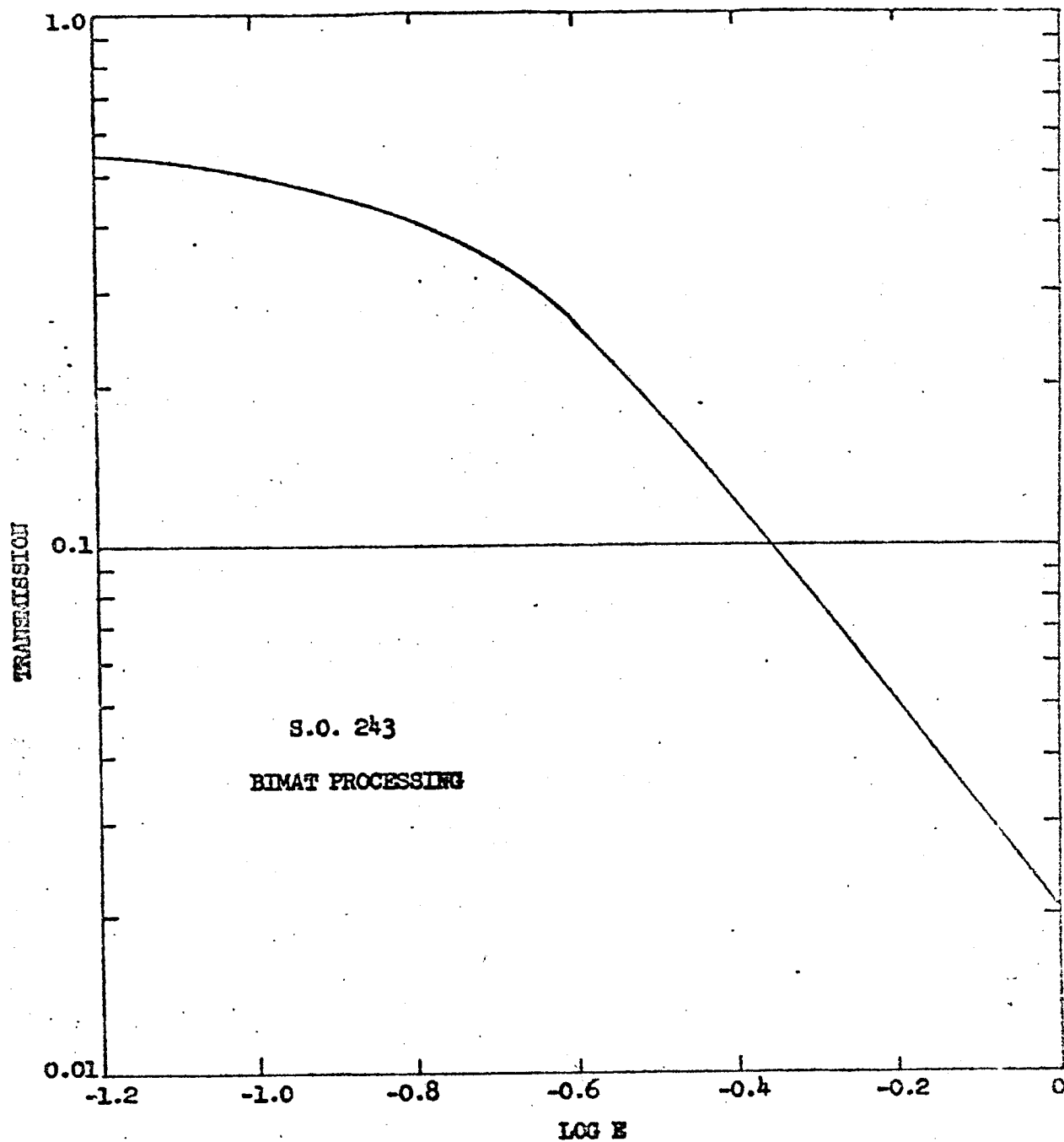
BOEING

NO. D2-100293-1

SECT. _____

PAGE 21

20



READOUT TRANSMISSION VERSUS LOG EXPOSURE

FIGURE 1.3-6

U3 4253 2000 REV. 2/64

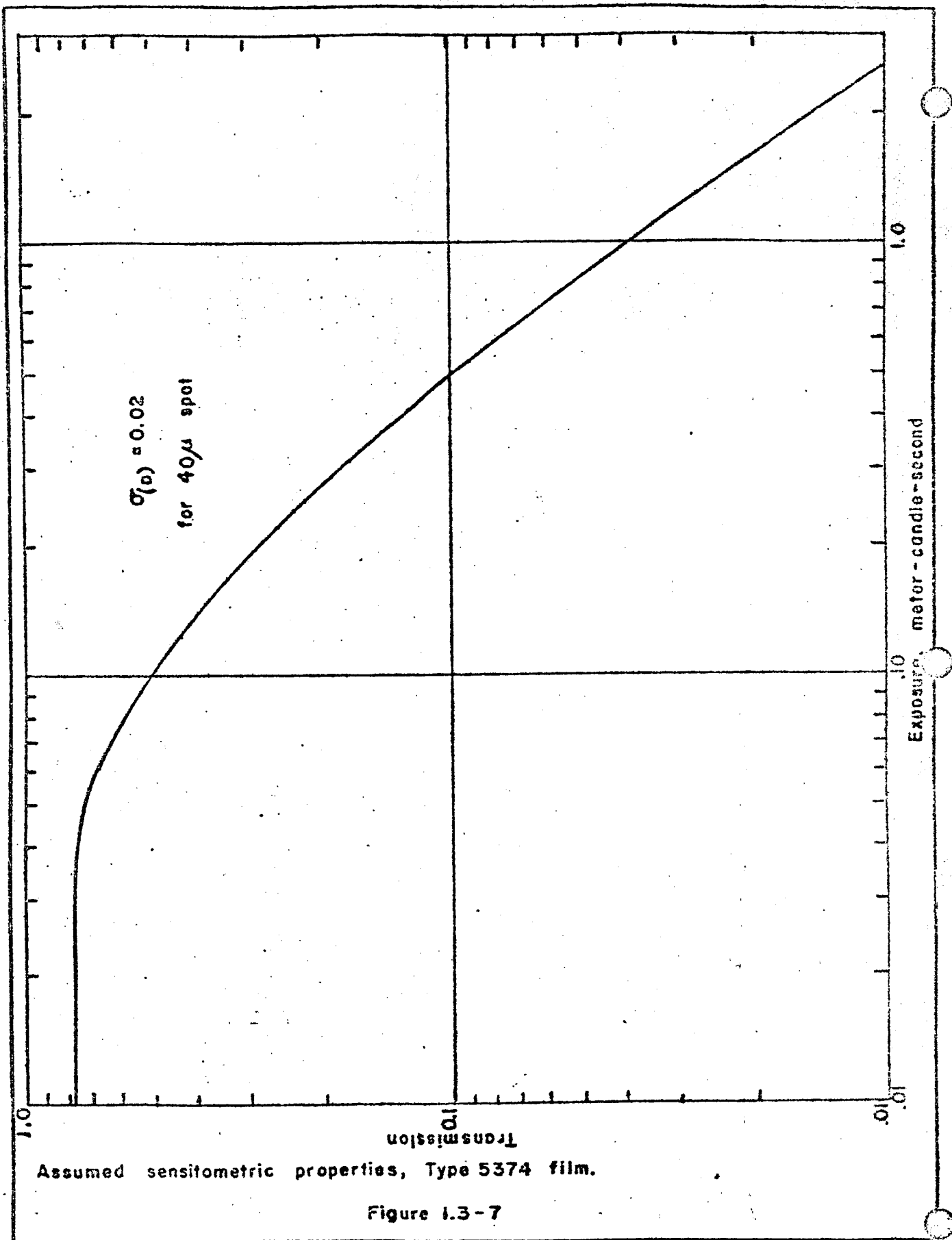
REV SYM _____

DOING

NO. D2-100293 -1

PAGE

22



U3 4258 2000 REV. 6/62

2-5142-2

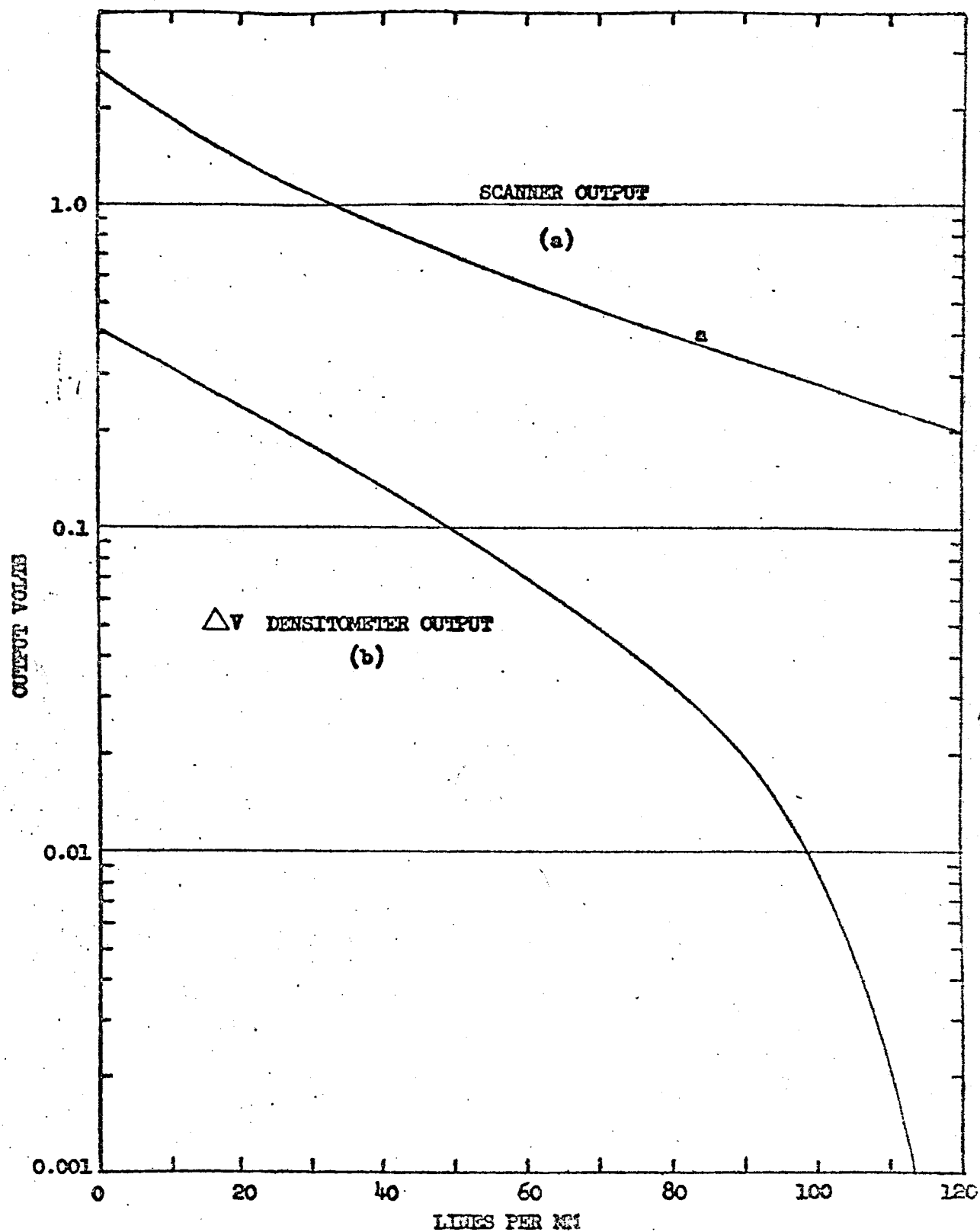
REV SYM _____

BOEING

NO. D2-100293-1

SECT.

PAGE 23



SIGNAL VERSUS LINES PER MM

FIGURE 1.3-8

U3 4208 2000 REV. 9/82

2-5142-2

REV SYM _____

BOEING

NO.

D2-100293-1

SECT.

PAGE 24

Calculated Signal Levels at Each Step in System, 1/2 M Effective Aperture

| PAYLOAD FILM | | PRIMARY RECORD | | | | | | |
|--|--|----------------|--------|--------|--------|--------|---------------|--------|
| $D_o = 0.8$ | | $D_o = 0.75$ | | | | | $M_o = 0.500$ | |
| | | 0 | 20 | 40 | 60 | 80 | 100 | 120 |
| | | lines/mm | | | | | | |
| LENS - FILM RESPONSE | | 1.000 | .544 | .388 | .265 | .224 | .186 | .150 |
| IMAGE MODULATION = M | | .500 | .272 | .194 | .133 | .112 | .093 | .075 |
| $\Delta \text{ LOGE}^+ = \text{LOG} (1 + M)$ | | .1761 | .1045 | .0770 | .0542 | .0461 | .0386 | .0314 |
| $\Delta \text{ LOGE}^- = \text{LOG} (1 - M)$ | | -.3010 | -.1379 | -.0937 | -.0620 | -.0516 | -.0424 | -.0339 |
| LOGE^+ | | -.286 | -.358 | -.385 | -.408 | -.416 | -.423 | -.431 |
| LOGE^- | | -.763 | -.600 | -.556 | -.524 | -.514 | -.504 | -.496 |
| T^+ | | .074 | .102 | .115 | .127 | .131 | .137 | .140 |
| T^- | | .387 | .262 | .228 | .204 | .196 | .189 | .183 |
| ΔT^- | | -.058 | -.057 | -.044 | -.032 | -.028 | -.022 | -.019 |
| ΔT^+ | | .228 | .103 | .069 | .045 | .037 | .030 | .024 |
| SCANNER RESPONSE | | 8.929 | 8.483 | 7.884 | 7.233 | 6.375 | 5.483 | 4.643 |
| ΔV^- SCANNER OUTPUT | | -.759 | -.484 | -.348 | -.231 | -.179 | -.120 | -.089 |
| ΔV^+ SCANNER OUTPUT | | 2.040 | .874 | .544 | .325 | .246 | .165 | .111 |
| FILTER RESPONSE | | 1.000 | 1.000 | 1.000 | 1.000 | .944 | .707 | .056 |
| ΔV^- FILTER OUTPUT | | -.759 | -.484 | -.348 | -.231 | -.169 | -.085 | -.005 |
| ΔV^+ FILTER OUTPUT | | 2.040 | .874 | .544 | .325 | .223 | .116 | .005 |
| COMMUNICATIONS SUBSYSTEM RESPONSE | | 1.000 | 1.000 | 1.000 | 1.000 | .944 | .707 | .039 |
| ΔV^- COMMUNICATIONS SUBSYSTEM RESPONSE | | -.759 | -.484 | -.348 | -.231 | -.159 | -.060 | 0 |
| ΔV^+ COMMUNICATIONS SUBSYSTEM RESPONSE | | 2.040 | .874 | .544 | .325 | .210 | .083 | 0 |
| GRS RESPONSE | | 1.000 | 1.000 | .941 | .837 | .714 | .635 | .573 |
| ΔV^- GRS INPUT | | -.759 | -.484 | -.328 | -.194 | -.114 | -.038 | 0 |
| ΔV^+ GRS INPUT | | 2.040 | .874 | .511 | .273 | .150 | .053 | 0 |
| ΔE^+ GRS INPUT | | .450 | .193 | .113 | .060 | .033 | .011 | 0 |
| ΔE^- GRS INPUT | | -.168 | -.107 | -.072 | -.043 | -.025 | -.008 | 0 |

TABLE 1.3-1

DOEING VOL
SEC.

NO 12-100293-1
PAGE 25

| | 0 | 20 | 40 | 60 | 80 | 100 | 120 | UNIT |
|---------------------------|-------|------|------|------|------|------|------|-------|
| E ⁺ GRS INPUT | .757 | .500 | .420 | .367 | .340 | .318 | .307 | MCS |
| E ⁻ GRS INPUT | .139 | .200 | .235 | .264 | .282 | .299 | .307 | MCS |
| T ⁺ GRS OUTPUT | .056 | .097 | .123 | .148 | .161 | .174 | .182 | |
| T ⁻ GRS OUTPUT | .385 | .283 | .240 | .214 | .199 | .186 | .182 | |
| △ T GRS OUTPUT | .329 | .186 | .117 | .066 | .038 | .012 | .000 | |
| DENSITOMETER RESPONSE | 1.000 | .974 | .913 | .818 | .690 | .554 | .402 | VOLES |
| △ V DENSITOMETER OUTPUT | .329 | .181 | .107 | .054 | .026 | .007 | 0 | VOLES |

TABLE 1.3-1 (Continued)

~~SECRET~~ VOL
SEC

NO D2-100293
PAGE 26

1.3.2

(Continued)

Since

$$D = \log \frac{1}{T}$$

Then

$$\frac{dT}{dD} = 2.3026T = \frac{2.3026}{\log^{-1} D} = .3649$$

and the noise density in terms of transmission is $.204 \text{ } \mu\text{V}/(1/\text{m})^2$.

The granularity noise density of the GRS film is calculated in a similar manner. Table 1.3-2 shows the calculated noise density at each step and the RMS value of the noise. For the purpose of calculations, the pre-emphasis and de-emphasis are assumed to result only in a reduction of the communications subsystem noise.

| PAYLOAD FILM | PRIMARY RECORD | | | | | | | |
|--|----------------|--------|--------|--------|--------|--------|--------|-----------------------|
| $D_0 = 0.8$ | $D_0 = 0.75$ | | | | | | | |
| | 0 | 20 | 40 | 60 | 80 | 100 | 120 | UNIT |
| | | | | | | | | lines/mm |
| SCANNER RESPONSE | 8.929 | 8.483 | 7.884 | 7.233 | 6.375 | 5.483 | 4.643 | mv |
| FILM NOISE AT SCANNER OUTPUT | 18.3 | 17.3 | 16.1 | 14.8 | 13.0 | 11.2 | 9.5 | $\frac{mv}{(1/mm)^2}$ |
| PHOSPHOR NOISE | 1.4 | 1.3 | 1.2 | 1.1 | 1.0 | .9 | .7 | |
| SHOT NOISE | | | | 0.8 | | | | |
| AMPLIFIER NOISE | | | | 0.7 | | | | |
| TOTAL NOISE AT SCANNER OUTPUT | 18.3 | 17.3 | 16.1 | 14.9 | 13.1 | 11.3 | 9.6 | |
| FILTER RESPONSE | 1.00 | 1.00 | 1.00 | 1.00 | .944 | .707 | .056 | |
| TOTAL NOISE AT FILTER OUTPUT | 18.3 | 17.3 | 16.1 | 14.9 | 12.4 | 8.0 | 0.5 | $\frac{mv}{(1/mm)^2}$ |
| COMMUNICATIONS SUBSYSTEM RESPONSE | 1.00 | 1.00 | 1.00 | 1.00 | .944 | .707 | .039 | |
| PHOTO SUBSYSTEM NOISE AT COMMUNICATIONS OUTPUT | 18.3 | 17.3 | 16.1 | 14.9 | 11.6 | 5.6 | 0.0 | $\frac{mv}{(1/mm)^2}$ |
| COMMUNICATIONS SUBSYSTEM NOISE | 14.9 | 6.9 | 3.4 | 3.0 | 2.9 | 2.8 | 0 | |
| TOTAL NOISE AT COMMUNICATIONS OUTPUT | 23.5 | 18.5 | 16.5 | 15.1 | 12.0 | 6.3 | 0 | |
| GRS RESPONSE | 1.000 | 1.000 | .941 | .837 | .714 | .635 | .573 | |
| NON GRS NOISE AT GRS OUTPUT | 23.5 | 18.5 | 15.5 | 12.6 | 8.6 | 4.0 | 0 | $\frac{mv}{(1/mm)^2}$ |
| NON GRS NOISE ON PRIMARY RECORD (DENSITY) | .00814 | .00641 | .00537 | .00437 | .00299 | .00139 | 0 | $\frac{1}{(1/mm)^2}$ |
| PRIMARY RECORD NOISE (DENSITY) | | | | .00230 | | | | |
| TOTAL NOISE ON PRIMARY RECORD (DENSITY) | .00846 | .00681 | .00585 | .00494 | .00377 | .00268 | .00230 | |
| TRANSMISSION NOISE DENSITY PRIMARY RECORD | .00346 | .00279 | .00240 | .00202 | .00154 | .00110 | .00094 | |
| DENSITOMETER RESPONSE | 1.000 | .947 | .913 | .818 | .690 | .554 | .402 | VOLTS |
| NOISE DENSITY DENSITOMETER OUTPUT | .00346 | .00272 | .00219 | .00165 | .00106 | .00061 | .00022 | $\frac{V}{(1/mm)^2}$ |
| FMS NOISE - DENSITOMETER OUTPUT | .0211 VOLTS | | | | | | | |

CALCULATED NOISE LEVELS AT EACH STEP IN
SYSTEM, 1/2 M. APERTURE

TABLE 1.3-2 ~~COPIED~~

VOL
SEC

NO 12-1002934
PAGE 28

1.3.3

Signal to Noise Ratio

From the data in Tables 1.3-1 and 1.3-2, the peak-to-peak signal to RMS noise ratio at the densitometer output may be calculated. This function is plotted in Figure 1.3-9 and applies to the case of test bars having a sinusoidal brightness distribution (sine wave bars) and a densitometer with an aperture diameter equivalent to 0.5 meter at the lunar surface.

When using a test target consisting of conventional bars (square wave bars), i.e., sharply defined bars on a contrasting background, the resulting peak-to-peak signal must be calculated by Fourier analysis. It can be shown that:

$$f(x) = \frac{4}{\pi} \sum_{n=1,3,5,\dots} \left(b_n \sin \frac{n\pi x}{L} \right)$$

where $b_n = \frac{f(n)}{n}$

and $f(n)$ is the system output at the n th harmonic frequency from Figure 1.3-9.

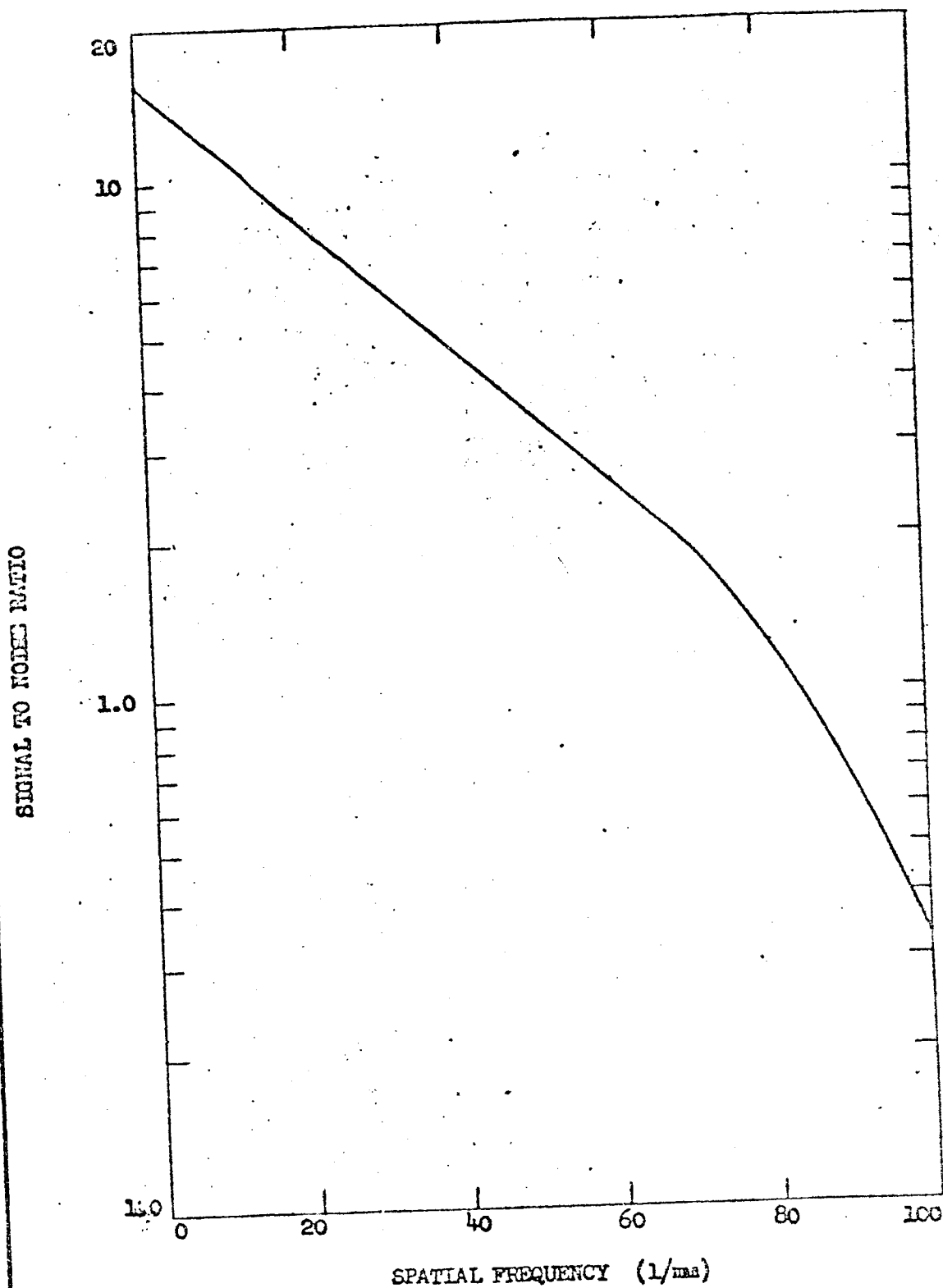
The values of b_n and $f(x)$ are tabulated for various spatial frequencies of the test bars in table 1.3-3, where:

$$f(x)^1 = \frac{4}{\pi} \sum_{n=1,3,5,\dots} b_n \sin \frac{n\pi x}{2}$$

represents the peak-to-peak value of the resulting output. This function is plotted in figure 1.3-10 and represents the output of the system for square wave bars when scanned with a densitometer having an aperture diameter equivalent to 0.5 meter at the lunar surface.

A further requirement of the statement of work is that 1 meter bars (38 1/mm) yield 6:1 signal to noise when scanned with a 1 meter equivalent aperture. Table 1.3-4 shows the ΔT at the GRS output (from Table 1.3-1), the response of a densitometer with an aperture diameter equivalent to 1 meter, and the resulting signal output. Table 1.3-5 similarly shows the noise at the densitometer output. Figures 1.3-11 and 1.3-12 show the signal-to-noise ratio vs. spatial frequency for a one meter scanning aperture for sine wave and square wave bars respectively. The data for figure 1.3-12 is tabulated in Table 1.3-6.

¹ Handbook of Mathematical Tables, Chemical Rubber Publishing Co., First Edition, 1962 pp 403-406



SIGNAL TO NOISE RATIO USING SINE WAVE BARS AND 1/2 METER EQUIVALENT APERTURE

FIG. 1.3 - 9

2-5142

U3 4288 2000 REV. 5/62

REV SYM _____

BOEING

NO. D2-100293 -1

SECT.

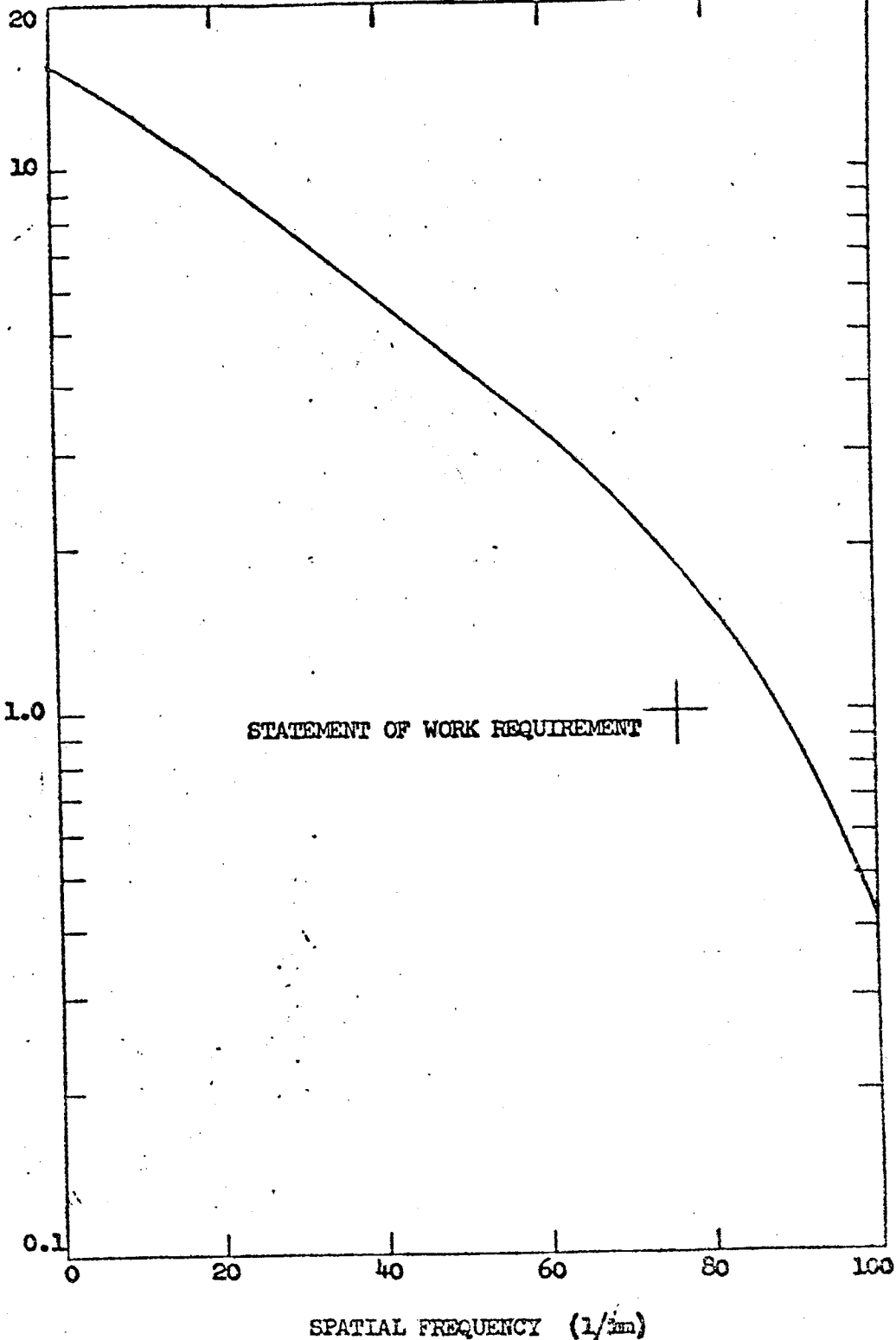
PAGE 30

| Spatial Frequency | b ₁ | b ₃ | b ₅ | b ₇ | b ₉ | b ₁₁ | b ₁₃ | b ₁₅ | $f(x)$ |
|----------------------|----------------|----------------|----------------|----------------|----------------|-----------------|-----------------|-----------------|--------|
| 2 | 14.7 | 4.3 | 2.3 | 1.5 | 1.0 | 0.7 | 0.5 | 0.4 | 14.7 |
| 4 | 13.9 | 3.6 | 1.8 | 1.0 | 0.6 | 0.4 | 0.3 | 0.2 | 14.5 |
| 6 | 13.0 | 3.0 | 1.3 | 0.6 | 0.3 | 0.2 | 0.1 | | 13.8 |
| 8 | 12.3 | 2.5 | 0.9 | 0.4 | 0.2 | 0.1 | | | 13.5 |
| 10 | 11.6 | 2.1 | 0.7 | 0.3 | 0.1 | | | | 12.7 |
| 12 | 11.0 | 1.7 | 0.5 | 0.1 | | | | | 12.3 |
| 14 | 10.2 | 1.5 | 0.4 | 0.1 | | | | | 11.4 |
| 16 | 9.7 | 1.2 | 0.2 | | | | | | 11.0 |
| 18 | 9.2 | 1.0 | 0.1 | | | | | | 10.3 |
| 20 | 8.5 | 0.9 | 0.1 | | | | | | 9.8 |
| 22 | 8.0 | 0.7 | | | | | | | 9.3 |
| 24 | 7.6 | 0.6 | | | | | | | 8.9 |
| 26 | 7.1 | 0.4 | | | | | | | 8.5 |
| 28 | 6.7 | 0.3 | | | | | | | 8.1 |
| 30 | 6.3 | 0.2 | | | | | | | 7.8 |
| 32 | 5.9 | .2 | | | | | | | 7.2 |
| 34 | 5.6 | .1 | | | | | | | 7.0 |

TABLE 1.3-3

FOURIER COMPONENTS OF SQUARE WAVE TEST BARS, 1/2 m. APERTURE

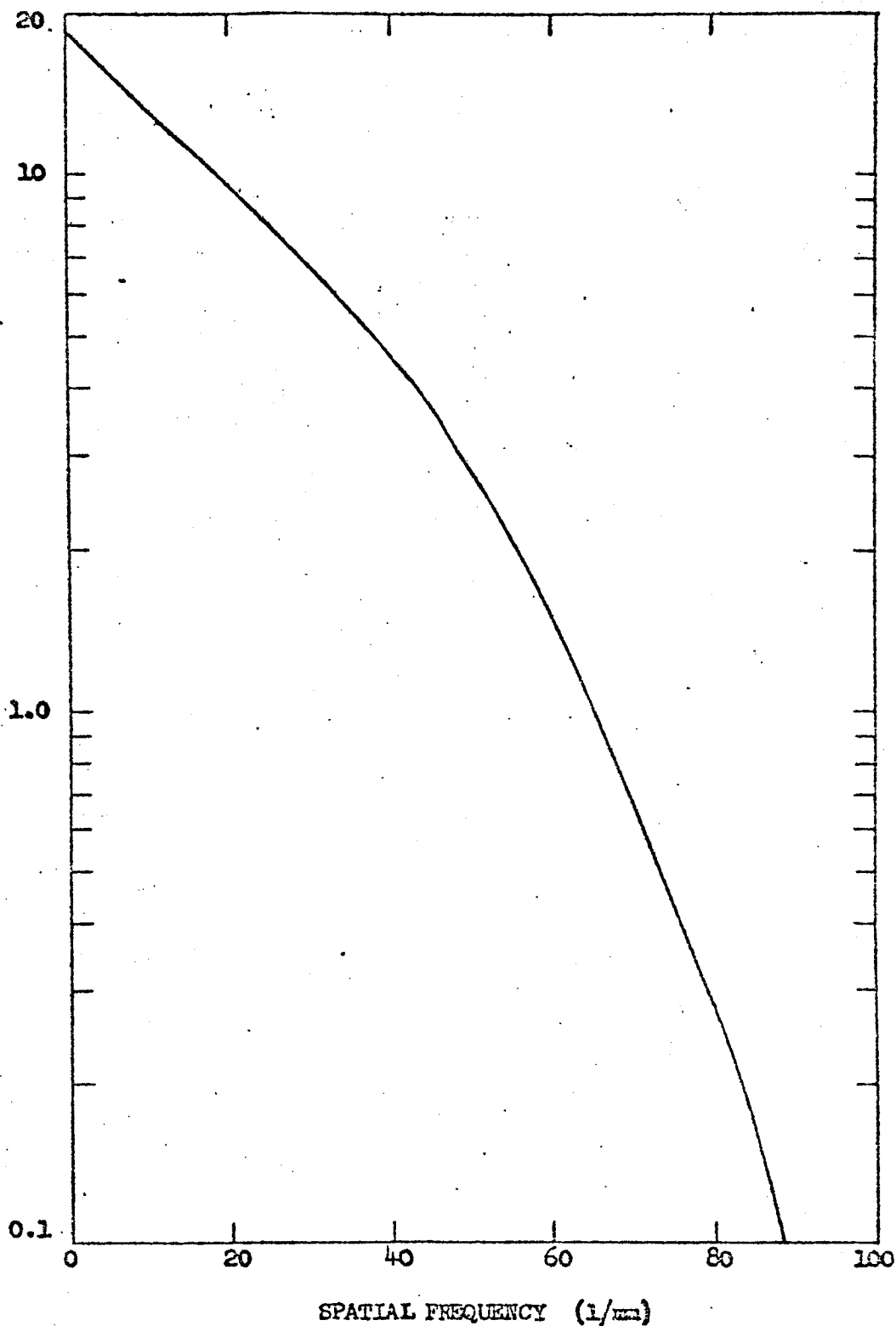
SIGNAL TO NOISE RATIO



SIGNAL TO NOISE RATIO USING SQUARE WAVE BARS AND 1/2 METER EQUIVALENT APERTURE

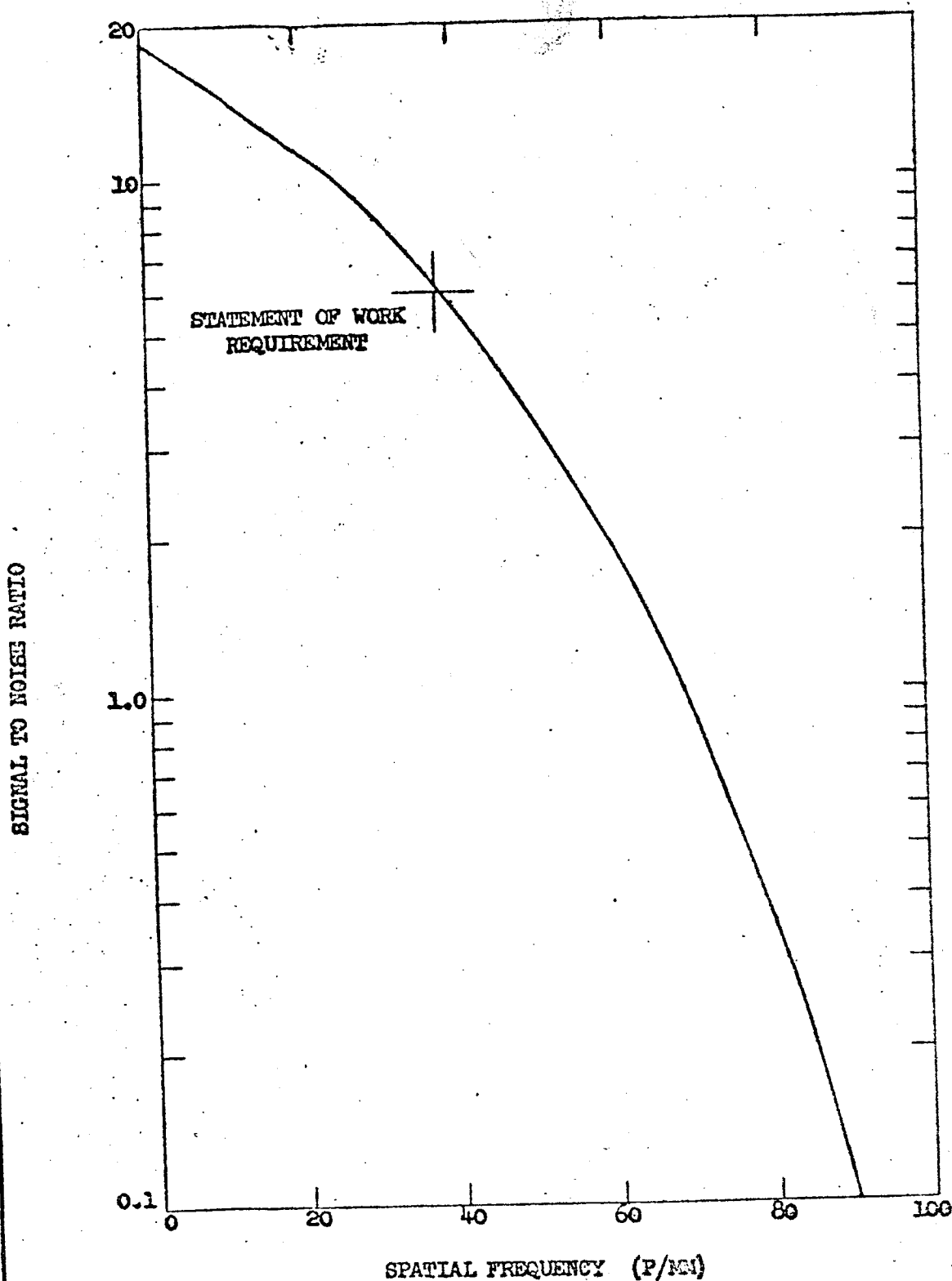
FIG. 1.3-10

SIGNAL TO NOISE RATIO



SIGNAL TO NOISE RATIO USING SINE WAVE BARS AND 1 METER EQUIVALENT APERTURE

FIG. 1.3-11



SIGNAL TO NOISE RATIO USING SQUARE WAVE BARS
AND 1. METER EQUIVALENT APERTURE
FIGURE 1.3-12

US 4289 2000 REV. 8/62

2-5112

REV SYM _____

| | |
|------------------|-----------------|
| DDEND | NO. D2-100293-1 |
| | SECT. PAGE 34 |

| Lines per mm | 0 | 20 | 40 | 60 | 80 | 100 | 120 | |
|-------------------------------------|------|------|------|------|-------|-------|-------|-------|
| ΔT GRS Output | .329 | .186 | .117 | .066 | .038 | .012 | 0 | |
| Densitometer Response 1.000 | .913 | .690 | .402 | .132 | -.056 | -.131 | volts | |
| ΔV Densitometer Out- Put | .329 | .170 | .081 | .027 | .005 | -.001 | 0 | volts |

TABLE 1.3-4
SYSTEM SIGNAL LEVEL FOR SINE WAVE BARS, 1 m. APERTURE

| | | | | | | | | |
|---|--------|--------|--------|--------|--------|---------|---------|--------------|
| Transmission Noise Density Primary Record | .0036 | .00279 | .00240 | .00202 | .00154 | .00110 | .00094 | |
| Densitometer Response | 1.000 | .913 | .690 | .402 | .132 | -.056 | -.131 | volts |
| Noise Density Densitometer Output | .00346 | .00255 | .00166 | .00081 | .00020 | -.00006 | -.00012 | $V/(1/mm)^2$ |

RMS Noise Densitometer Output 17.7 Millivolts

TABLE 1.3-5
SYSTEM NOISE LEVEL, 1 m. APERTURE

| Spatial Frequency | b ₁ | b ₃ | b ₅ | b ₇ | b ₉ | b ₁₁ | b ₁₃ | b ₁₅ | $f(x)$ |
|----------------------|----------------|----------------|----------------|----------------|----------------|-----------------|-----------------|-----------------|--------|
| 2 | 17.2 | 5.1 | 2.7 | 1.7 | 1.1 | 0.8 | 0.6 | 0.4 | 17.3 |
| 4 | 16.1 | 4.1 | 1.9 | 1.0 | 0.6 | 0.3 | 0.2 | 0.1 | 16.9 |
| 6 | 15.2 | 3.4 | 1.3 | 0.6 | 0.3 | 0.1 | | | 16.1 |
| 8 | 14.2 | 2.7 | 0.9 | 0.3 | 0.1 | | | | 15.5 |
| 10 | 13.3 | 2.2 | 0.6 | 0.1 | | | | 14.7 | 14.7 |
| 12 | 12.4 | 1.7 | 0.3 | | | | | | 14.3 |
| 14 | 11.5 | 1.4 | 0.1 | | | | | | 13.0 |
| 16 | 10.8 | 1.0 | 0.1 | | | | | | 12.6 |
| 18 | 10.0 | 0.7 | | | | | | | 11.8 |
| 20 | 9.6 | 0.5 | | | | | | | 11.6 |
| 22 | 8.8 | 0.3 | | | | | | | 10.8 |
| 24 | 8.1 | 0.2 | | | | | | | 10.0 |
| 26 | 7.5 | 0.1 | | | | | | | 9.4 |
| 28 | 7.0 | 0.1 | | | | | | | 8.8 |
| 30 | 6.5 | | | | | | | | 8.3 |

TABLE 1.3-6
FOURIER COMPONENTS OF SQUARE WAVE TEST BARS, 1 m. APERTURE

From figures 1.3-10 and 1.3-12 it can be seen that the Statement of Work requirements can be met on axis with the 24" lens for the nominal case.

A detailed analysis has not been performed for the 3" lens system since adequate modulation transfer function data for the lens-film combination is not available. The only difference between the 24" and 3" lens systems is this transfer function. Data is available which indicates that the limiting lens-film resolution of the 3" lens is about 13% lower than the 24" lens (in lines per millimeter). Since the lens-film transfer function is only one of many contributors, it is estimated that the net change in system resolution will be a loss of about 5%, giving a signal to noise ratio margin of about 3 db at 8 meters resolution. For the case of the 8 meter bars scanned with an aperture of 8 meters, no such extrapolation can be made since there is "no" data available in the region of 38 lines per millimeter. In general, all that can be said is that there will probably be less difference in performance at 38 lines per millimeter than at 76 lines per millimeter, with the possibility that the 3 inch lens may even be better than the 24 inch lens.

2.0 Off Nominal System Performance

2.1 Effects of Off Nominal Values of Variables

This section presents data to permit analysis of the effects on system performance of the parameters under various off-nominal conditions that might be encountered.

2.1.1 Variations in Exposure

Off nominal film exposure will occur which is caused by target characteristics, the space environment, and errors originating in the photographic system. The amount of variation, its occurrence, and its effect upon the photographic capabilities with respect to resolution and picture quality will be characterized by the source of the variation. Each of the causes mentioned will produce a change in picture quality or exposure which will ordinarily be characteristic of the general type mentioned. Each of these is discussed in turn.

2.1.1.1 Variation Due to Target Characteristics

Of concern here are the brightness differences of the gross lunar features or larger areas which affect the overall field of view or a significant portion of it. The apparent brightness of the lunar surface, which determines the exposure requirements is dependent upon the surface albedo and the photometric function. The first is a characteristic of the surface material, its structure, or a combination of both. The photometric function is an expression defining the modification of reflectance by the variable geometry of the surface, the illumination, and the line of sight. These factors are discussed in detail in Section 3.0.

Two broad types of lunar surface are recognized which have appreciably different albedos. The upland areas are generally lighter, with an albedo ranging between about 0.10 and 0.15. The darker maria, on the other hand, have albedos ranging between 0.05 and 0.08. Albedos of individual features or small areas may exceed these limits. The average albedo of the moon is about 0.07. Because the Lunar Orbiter will pass over both upland and mare areas, exposure must be based upon the area type to be photographed, since the brightness may differ by a factor of 3.

Unless a photograph is intended to record detail of some atypical area, exposure must be based upon the scene luminance integrated over the field of view or over that part of the field having greatest significance. Since the photographic system is designed for optimum performance on-axis, the central area of the field of view will be most significant and exposure should be based on its luminance. It is shown in Section 3 that, because of the photometric characteristic of the surface, the off-axis line of sight defining the field of view will produce an apparent cross-frame luminance difference. On a level surface of uniform properties, an off-axis angle of 10° , approximating the format edge of the high resolution camera, may exhibit a cross-frame brightness ratio of between 1.3 and 1.4 in the illumination plane, depending upon the sun angle.

Referenced to the nadir brightness, this amount to ± 0.2 to ± 0.25 f. stops. If the exposure is correct at the nadir point, in the area of maximum resolution, the film will be slightly overexposed in the direction away from the sun and underexposed on the side toward the sun.

2.1.1.2 Variations due to the Space Environment

The photographic film will be subject to high energy ionizing radiation during the mission. Prior to processing, this radiation will affect the emulsion in much the same way as exposure to visible light, producing a general fogging effect. This effect and its occurrence is discussed in detail in Section 6.1. Fogging of the film will increase image density and will reduce contrast or gamma, which degrades resolution and picture quality.

A radiation dose will be received during passage of the vehicle through the Van Allen belts which may be significant with respect to film damage. As shown in Table 6.1-8 and Figure 6.1-4, a fog density of 0.3 or more may be produced.

Solar particle events, usually associated with solar flare activity, can be a source of radiation damage to the film. Flare activity which can affect the mission is intermittent and of variable intensity. It has been estimated that total mission failure due to radiation effects from solar particle events has a probability of 10% or less.

There has been some concern that impacts of meteoric particles and secondary ejecta from the lunar surface may damage the lens. This is discussed in detail in Section 6.2. Lack of data prevents reasonably quantitative assessment of this hazard and its effects on the lens. There appears to be no analytical or empirical data on the degradation of optical characteristics of a lens which has been pitted. It would seem, intuitively, that pits on the lens surface would cause scattering of light and consequent lowering of resolution by a fogging type effect as well as possible image distortion. A decrease in effective aperture may also occur.

2.1.1.3 Variations Due to System Errors

Exposure variation may also originate within the photographic system due to optical effects and operational errors. Transmission characteristics of the camera lens will produce an exposure variation within the frame. Transmission decreases as off-axis angle is increased to the limiting field angle. This vignetting results in underexposure toward the edges of the picture area. This effect will, to some extent, resemble the off-axis effect of the photometric function, but without the orientation to the plane of illumination. Transmission variation will produce an exposure difference between the center and the edge equivalent to about 0.5 f. stop in the 24 inch lens and about 1.0 f. stop in the 3 inch lens.

Additional error in exposure will be associated with the operational accuracy of the shutter mechanism; and in the accuracy of shutter setting. These errors would be the same for either camera and is estimated to be equivalent to about 1 f. stop. An error must be assigned to prediction of nominal camera settings because of inadequate data for the prediction basis. A nominal error of 0.5 stop has been assumed.

The nominal exposure errors are summarized below:

| | 24" lens | 3" lens |
|--------------------------------------|----------|-----------|
| Photometric function uncertainties | 0.5 stop | 1.5 stop |
| Albedo, slopes, etc. | 1.0 stop | 1.0 stop |
| Lens transmission | 0.5 stop | 1.0 stop |
| Shutter setting & operating accuracy | 1.0 stop | 1.0 stop |
| Prediction of setting | 0.5 stop | 0.5 stop |
| RSS Error = | 1.5 stop | 2.25 stop |

2.1.1.4 Effects of Exposure Variation on System Performance

The primary criterion of system performance is image resolution, which is closely related to film exposure. By making some assumptions, the relationships of exposure, film gamma, granularity and signal-to-noise to resolution, an approximate correlation in terms of lines per millimeter may be drawn. This is shown in Figure 2.1.1-1.

Curve A represents a portion of the familiar H and D plot for S.O.243 relating image density to log exposure. Curve B is a postulated relation between signal-to-noise, as affected by density and granularity and resolution. The resolution scale is an approximation to provide an indication of estimated effect and should not be taken as absolute values. Approximate film resolution is indicated by the intersection of an exposure value with curve B. As shown, the nominal exposure will provide a resolution of about 80 lines per mm. As exposure is decreased from the nominal, the change in film gamma results in a decrease in resolution. With increase in exposure, granularity increases which degrades resolution. A variation in exposure amounting to 0.5 stop will lower resolution to near 70 lines per mm.

READOUT DENSITY VS. EXPOSURE
8.0. 243 FILM BIMAT PROCESSING

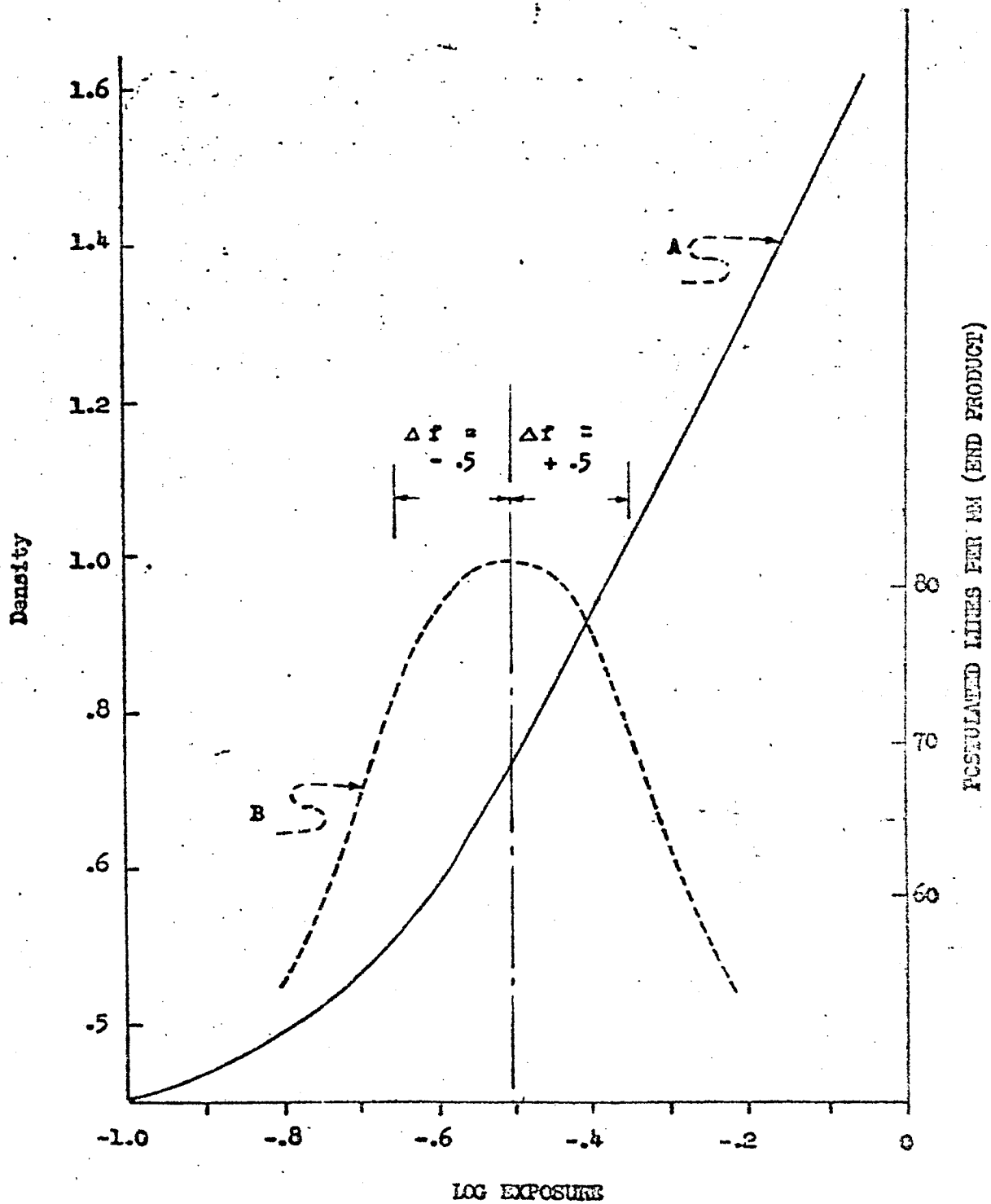


FIGURE 2.1.1-1

US 4288 2000 REV. 2/64

REV SYM _____

BOEING NO. D2-100293-1
PAGE 41

2.1.2

Off-Nominal Variations in Transfer Functions

The basic analysis in Section 1 of S/W or performance of the LOS system is based upon the nominal conditions which include on-axis imagery for the lens, correct focus for the lens, optimum exposure setting, and the holding of smear budget tolerances. Some of the conditions which give off-nominal performance are discussed here from the standpoint of degrading the signal. Exposure variations and off-nominal smear contributions are discussed in Sections 2.1.1 and 2.1.5 respectively.

The first factor to be considered is the performance of the lens in terms of image quality at points in the field of view other than the on-axis point. Measured data for off-axis resolution of the 24 inch and 3 inch lenses as supplied by Eastman Kodak is shown in Figures 2.1.2-1 and 2.1.2-2 respectively. The data is for 2/1 target contrast on S.O. 243 film with D-19 processing. The dashed line for the 24 inch lens represents the measured off-axis performance of the original 24 inch, f/5.6 Pacific Optical Paxoramic Delta lens. The solid line represents the Eastman specification for this lens after vignetting and otherwise modifying for decreasing the weight.

The dashed line on the 80 mm lens represents measured off-axis resolution with a 2/1 target contrast and S.O. 243 film with D-19 processing. The solid line represents the Eastman Kodak specification on this lens.

The 24 inch lens will be considered in more detail. Data is not available (ray trace spot diagrams, etc.) to permit accurate derivation of modulation transfer functions* for the lens off-axis. However, for the purpose of working in quantitative terms, off-axis MTF's have been postulated for this lens and are plotted in Figure 2.1.2-3. One point on each of these curves is available from the data of Figure 2.1.2-1. The postulated curve shape is considered valid based on data from other high acuity refractive lenses with good color corrections (1). Data measured by Eastman on the original lens with and without filters gives justification for not considering wavelength as a major parameter. Eastman indicated less than a 4% difference in performance in white light vs. spectral bands. It should again be emphasized that only the off-axis MTF curves in Figure 2.1.2-3 are postulated and not based on actual data for this lens.

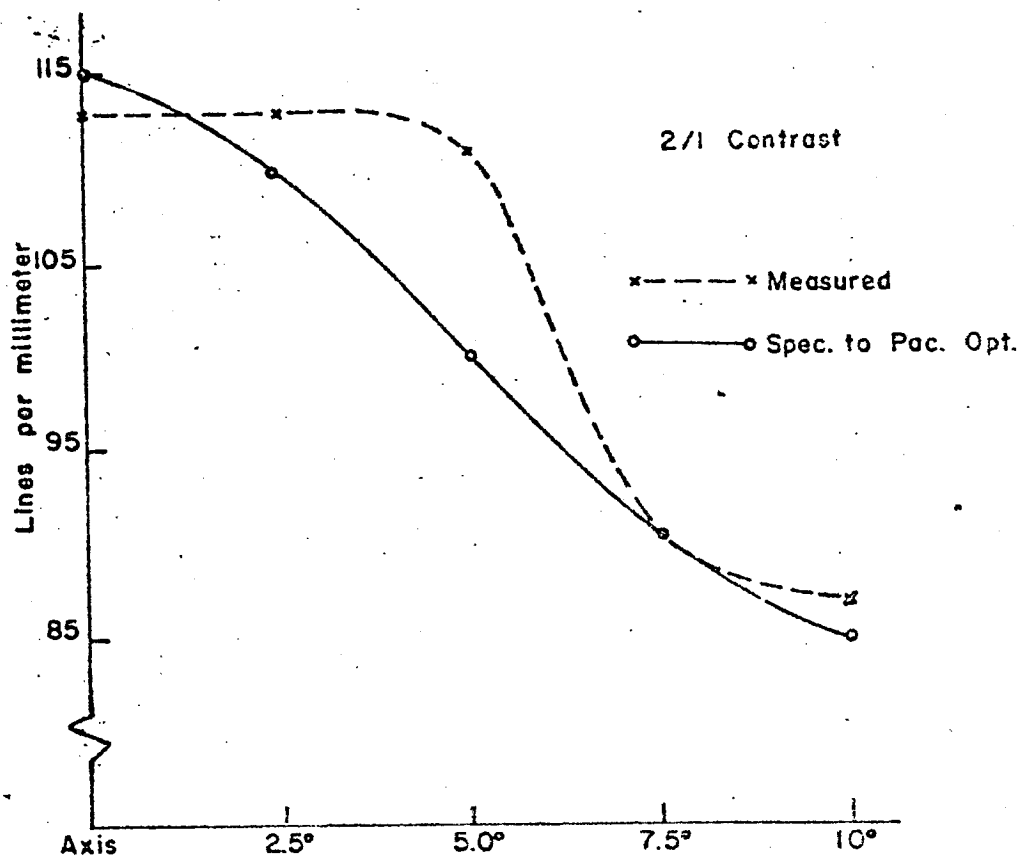
Some additional preliminary data on this subject was received from Eastman Kodak in October, 1964, which is inserted here. Computer ray trace data for the lens formula was utilized to generate MTF's for 7° and 10.5° off-axis. The limiting condition was for tangential resolution in each case and these resultant MTF's are shown in Figure 2.1.2-3a. These curves will be degraded by some factor in terms of the capability to fabricate the actual lens per the formula. The dashed lines represent a typical 30% degradation due to fabrication. Actual performance data for off-axis, however, will have to await measurements on a fabricated lens.

2.1.2

*The reader who desires to review the basis for the use of transfer functions for signal analysis is referred to Section 4.1.

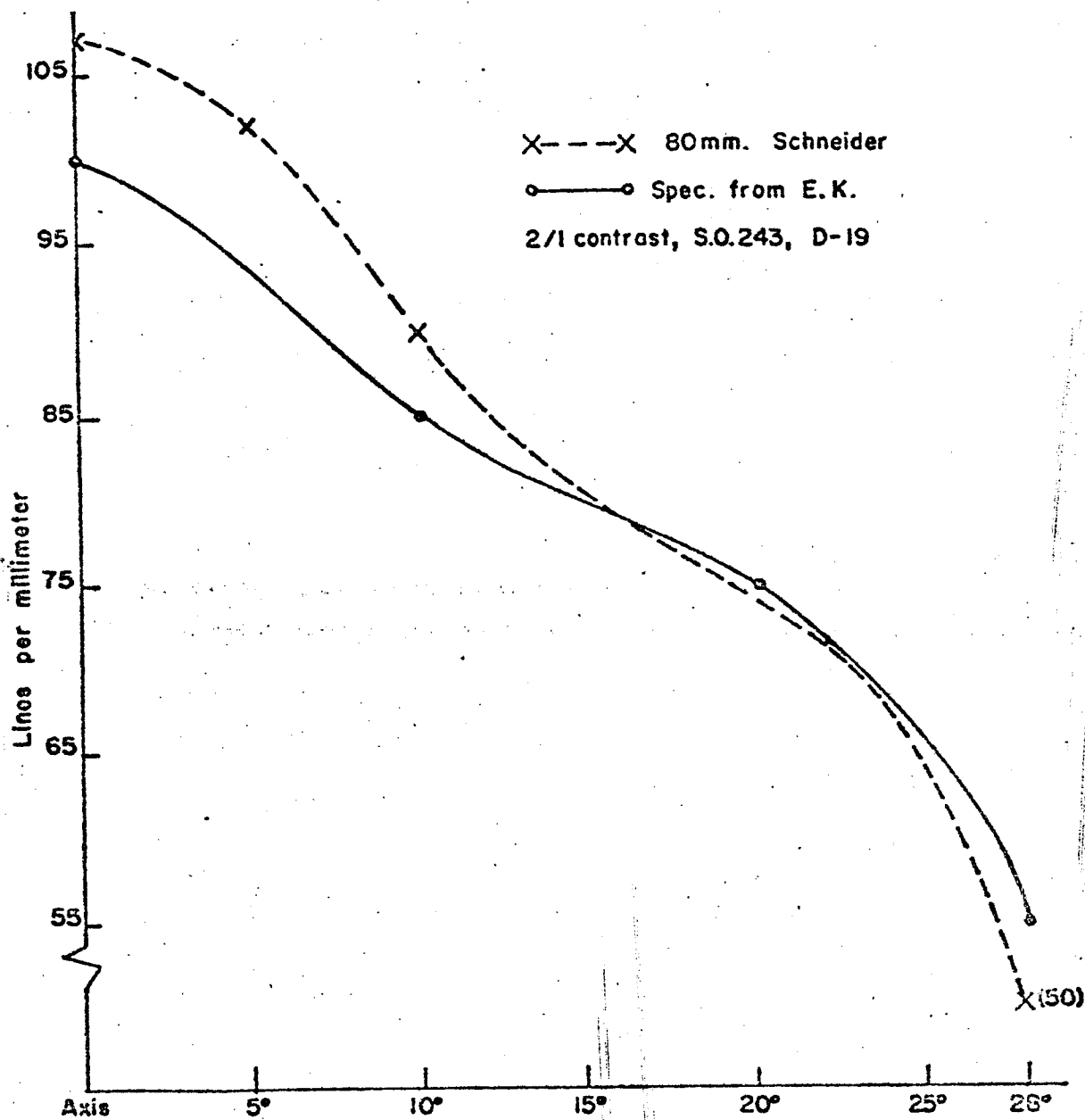
- (1) See, for instance: "A Research Study on Diffraction Limited Optics", Perkin-Elmer Corp., Report No. 5564, 1960

OFF - AXIS PERFORMANCE



Eastman Kodak specification to Pacific Optical : 24" F.L., S.O.243, D-19, 2/1 Contrast.

Figure 2.1.2-1



3" Lens Off-Axis Performance

Figure 2.1.2-2

U3 4288 2000 REV. 3/64

REV SYM _____

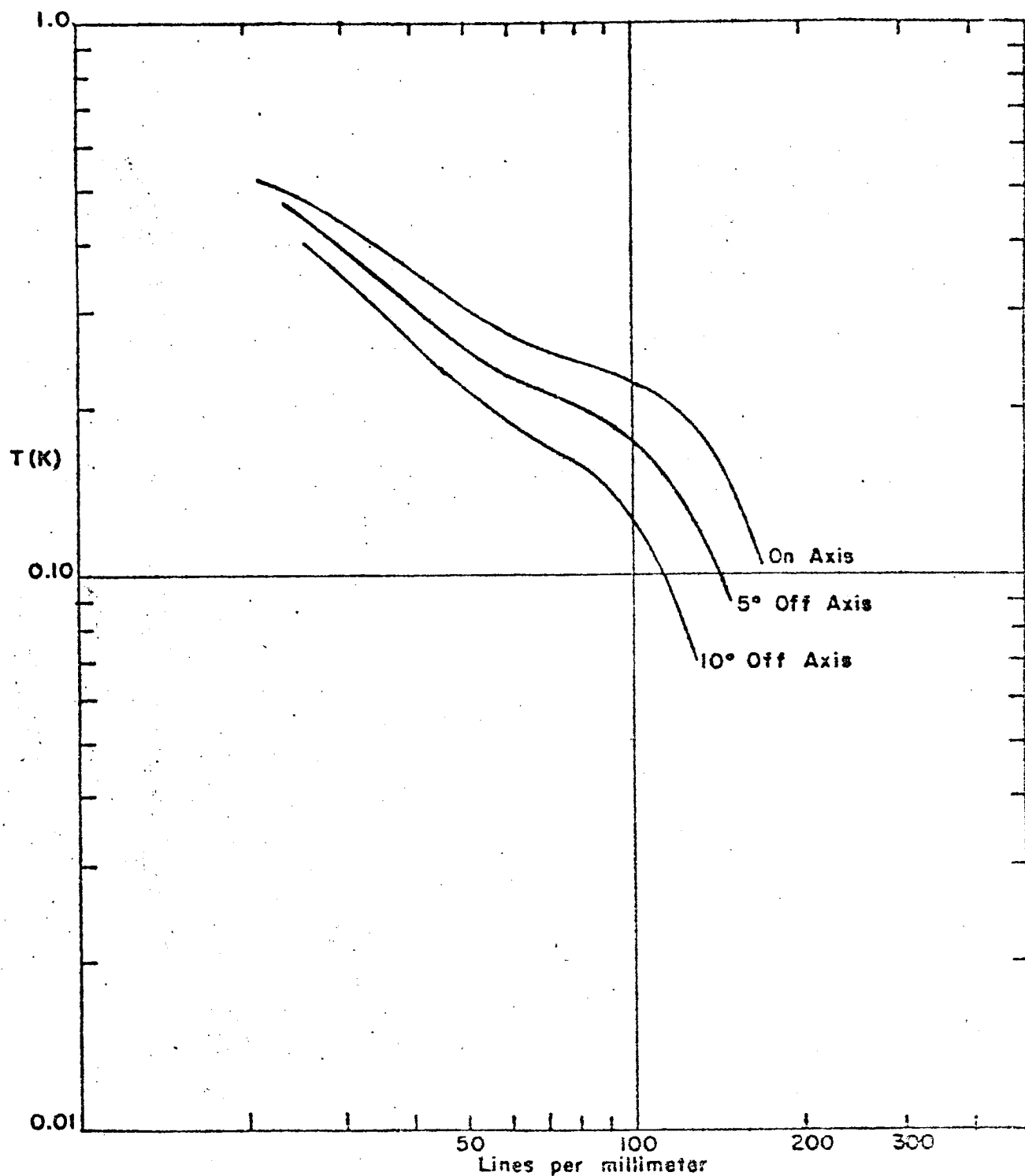
BOEING

NO.

D2-100293-1

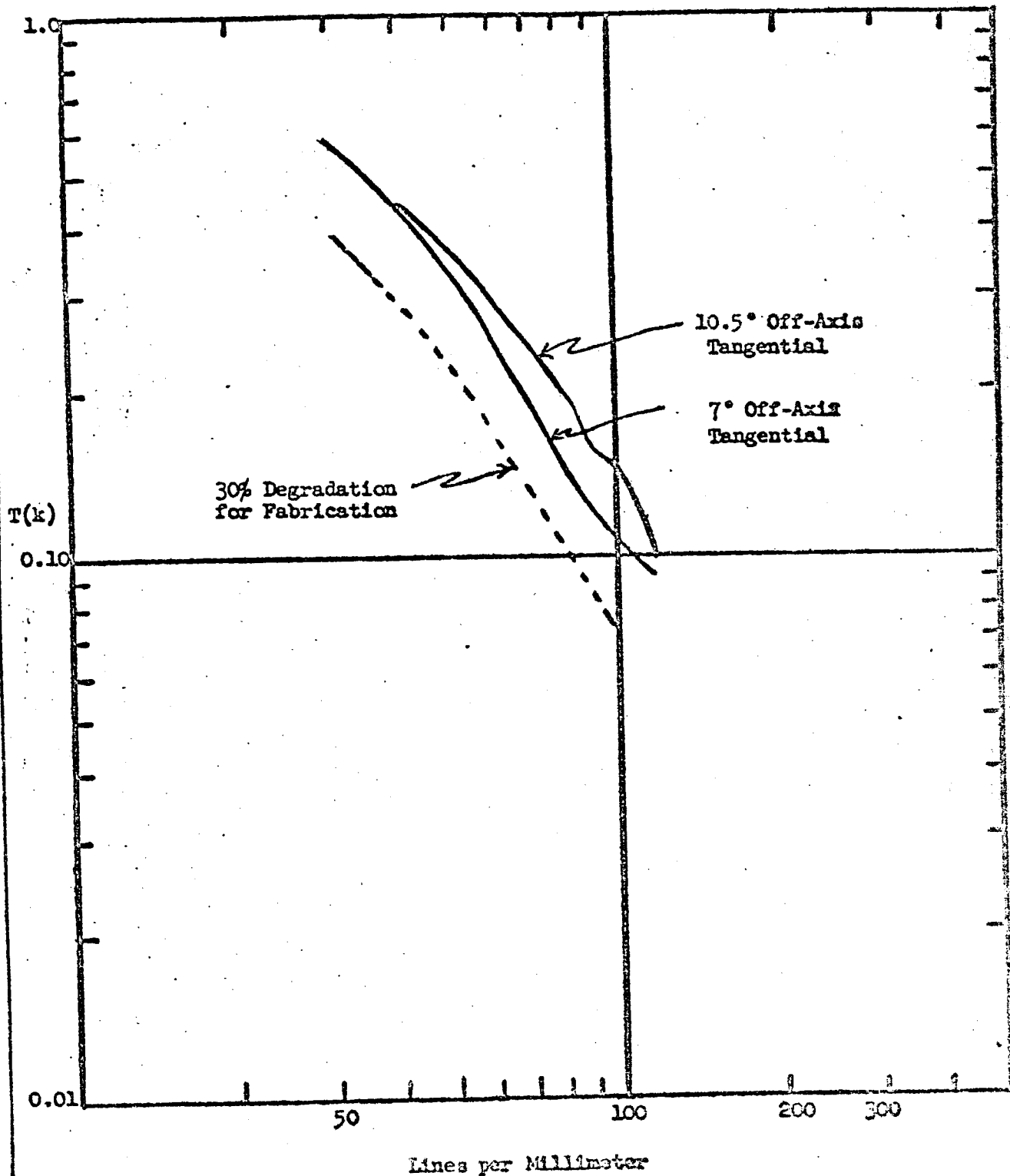
PAGE

45



Postulated Off-Axis Transfer Functions for 24 inch Lens.

Figure 2.1.2-3



OFF-AXIS TRANSFER FUNCTIONS COMPUTED FROM 24" LENS FORMULA

FIGURE 2.1.2-3a

The second potential off-nominal condition to consider is that of performance of the lens when out of focus. The focus tolerance for each of the lenses is ± 0.001 inches. Again, the 24 inch lens is discussed in some detail. Kodak has provided measured data on the original 24 inch lens performance when it is 0.002 inches out of best focus position. This data is plotted in Figure 2.1.2-4. The capability to hold focus tolerance is, of course, tied very closely to the thermal model and the ability to control the lens temperature environment to within the $70 \pm 5^\circ \text{F}$ specified. No provision is made for focus adjustment in flight for this system.

To permit quantitative signal analysis for this off-nominal condition, a transfer function is postulated for the 24 inch lens at a focus position 0.002 inches off optimum. This function is plotted in Figure 2.1.2-5. This plot is for the on-axis condition. A single point of the curve is available from the data of Figure 2.1.2-4. The shape of the curve is considered valid from other analysis of MTF degradation as a function of focus shift⁽²⁾. Again, it should be pointed out that the lens is considered to be color corrected to a degree where this curve is considered adequate for the total white light band.

In terms of the transfer functions used for the nominal S/W calculation of Section 1, the majority of functions used are considered to be fairly firm because they represent measured data. The lens data, as explained earlier, represents measurements on the original lens design. This is the optimum lens for this system. Other lenses which would more closely approach the diffraction limit and provide the field angle and color correction of this one would add a considerable weight penalty. The film/process MTF also represents measured data. The scanner unit MTF is primarily a product of the functions for the scan lens and the tube. The scan lens represents measured data. However, the PM tube function is calculated from the spot size image spread data. The accuracy of this calculated function must await actual measurement data when the tube becomes available. The communications system analysis, Section 4.4, includes the error tolerances assumed realistic for that system. The transfer function for the ground reconstruction electronics and 35 mm recording camera is not expected to deviate from the nominal curves used. Since the system is being utilized at approximately 13 lines/mm, off-axis effects should be minimal. An additional transfer function for the lens-film combination in the reassembly printer has not been included. The response at the frequency utilized should be near 95% so this omission is considered valid. Actual data on this unit is not available at this time.

(2) See, for instance: R. E. Hopkins, "Practical Comments on Frequency Response Calculations", Image Evaluation Techniques, University of Rochester, 1963

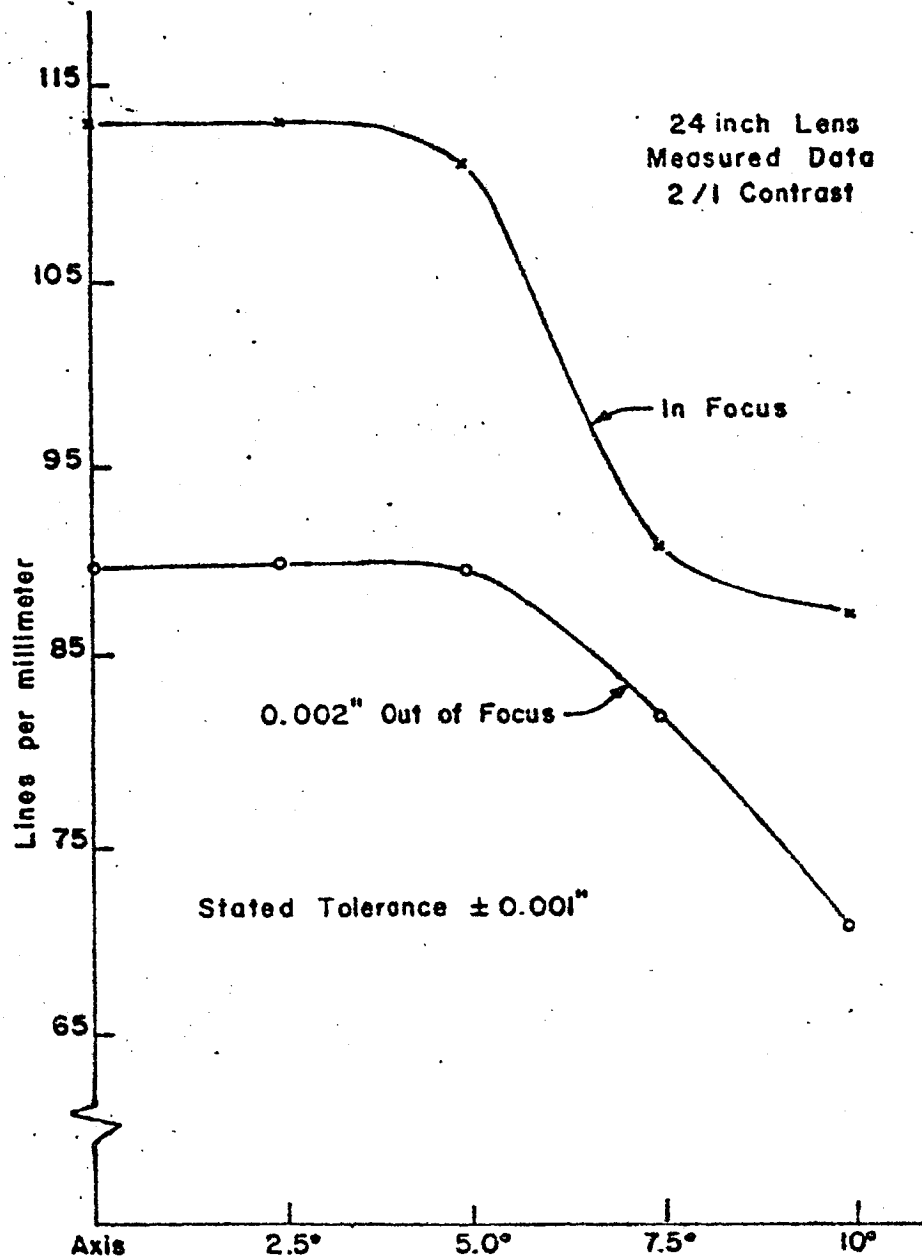
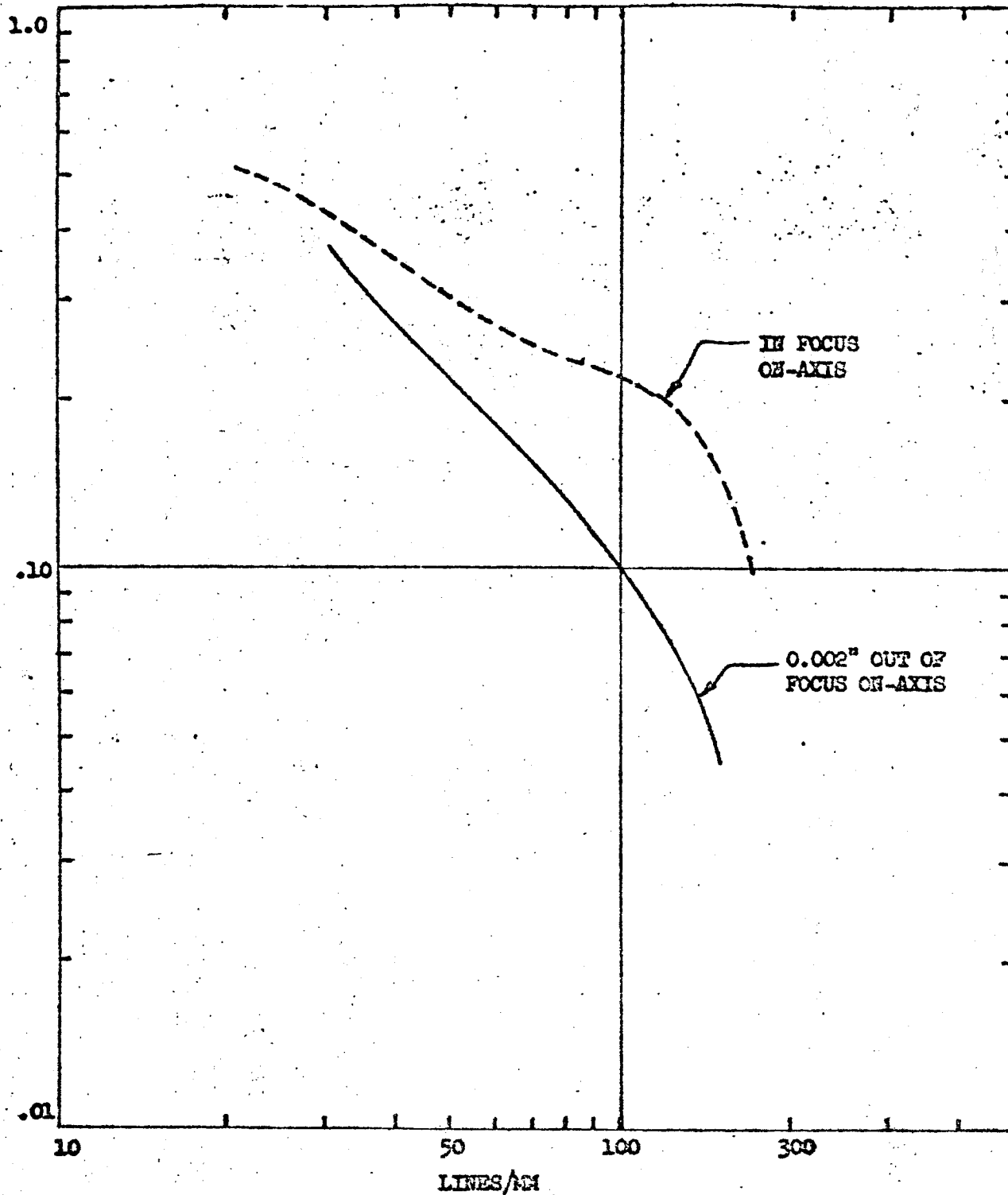


Figure 2.1.2-4



POSTULATED MTF FOR 24" LENS WHEN 0.002 INCHES
OUT OF FOCUS

FIGURE 2.1.2-5

2.1.3

Variations in Contrast Ratio

The system analysis given in Section 1.0 was limited to on-axis line of sight and a correct exposure for the central areas of the field of view. Apparent brightness of the surface of the moon will vary within the field of view as a result of the variable geometry of line of sight, illumination, and surface albedo as discussed in detail in Section 3.0.

If a level surface of uniform albedo is assumed, the cross frame exposure will vary as a result of off-axis line of sight and the effect of the photometric function, and may be expressed as a brightness ratio. Furthermore, this ratio will also be a function of the solar phase angle, referenced to the nadir line. A flat, level surface cannot be assumed. Few lunar areas, even at the resolution limits of Earth-based observation, are completely devoid of terrain features, and as resolution is increased, topographic irregularities must become more common. Such irregularities, having slopes, will introduce additional variations in apparent brightness and consequent scene contrasts as a result of the photometric function, even where hard shadows do not occur. The contrasts arising from surface slopes, off-axis line of sight, and the limiting sun angles of 50° and 75° are given in Table 3.3-1.

In the above tabulation, a uniform albedo is assumed. Variations in reflectance due, presumably, to differences in surface composition or structure occur on the surface. Some typical values of albedo reported in the literature are listed in Table 3.1-1. Upland areas have an albedo generally about .10 to .12 while the maria range between .05 to .08. Bright ray structures, associated with primary impact craters, occur on both maria and uplands, but, because of their high albedo of .12 or higher, are more prominent on the maria because of the contrast.

Albedo variations can increase the contrasts given in Table 3.1-1, since reflectance is the product of albedo and the value of the photometric function as listed. Thus, these contrasts can be greater by a factor of two or more.

Contrast variation will occur as a result of the combination of a number of inter-related factors, some of which occur with random frequency and magnitude. An approximation of these variations, as they may occur during an orbital pass of the photographic mission is discussed in Section 3.3.2. The mean contrast ratio between adjacent areas of differing brightness, within the mission illumination limits, as determined from the A.C.I.C. Charts, was about 1.24, with 6% exceeding a ratio of 2:1. These contrasts were computed for on-axis line of sight only.

The contrasts derived from the above profile are approximations based upon gross topography as portrayed on the Lunar Atlas Charts. Reference to Figure 3.3-9 shows that the mean distance over which brightness was assumed constant was about 2 kilometers.

Since brightness is a function of slopes, and, as the indicated slope decreases as the integrated interval is increased, higher slopes and greater contrasts will occur across small terrain features. A cone model has been specified for representation of the small features to be resolved. This is shown in Figure 3.3-2.

Maximum-minimum contrasts across the cone model vary with the illumination angle, ranging from zero with the sun angle directly along the line of sight at nadir, to infinite when hard shadows occur as the illumination and slope angles coincide. This is shown in Figure 3.3-4. It is further seen that at the minimum specified sun angle of 50° , the on-axis contrast across the cone is 3:1.

Contrast across the cone model is modified by changing the line of sight as shown in Figure 3.3-5. Variation both above and below contrast at nadir occurs. A maximum of about 4:1 is reached with line of sight 20° off axis directed away from the sun and a minimum of 2.3:1 at 20° off axis toward the sun. This difference in contrast ratio will affect resolution by about 7 lines per mm. The higher contrasts increasing the nominal resolution of 76 lines per mm to about 83 while the lower contrast reduces it to about 69.

2.1.4

Variations in Filter Characteristics

Variations in the filter characteristics take two general forms:

- Variations in frequency response
- Variations in Phase with frequency

The filter characteristics defined in D2-100112 have been chosen such that the effect of the filter is negligible.

In general, variations in frequency response outside the tolerance specified in D2-100112 will cause slight losses or gains in resolution. For variations of 1 db or less, the change in resolution should not be noticeable.

Variations in phase, i.e., group delay, with frequency of up to ± 1.0 microsecond cause only slight distortion of edges in the image. These distortions are not of a type that would reduce the detectability of the edge, however. Excessive group delay would result in reduction of the slope of the edge along with secondary edges, resulting in an uncertainty in the location of the edge. This would not impair the systems ability to detect objects with sizes on the order of the limiting resolution. In photographic terms, the system would suffer a loss of acuity.

2.1.4

(Cont'd)

Figures 2.1.4-1 and 2.1.4-2 show several hypothetical phase characteristics and their respective edge responses. These are extreme cases with values of $\frac{d\phi}{dF}$ which are unlikely to occur in a practical system. The three cases were arbitrarily chosen for the investigation of worse cases more severe than expected. Other cases with equally large phase shifts, but lower values of $\frac{d\phi}{dF}$ would not exhibit such severe overshoot.

The curve labeled "D" is the most severe of many cases run with differential group delays up to ± 3.0 microseconds. Weighing the results of this filter effects study, it has been concluded that for expected values of $\frac{d\phi}{dF}$, the group delays of up to 3 microseconds will not seriously degrade system performance, and values of 1 microsecond will have a negligible effect.

VARIATION OF PHASE WITH FREQUENCY

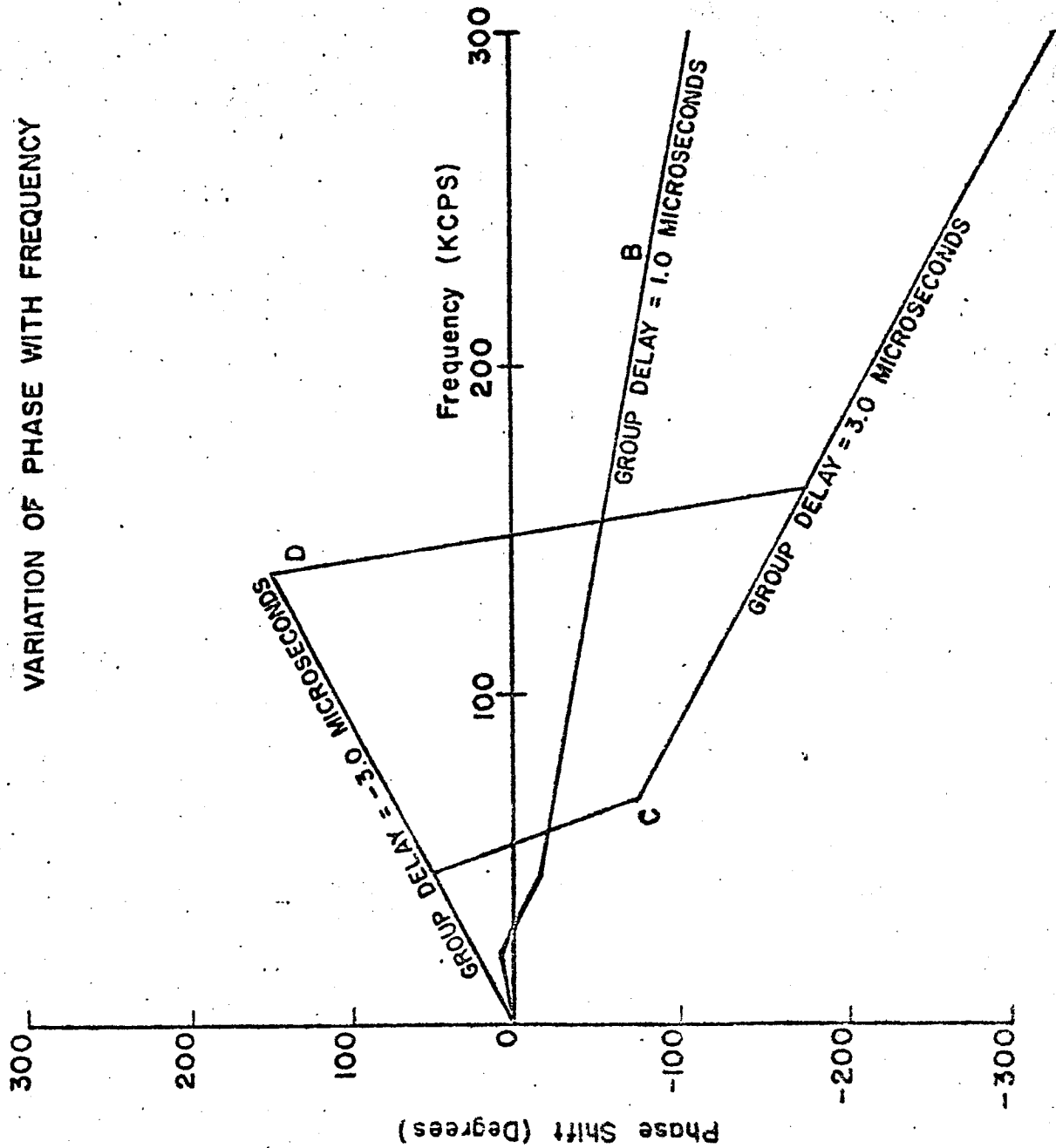
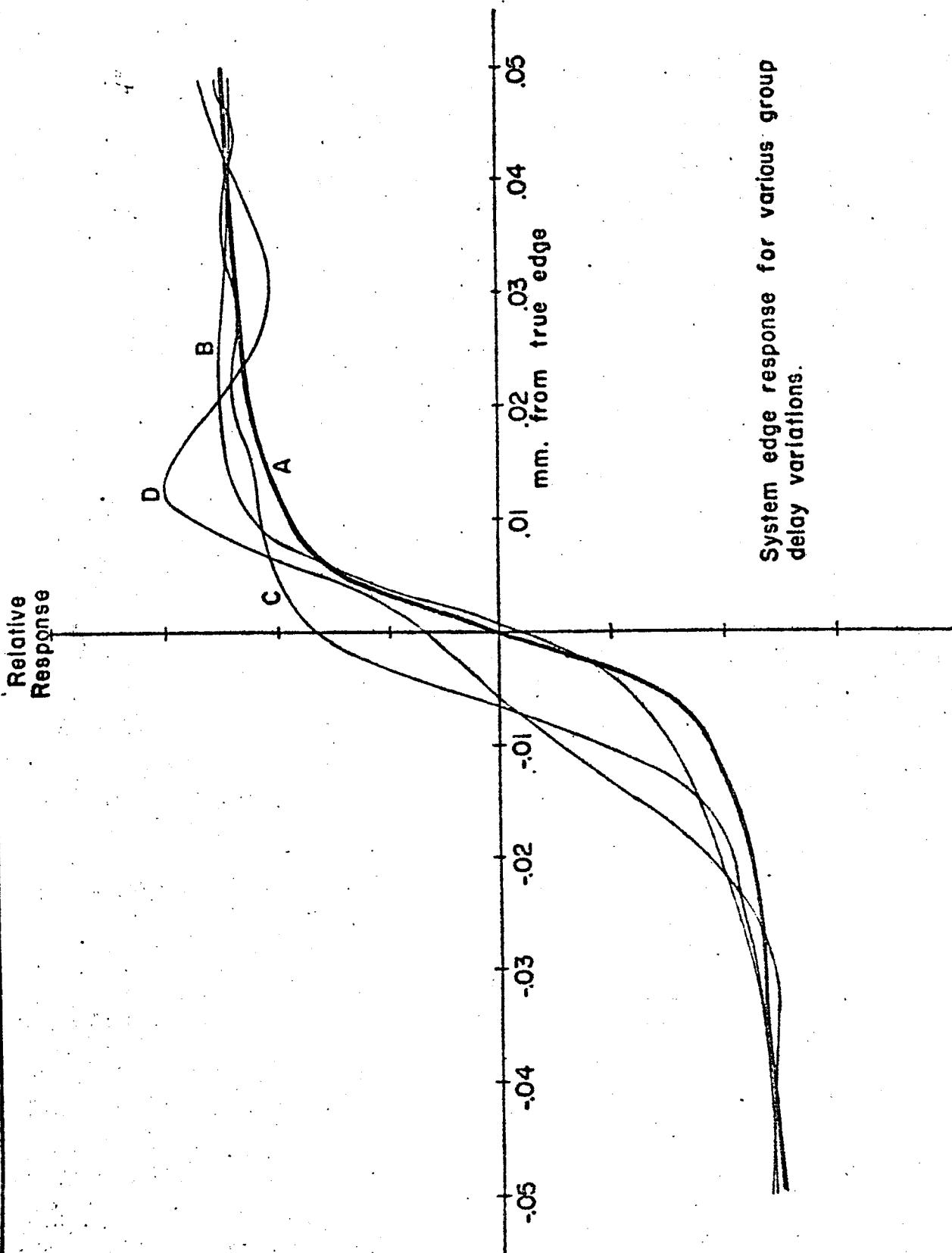


Figure 2.1.4-1



System edge response for various group delay variations.

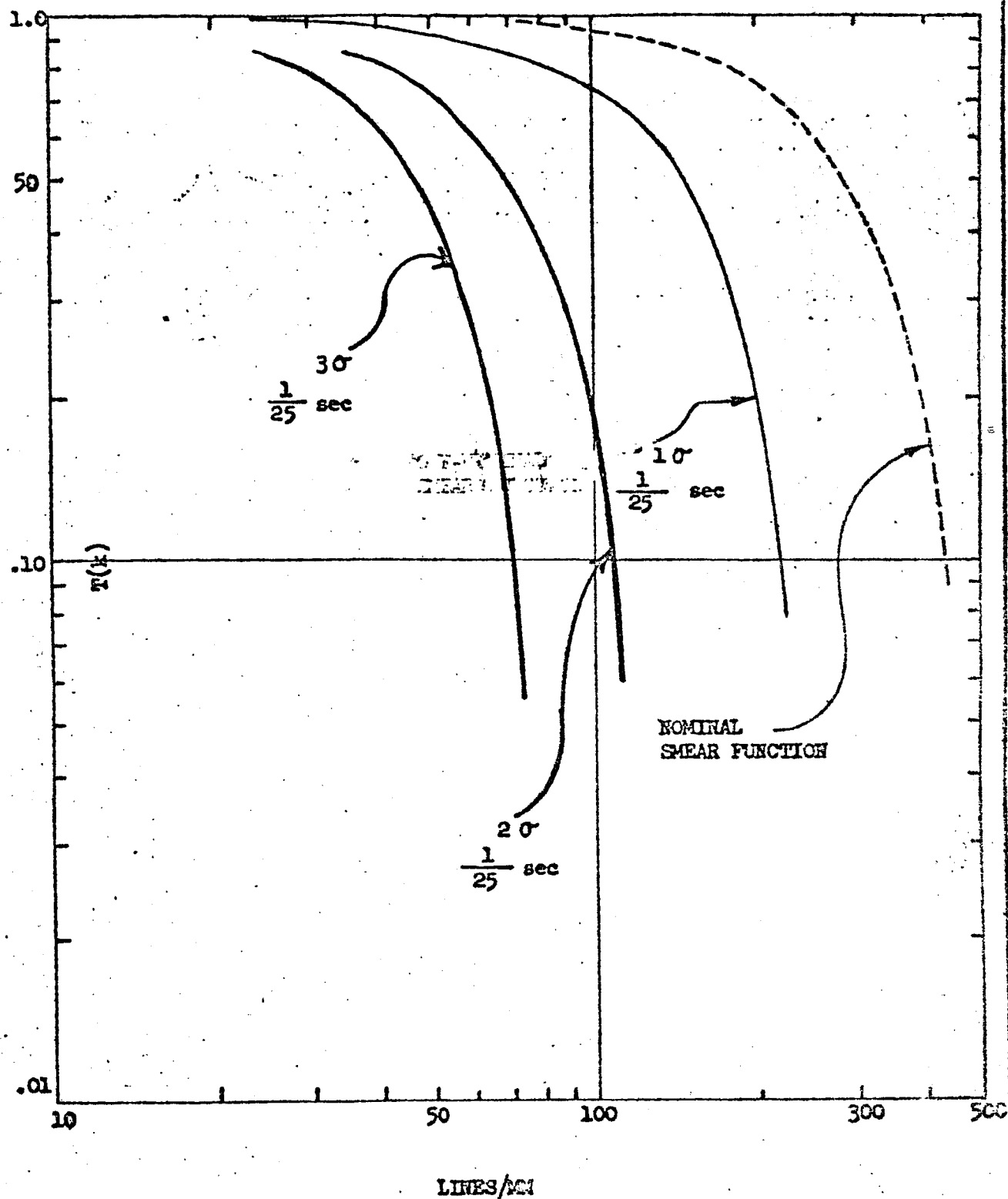
Figure 2.1.4-2

2.1.5

Off-Nominal Smear Conditions

The contributions to the smear budget assumed for the nominal case due to V/H, IXC, attitude control errors, etc., is discussed in Section 5.0. It is concluded that the expected smear is insignificant in terms of the overall system performance. Specifically, the modulation response at 76 l/mm is calculated to be 0.96.

Three curves are presented in figure 2.1.5-1 for analysis of off-nominal smear conditions. These include one with a nominal 1σ smear error but the maximum exposure of 1/25 second; a curve which represents the 2σ error, 1/25 second exposure of which 96% of the photos should be superior to; and a worst case condition with 3σ errors and the 1/25 second exposure.



MODULATION TRANSFER FUNCTION FOR
OFF-NOMINAL SMEAR
FIGURE 2.1.5-1

3.0

Contrast Ratio and Exposure

The detection of a surface feature by photographic methods requires, implicitly, the existence of a contrast between that feature and its surrounding. Those factors which control or determine brightness, and brightness differences or contrasts are of major concern to photography of the lunar surface. The brightness of the lunar surface varies as a result of changing geometrical relationships between the angle of illumination, lines of sight, and slope of the surface according to unique reflection characteristics, due to its physical structure or texture, and to variations in albedo or brightness due to composition or a combination of composition and physical characteristic of the material.

3.1

Factors Affecting Surface Brightness

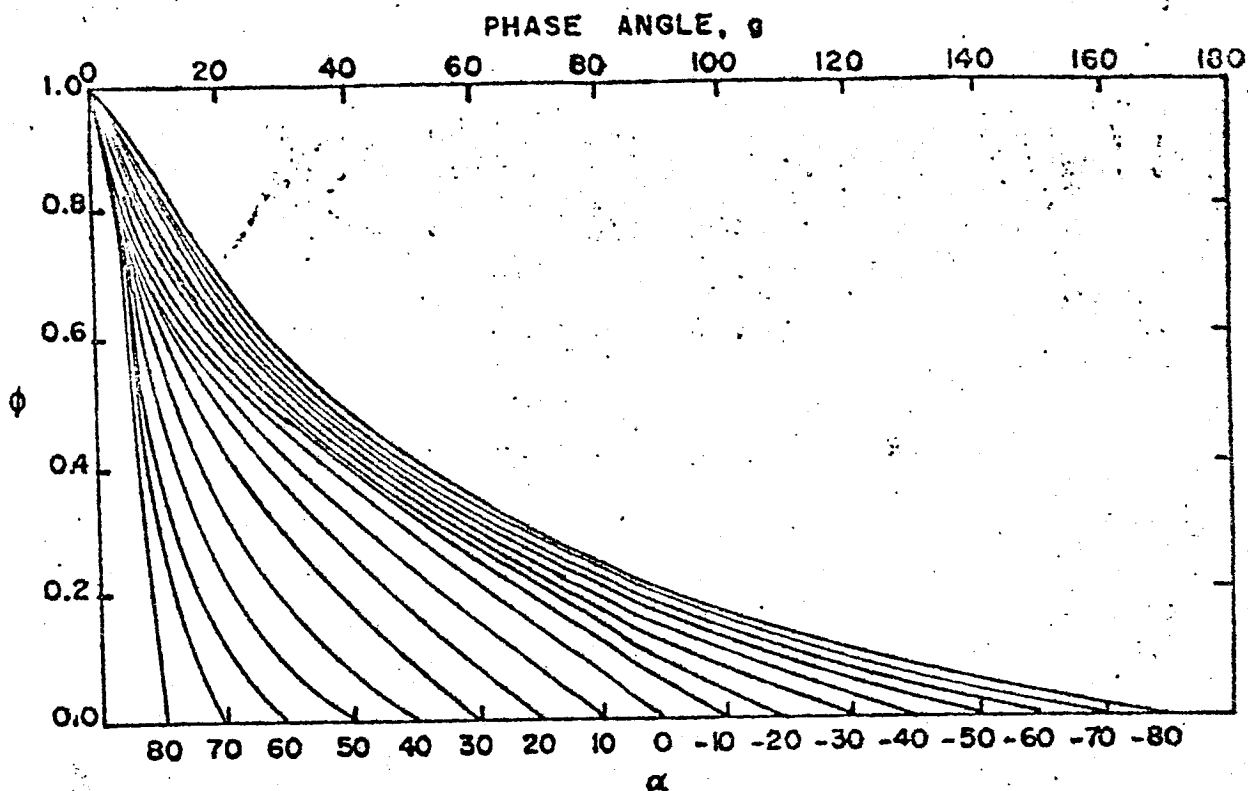
3.1.1

Geometrical Effects

The photometric function derived by Fedorets (Reference 4), reproduced as Figure 3.1-1, has been used to determine relative surface brightness variation due to changing the geometry of sun angle, viewing angle, and surface slope. In order to examine the effects of these factors, some assumptions have been made to simplify derivation of near-limiting cases. The assumptions and conditions used are as follows:

- The values of reflectivity are determined in the plane of illumination.
- The camera axis is toward the nadir.
- The sun angle is at 50° and 75° from vertical (40° and 15° solar elevation at the nadir points).
- Surface slopes 0° , 5° , 10° , 15° and 30° from horizontal falling both toward and away from the sun and the 2 m. by 0.5 m cone are considered.
- The photometric function given by Fedorets will be assumed for all surfaces.

By restricting consideration to the plane of illumination, maximum and minimum values will be obtained. The angles of view for the cameras are 21° (10.5° half angle across the long axis of the high resolution camera, and 57.5° (28.75° half angle) for the low resolution camera. The maximum slope angle considered (30°) is taken as representing crater walls, although higher slopes may be encountered in some craters and on ejecta blocks. The standard 2 meter cone has a slope of 26° .



Photometric function of lunar maria, according to Fedorets. ϕ vs. g

Figure 3.1-1

The photometric function derived by Fedorets is an average. The character of the lunar surface is not uniform and the photometric function varies somewhat. This has been shown by Sytinskaya and Scharonov in their plots of the variation in brightness of particular locations as a function of phase angle. These plots are similar to Fedorets photometric function, with the angle of reflection (α) held constant by the location of the area on the moon. To illustrate the variations which have been observed for different areas, six of their plots have been re-drawn and are presented in Figure 3.1-2.

Two sun angles, lines of sight both on camera axis and off axis, and surface slopes have been used in various combinations to investigate the effects on observed surface reflectivity. The geometrical relationships for this study are illustrated in Figure 3.1-3.

3.1.2 Albedo

The photometric properties of the moon have been studied extensively (Reference 1)* and the brightness of lunar features has been measured (References 2 and 3*). The albedos reported for some representative areas are listed in Table 3.1-1. These values are averaged over areas which are at least comparable with the field of view of the high resolution camera. It should be expected that variations at least as great and quite possibly greater than those reported for different areas may occur in some locations within the camera field of view due to terrain features not presently resolvable. On the basis of the brightness measurements, the maximum range of brightness due to albedo differences is about 3 (0.06 to 0.18) or about 1.5 photographic f. stops. The photometric function, ϕ , is a factor by which the normal albedo is decreased by deviation of line of sight, phase angle, or both from normal.

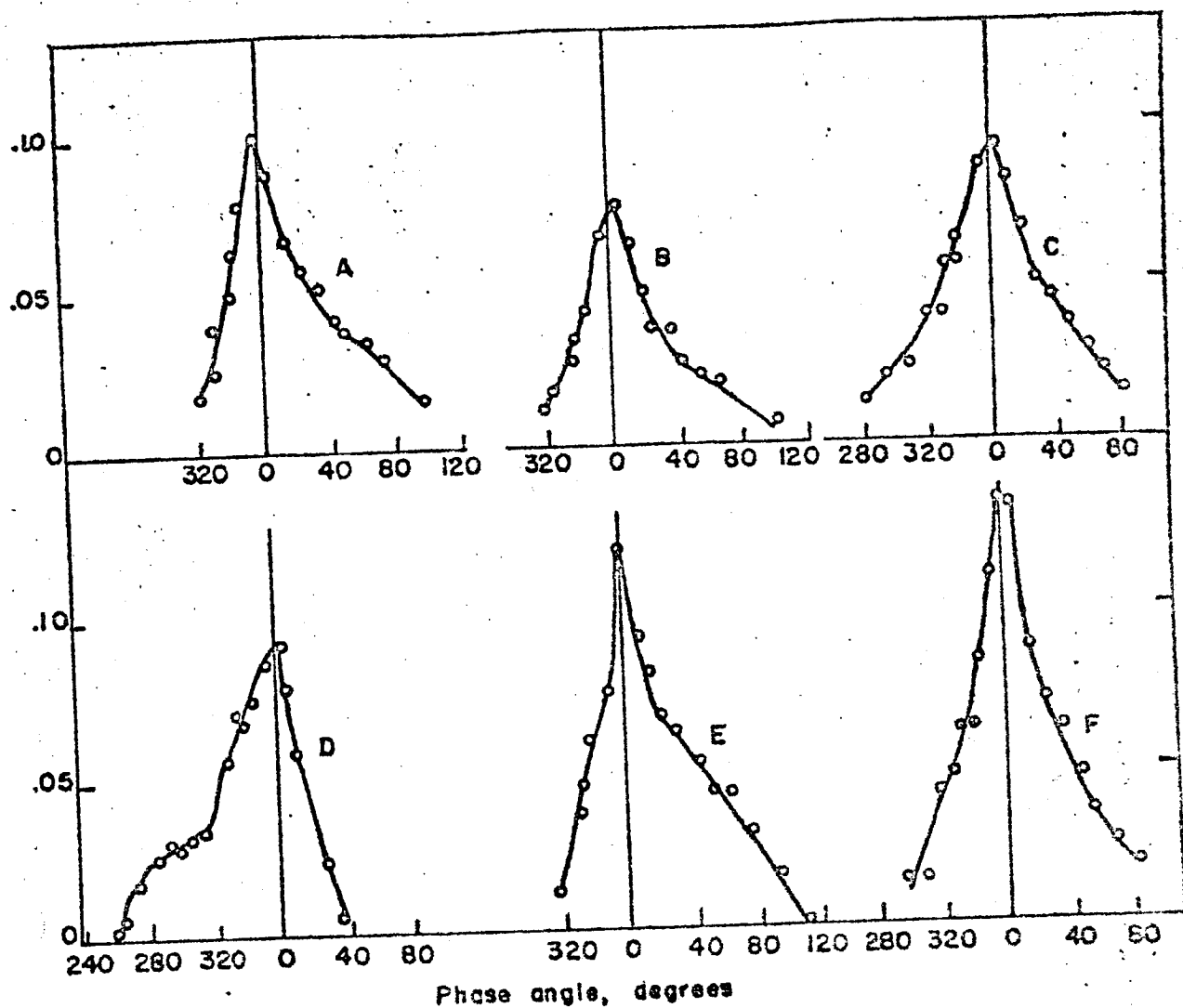
Albedo values which have been reported in the literature must be considered only as good approximations because of the limitations imposed by Earth-based observation. While brightness measurements under differing angles of illumination are readily obtained, depending upon the lunar phase, variations in the angle α are limited by the lunar libration. The brightness of features away from the central portion of the visible disk, when observed from directly above, as from an orbiting vehicle, must be computed on the basis that the photometric function is valid. Assumption that the albedo under vertical line of sight will closely follow that observed from Earth is probably reasonable. Under full moon lighting, virtually no limb darkening is observed, indicating that when α and θ are both equal to 0, maximum brightness is achieved.

*References listed on Page 88.

Albedoes of Lunar Areas:

| Maria | Location | | Albedo |
|-----------------------------------|----------|------|--------|
| Tranquillitatis | 9°N | 29°E | 0.066 |
| Serenitatis | 26°N | 28°E | .070 |
| Nectaris | 15°S | 33°E | .080 |
| " | 7°S | 26°E | .089 |
| Vaporum | 10°N | 8°E | .062 |
| Sinus Medii | 7°N | 8°W | .054 |
| Sinus Medii | 1°N | 2°W | .076 |
| Imbrium | 26°N | 0° | .074 |
| " | 31°N | 17°W | .064 |
| Oceanus Procellarum | 6°N | 16°W | .070 |
| " | 9°S | 24°W | .071 |
| " | 15°N | 42°W | .060 |
| " | 4°S | 54°W | .056 |
| Upland Areas | | | |
| | 4°S | 35°E | .104 |
| | 3°S | 22°E | .118 |
| | 9°N | 13°E | .090 |
| | 2°S | 12°E | .123 |
| | 11°S | 12°E | .125 |
| | 7°N | 2°E | .104 |
| | 5°S | 0° | .108 |
| Appenine Mts. | 17°N | 2°W | .082 |
| | 3°S | 8°W | .112 |
| Individual Features | | | |
| Floor of Julius Caesar | | | .074 |
| Floor of Flamsteed and Theophilus | | | .088 |
| Floor of Ptolemaeus | | | .162 |
| Floor of Copernicus | | | .120 |
| Walls of Copernicus | | | .156 |
| Rays from Copernicus | | | .122 |
| Region near Kepler | | | .115 |
| Central Mountain of Aristarchus | | | .183 |

TABLE 3.1-1

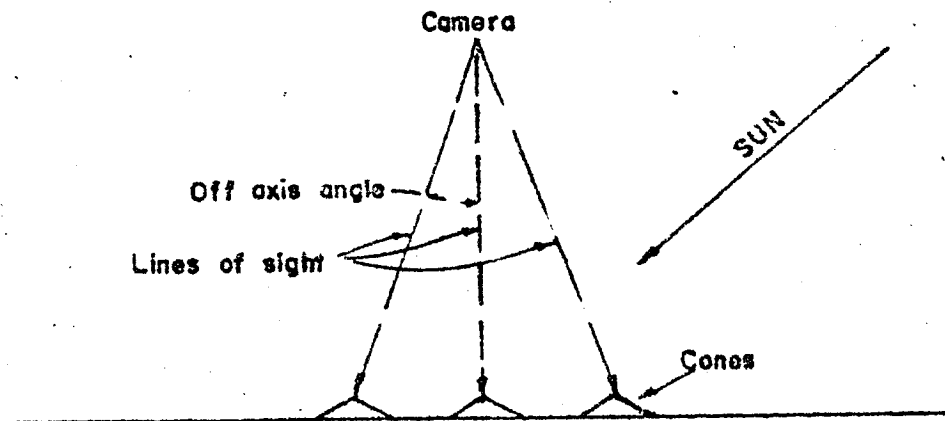
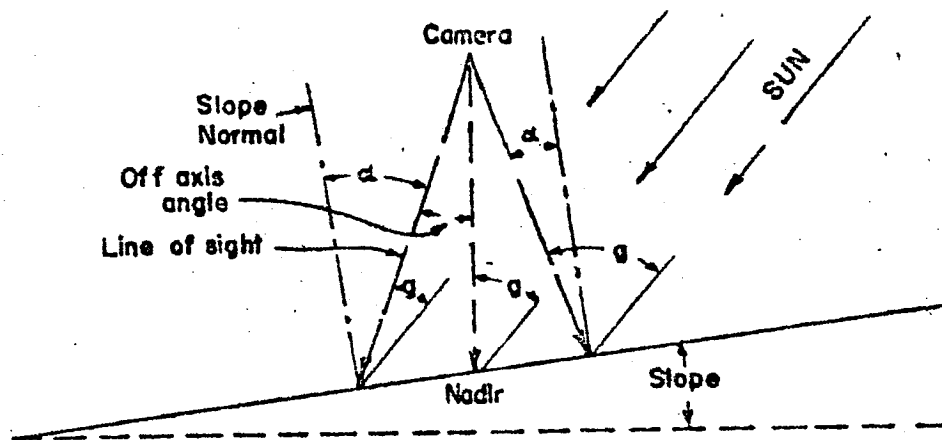
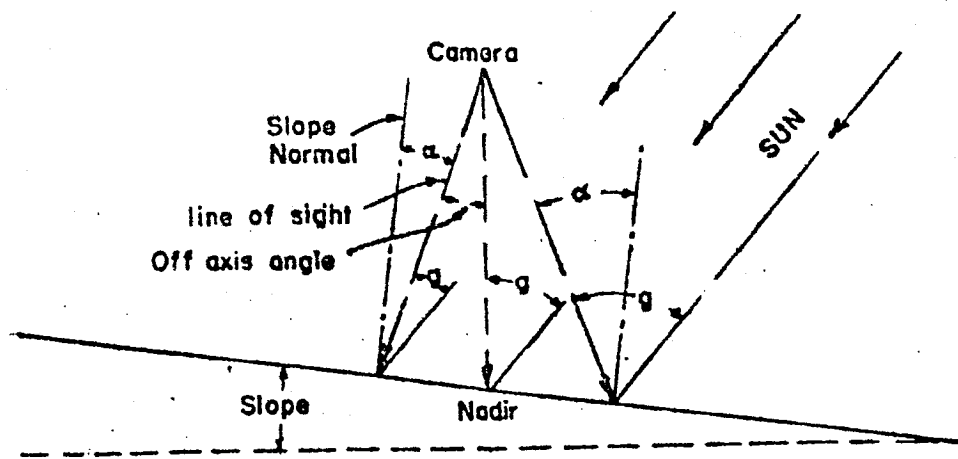


- A. Mare Nectaris, north central part
 B. Mare Tranquillitatis, south eastern part
 C. Sinus Medii
 D. South rim area of Kepler
 E. Upland between Mare Fecunditatis and Mare Nectaris
 F. Upland

7°S 26°E
 2°S 27°E
 1°N 2°W
 7°N 35°W
 4°S 25°E
 11°S 12°E

The apparent brightness of different details on the lunar surface as a function of phase angle before and after full moon. After Sytinskaya and Scharonov, *Uchen. Zapiski Univ. Leningrad* No. 153, 1952.

Figure 3.1-2



Geometrical relationships affecting surface reflectance. Line of sight and slopes assumed in plane of illumination.

Figure 3.1-3

Albedo values are given for visible light. While there are no prominent colors apparent on the moon's surface, photometric measurements through filters of narrow spectral transmission have shown small differences in color indices. Thus, some small variation will occur if measurements are made by limited wavelengths or in the I.R. or U.V. Just as greater differences may be expected in albedo as resolution is increased, it is possible that more prominent color differences may occur between small feature detail, particularly in regions where exposed rock occurs. It is unlikely, however, that such differences will be of particular significance to photograph requirements of the LO system.

3.2

Determination of Contrast Ratios

Brightness differences, whether occurring between adjacent areas or between more widely separated positions may be expressed as contrast ratios which readily may be related to the capabilities or requirements of a photographic system. Where a uniform albedo of the surface within the area being considered may be assumed, contrast ratios conveniently may be determined on the basis of relative brightness or reflectance as computed from the photometric function. Where albedo variation must be taken into account, reflectance values obtained as a product of the albedo, ρ , and the value of the photometric function, ϕ .

The contrast ratio also may be expressed in terms of the equivalent difference of photographic f. stop, Δf . Contrast ratio is related to Δf by the equation,

$$\Delta f = \frac{\log \frac{B_1}{B_2}}{\log 2}$$

where $\frac{B_1}{B_2}$ is the ratio of brightness values and is greater than 1.

As shown in Section 3.1, contrasts may be due to geometrical relationships between surface configuration, and the angles of illumination and of line of sight, to albedo differences, or to combinations of both. On a single photograph, the cause of a contrast cannot be definitely established unless there is sufficient additional information to permit recognition of the feature. Recognition and identification of a feature is largely dependent upon the relation between the size of the feature and resolution, the latter, again, being a function of the contrast ratio. This is discussed in detail in Section 4.0.

| Phase at Radir | Slope Direct- ion | Slope Angle | ϕ at Radir | 5° OFF-AXIS LINE OF SIGHT | | | | 10° OFF-AXIS LINE OF SIGHT | | | | 15° OFF-AXIS LINE OF SIGHT | | | |
|----------------------|-------------------------|----------------|-----------------------|---------------------------|------|------------|-------------------------|----------------------------|-------|------------|-------------------------|----------------------------|------|------------|-------------------------|
| | | | | δ | | Δf | $\frac{\Delta f}{\rho}$ | δ | | Δf | $\frac{\Delta f}{\rho}$ | δ | | Δf | $\frac{\Delta f}{\rho}$ |
| | | | | Toward Sun | Away | | | Toward Sun | Away | | | Toward Sun | Away | | |
| 50° | TOWARD | 0 | 0.30 | 0.28 | 0.32 | 1.152 | 0.062 | 0.21 | 0.251 | 0.33 | 1.330 | 0.124 | 0.41 | 0.23 | 1.541 |
| | | 5 | .31 | .29 | .34 | 1.181 | .072 | .24 | .26 | .35 | 1.316 | .139 | .24 | .28 | 1.555 |
| | | 10 | .32 | .30 | .35 | 1.182 | .073 | .24 | .27 | .35 | 1.309 | .149 | .25 | .29 | 1.555 |
| | | 15 | .33 | .30 | .36 | 1.191 | .076 | .25 | .28 | .37 | 1.305 | .145 | .25 | .29 | 1.555 |
| | | 20 | .34 | .31 | .37 | 1.176 | .070 | .23 | .29 | .37 | 1.376 | .139 | .26 | .28 | 1.555 |
| | | 30 | .36 | .33 | .38 | 1.167 | .067 | .22 | .30 | .41 | 1.370 | .137 | .28 | .28 | 1.555 |
| | | | | | | | | | | | | | | | |
| 75° | | 0 | 0.11 | 0.10 | 0.12 | 1.190 | 0.076 | 0.25 | 0.09 | 0.12 | 1.402 | 0.147 | 0.45 | 0.02 | 1.451 |
| | | 5 | .13 | .12 | .15 | 1.219 | .086 | .29 | .11 | .15 | 1.522 | .182 | .10 | .15 | 1.710 |
| | | 10 | .15 | .13 | .16 | 1.218 | .086 | .29 | .12 | .13 | 1.492 | .174 | .11 | .20 | 1.790 |
| | | 15 | .16 | .15 | .18 | 1.220 | .086 | .29 | .13 | .20 | 1.482 | .171 | .12 | .22 | 1.811 |
| | | 20 | .18 | .16 | .20 | 1.240 | .093 | .31 | .15 | .22 | 1.471 | .168 | .13 | .24 | 1.786 |
| | | 30 | .20 | .18 | .22 | 1.210 | .083 | .28 | .16 | .24 | 1.439 | .158 | .15 | .25 | 1.745 |
| | | | | | | | | | | | | | | | |
| 50° | AWAY | 0 | 0.30 | 0.28 | 0.32 | 1.152 | 0.062 | 0.21 | 0.25 | 0.33 | 1.330 | 0.124 | 0.41 | 0.23 | 1.541 |
| | | 5 | .28 | .26 | .29 | 1.116 | .048 | .26 | .24 | .37 | 1.255 | .102 | .34 | .22 | 1.470 |
| | | 10 | .25 | .24 | .25 | 1.060 | .025 | .06 | .22 | .27 | 1.202 | .080 | .27 | .20 | 1.421 |
| | | 15 | .21 | .21 | .22 | 1.050 | .021 | .07 | .20 | .22 | 1.137 | .056 | .19 | .18 | 1.298 |
| | | 20 | .17 | .16 | .18 | 1.071 | .030 | .01 | .16 | .13 | 1.091 | .038 | .13 | .16 | 1.220 |
| | | 30 | .09 | .08 | .09 | 1.071 | .030 | .01 | .08 | .03 | 1.071 | .030 | .10 | .08 | 1.334 |
| | | | | | | | | | | | | | | | |
| | | | | | | | | | | | | | | | |
| 75° | | 0 | 0.11 | 0.10 | 0.12 | 1.190 | 0.076 | 0.25 | 0.09 | 0.12 | 1.402 | 0.147 | 0.45 | 0.02 | 1.451 |
| | | 5 | .08 | .07 | .08 | 1.125 | .052 | .17 | .05 | .09 | 1.238 | .093 | .31 | .05 | 1.474 |
| | | 10 | .04 | .04 | .04 | 1.000 | .000 | .03 | .04 | .04 | 1.166 | .067 | .22 | .03 | 1.400 |
| | | 15 | .00 | .00 | .00 | 0 | 0 | 0 | .00 | .00 | 0 | 0 | 0 | .00 | 0 |
| | | 20 | .00 | .00 | .00 | 0 | 0 | 0 | .00 | .00 | 0 | 0 | 0 | .00 | 0 |
| | | 30 | .00 | .00 | .00 | 0 | 0 | 0 | .00 | .00 | 0 | 0 | 0 | .00 | 0 |

TABLE 3.3-1
VARIATIONS OF IDEAL SURFACE BRIGHTNESS RATIOS DUE TO OFF-AXIS
LINE-OF-SIGHT, AS A FUNCTION OF SLOPE AND SUN ANGLE

12-100893-1
PAGE 65

To the present time, the observations and measurements by Fedorets (1951), Sytinskaya and Scharonov (1952), Sytinskaya (1953), Fessenkov (1962) and others have provided the basis for studies involving lunar photometric measurements. The recent marked increase in lunar studies has resulted in the initiation of new and more accurate photometric measurements. Among the studies currently in progress are those by R. W. Shorthill of the Boeing Scientific Research Laboratories and by Howard A. Phon, U.S.G.S. Astrogeology Research Laboratory, Flagstaff, Arizona. Data from the above programs, directly applicable to the present study, is not yet available.

Lunar photometric measurements have been made by two basic methods, photographic and direct. In the first method, the moon is photographed with an astronomical telescope. Rigid control is maintained at all stages of the photographic process to retain photometric accuracy of the photographic image. Microdensitometer measurements of the photograph are made and surface brightness computed from the recorded transmission values. By this technique measurements may be made over the visible area at essentially the same instant in time and in detail limited only by the resolution of the photograph. In addition, other scans may be made at any subsequent time. The technique is subject to the errors inherent in the photographic process, such as non-uniformity of the film or the processing, as well as those arising from degradation of the image by atmospheric effects such as turbulence and absorption.

The second technique involves direct measurement by photometric scanning of the image at the focal plane of the telescope. In general, the minimum practical size of the sensor results in brightness values integrated over areas of 10 kilometer diameter or larger as compared with about 1 kilometer by the photographic technique. In his recent measurements, Shorthill integrated values over a circular area equivalent to about 10 kilometers on the moon, and Phon will be using a sensor covering about 20 kilometers. Precise control of telescope guidance throughout a scan is essential to ensure proper correlation between the photometer record and the corresponding position on the moon. Calibration and standardization of instrumentation must be frequent and very carefully done. For example, Phon bases his measurements on a comparison of twelve stars chosen for their known brightness and spectral characteristics and their positions with reference to the moon's position in the sky. Wilkey and Phon (Reference 5) have reported a standard error amounting to about 4% in preliminary direct photometric measurements of 25 lunar features made using the Mt. Wilson 60 inch reflector.

3.3

Variations in Contrast Ratios

3.3.1

Target Model Studies

It has been shown that, because of the photometric characteristics of the lunar surface, if the surface slopes across the field of view, modification of brightness will occur as a result of changed geometry. Considering the field of view of the camera system, off-axis line of sight will occur except at the nadir point. The geometrical relationships which determine reflectance will be further modified as the line of sight deviates from the camera axis. It is seen, then, that even with a uniform surface, a brightness difference across the field of view will occur. This effect is illustrated in Figure 3.3-1 in which the brightness ratio across a field, defined by a half angle corresponding to off-axis angles of 5° , 10° , and 15° , is plotted as a function of surface slope. Sun angles of 50° and 75° have been used, and values computed only for the plane of illumination.

For the purpose of analytical study of the factors determining contrast ratios, symmetrical cones have been used as target models for simulation of terrain features. The cones, having a known slope, will exhibit predictable contrast ratios when illuminated at known angles and may be related to equivalent bar charts in considering resolution of the photograph system. The target cone and bar chart established for the limiting resolution is shown in Figure 3.3-2.

When a cone is illuminated at some angle from the normal to the base, the surface brightness will grade from a maximum in the plane of illumination on the side facing the light source to a minimum in the same plane on the opposite side. This is illustrated in Figure 3.3-3. The maximum-minimum contrast ratio across the cone, having a uniform surface conforming to Fedorets photometric function, as a function of sun angle is shown in Figure 3.3-4. On-axis line of sight has been assumed.

Variation of line of sight angle will influence both the apparent phase angle, g , and the angle α . As a result, the maximum-minimum contrast ratio across the cone model will be changed significantly. Again, assuming a surface of uniform albedo and photometric characteristics, the maximum-minimum contrast across the cone as a function of off-axis line of sight in the plane of illumination has been computed on the basis of Fedorets photometric function. This has been plotted in Figure 3.3-5 for the limiting sun angles of 50° and 75° .

The slope of the cone is 26.6° . At a sun angle of 75° from zenith, the slope opposite the sun will be in hard shadow and contrasts across the cone would be meaningless. For this case, the contrast has been taken as the ratio between the illuminated side of the cone and a level surface according to the relation

VARIATIONS IN RELATIVE BRIGHTNESS WITH OFF AXIS LINE OF SIGHT, AS A FUNCTION OF SURFACE SLOPE AND SUN ANGLE

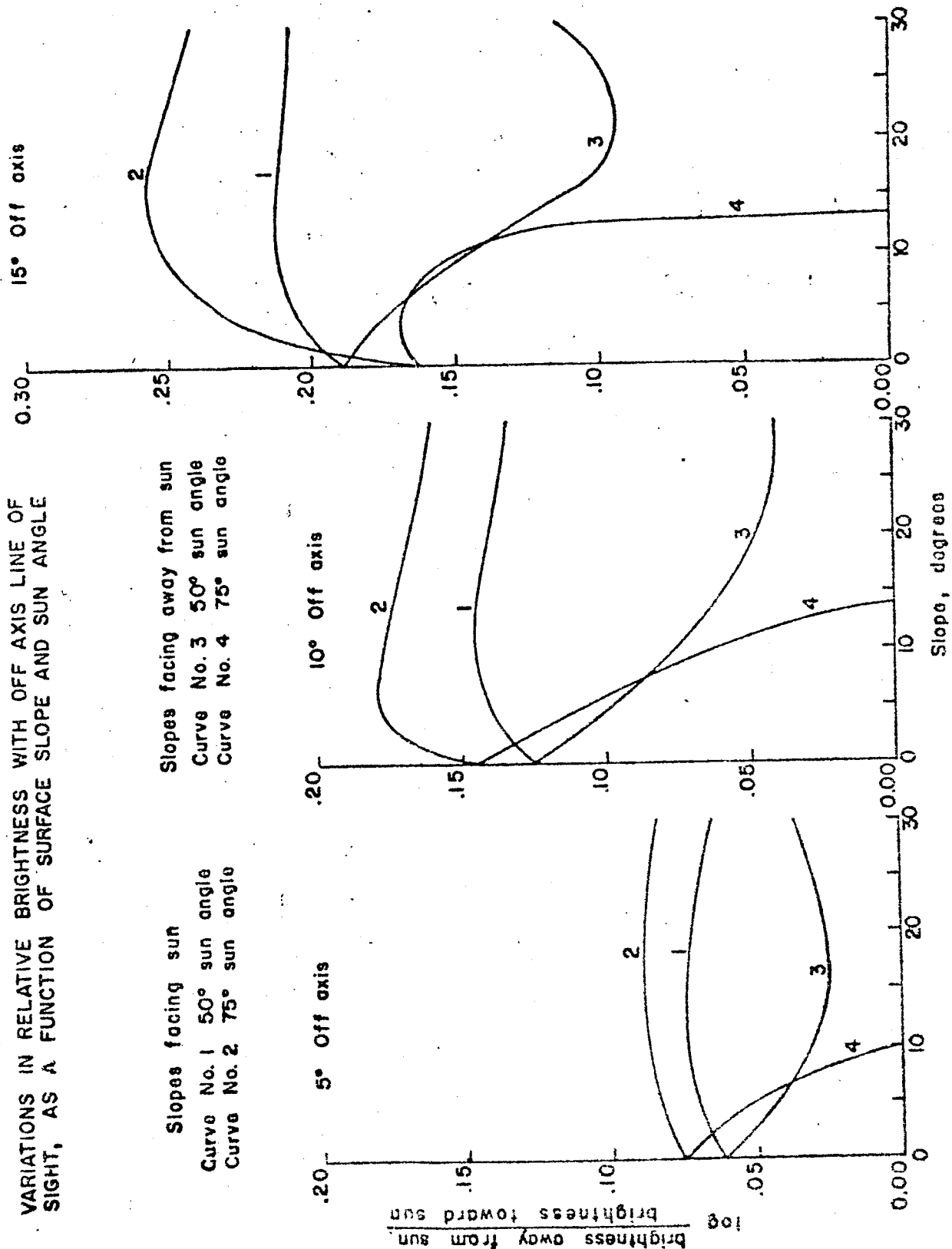


Figure 3.3-1

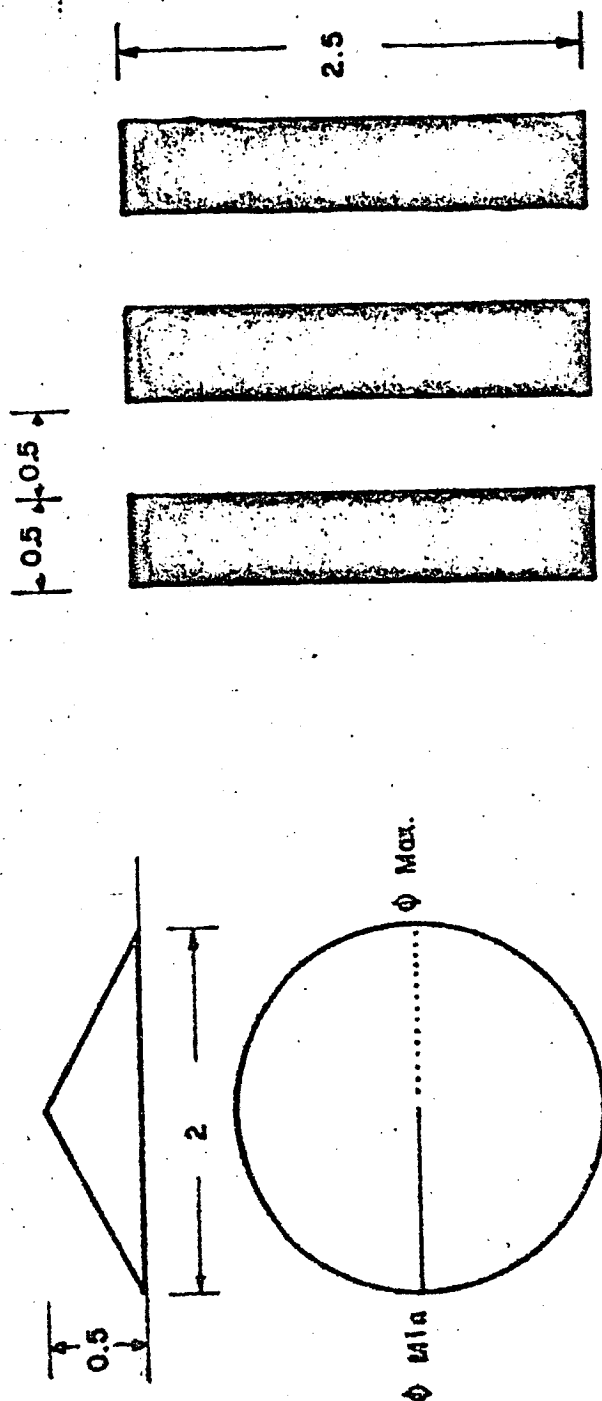
DOEING

VOL
SEC.

NO D2-100293-1
PAGE 68

Sun

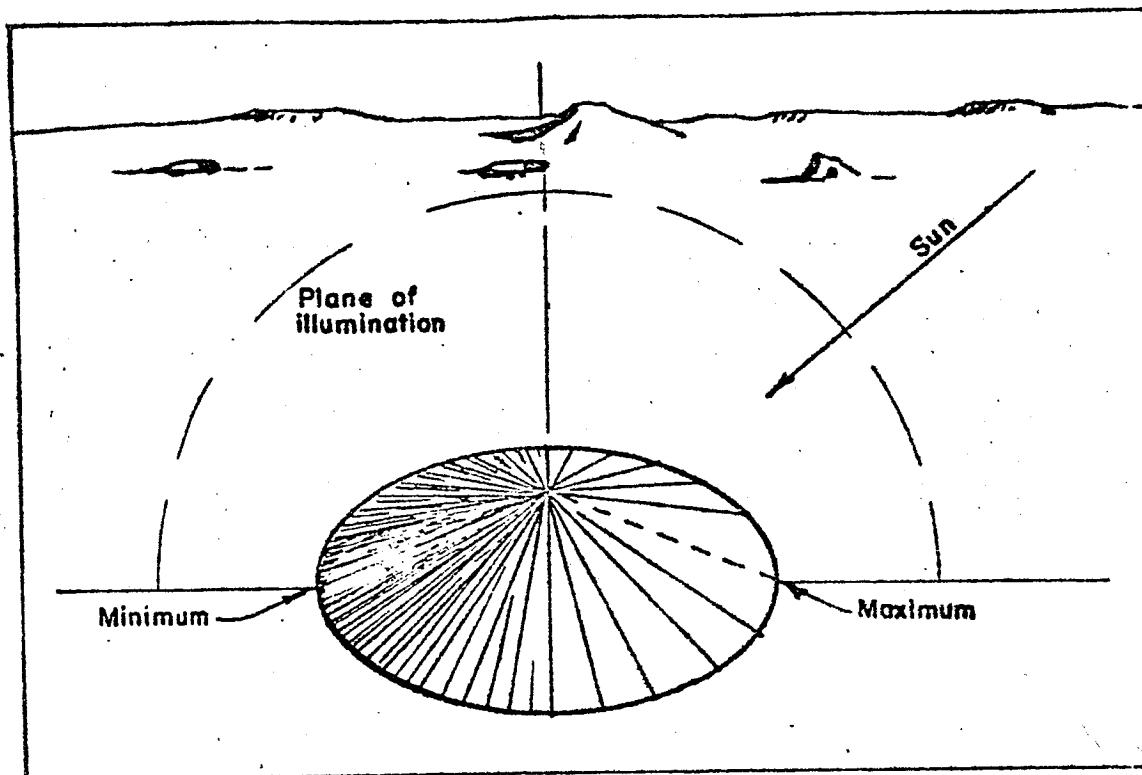
Dimensions in meters



NASA Targets at limiting resolution

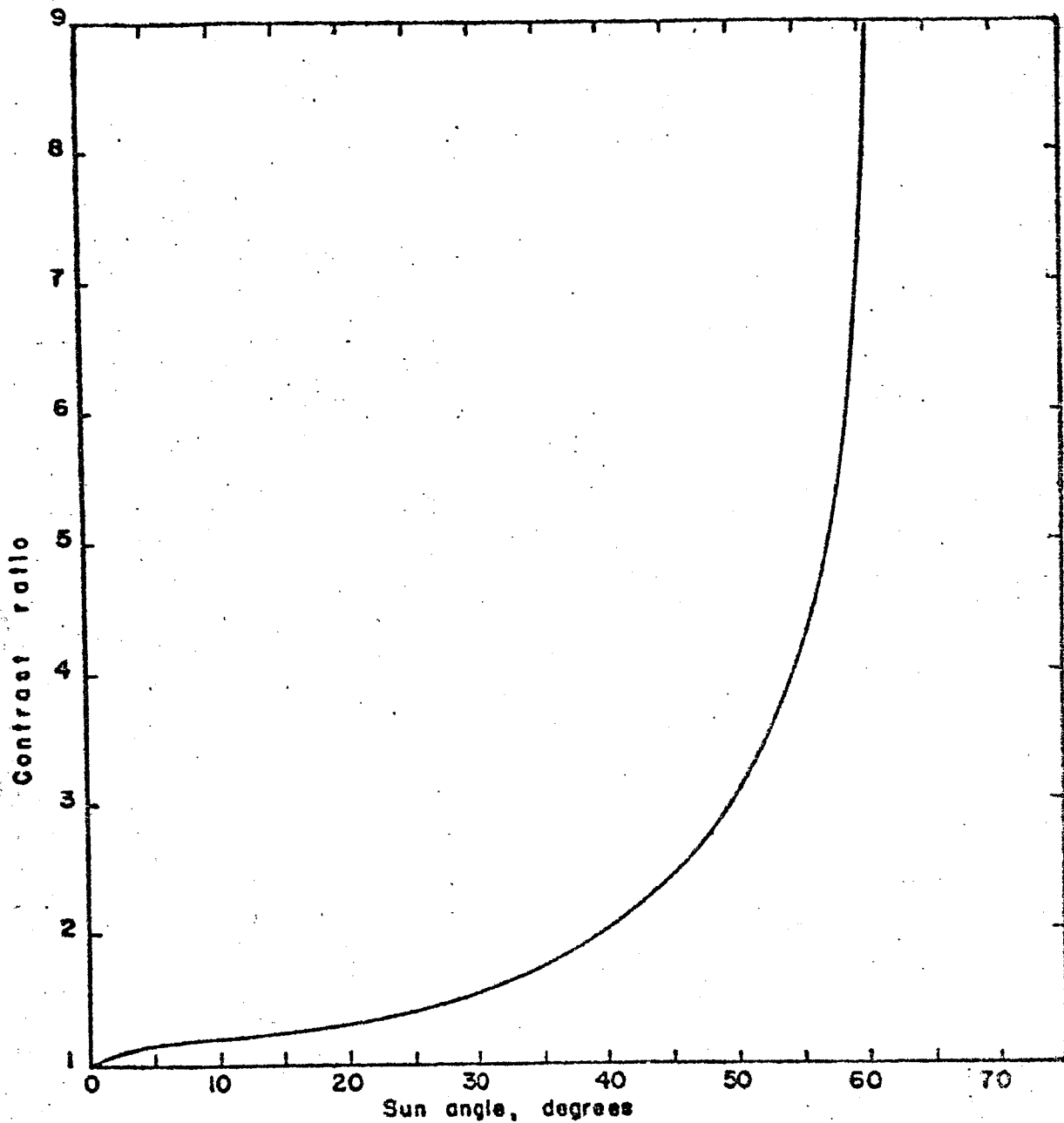
Figure 3.3-2

2-5143-1



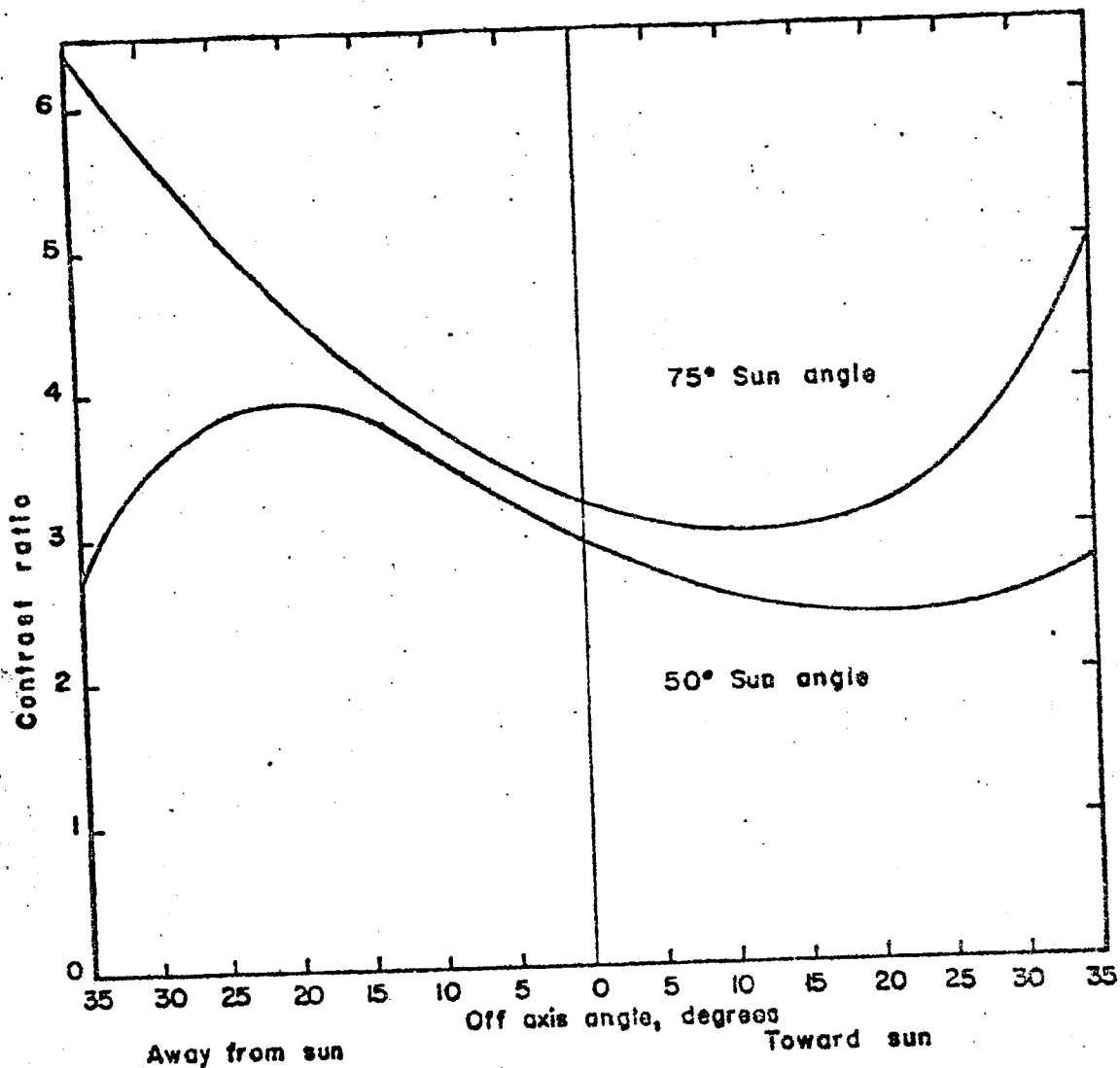
The illumination of a target cone.

Figure 3.3-3



Maximum-minimum contrast ratio across a 2 meter base, 0.5 meter high cone as a function of sun angle.

Figure 3.3-4



Contrast ratio across a 2 meter base 0.5 meter high cone as a function of off axis line of sight with sun angles of 50° and 75°.

Figure 3.3-5

$$\text{Contrast ratio} = \left(\frac{R_c}{R_l} \right)^2$$

where R_c and R_l are the reflectances of the cone surface and level surface, respectively.

3.3.2 Lunar Surface Photometric Variations

During an orbital pass of the Lunar Orbiter, changes will occur in phase angle, local slope of the surface, and the albedo, producing changes in the brightness of the surface. Phase angle at the nadir will vary at a rate determined by orbital velocity and inclination to the illumination plane. Variations due to slope and albedo will occur at irregular frequency and amplitude, depending upon the nature of the surface being crossed.

A traverse of 200 km along a lunar great-circle amounts to 6.60° . Since the orbital travel time will be only about 2.4 minutes, the effect of the lunar rotation on illumination angle can be disregarded. The change in illumination angle will thus be 6.6° where the traverse is in the plane of illumination. Where the orbit is inclined to the illumination, the change will amount to $(6.6) \cos \theta$, where θ is the angle between the orbit plane and the illumination equator. Between illumination angles of 50° and 75° , the maximum effect of the 6.6° change will amount to a $\Delta \phi$ of 0.05, but because of the changed phase, the ratio of brightness across traverse will increase as the phase is increased. This is shown in Table 3.3-2.

The albedo of the lunar surface is not uniform, as shown in Table 3.1-1. In traversing a 200 km distance, it is possible that the path may cross areas of both high and low albedo, such as recent rayed craters on the dark maria, or crossing from maria to continental or upland areas. As shown, the surface luminance will also be a function of solar phase. Assuming, again, that the photometric function is the same for all areas, these variations may be expressed as contrast ratio or as differences in photographic f. stops. The surface reflectance is the product of albedo and ϕ . Using the values of ϕ given in Figure 3.1-1 and values for albedo given by Sytinskaya in Table 3.1-1, some exposure differences across various features have been computed and tabulated in Table 3.3-3. Because of the limited number of areas for which albedo values are available, the areas used in the calculations are not necessarily within 200 km of each other, but are taken as representative of similar features.

It can be seen from the albedos listed in Table 3.1-1 that more extreme differences can occur. It was pointed out that these albedos are values which are averaged over an area of several square kilometers, depending upon the optical system and sensor used in the measurement. Brightness of detail below resolvable size must span a range of values above and below the average.

Effect of 6.6° traverse on surface contrast.

| SUN ANGLE () | ϕ | $\Delta\phi$ | $\frac{\phi}{\phi}$ | Δf |
|---------------|--------|--------------|---------------------|------------|
| 50° | .298 | .051 | 1.21 | 0.27 |
| 56.6° | .247 | | | |
| 68.4° | .156 | .050 | 1.47 | 0.56 |
| 75° | .106 | | | |

TABLE 3.3-2

Contrasts due to albedo differences across a 200 kilometer traverse

| | RATIO ϕ/ϕ | Δf |
|---|----------------------|------------|
| Copernicus, bottom ($\rho = .120$) to Sinus Medii ($\rho = 0.054$) at $g = 50, 56.6, 68.4, 75^\circ$ | 2.23 | 1.16 |
| Copernicus, bottom at 50° to Sinus Medii at 56.6° | 2.72 | 1.44 |
| Copernicus, bottom at 68.4° to Sinus Medii at 75° | 3.28 | 1.72 |
| Copernicus, bottom at 56.6° to Sinus Medii at 50.0° | 1.90 | 0.93 |
| Copernicus, bottom at 75.0° to Sinus Medii at 68.4° | 1.52 | 0.60 |

TABLE 3.3-3

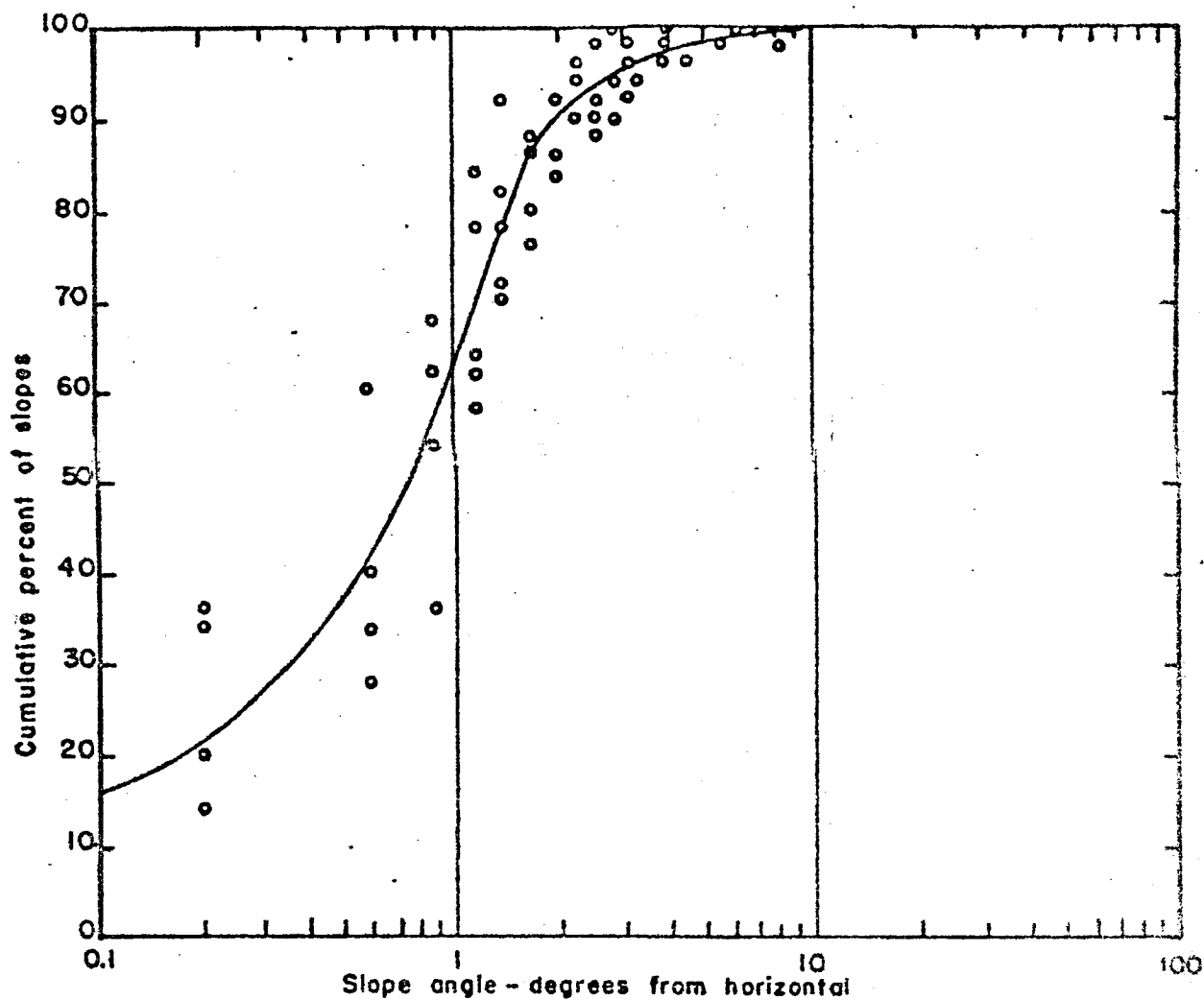
This effect will accentuate the differences shown in Table 3.3-3. A photographic exposure difference equivalent to at least two f. stops and perhaps four may exist under such a circumstance. It should be expected that such variation will occur within a 200 km lunar traverse, and possibly within the field of view of the camera.

The frequency and amplitude of surface brightness variation will be strongly dependent upon the type of terrain over which a sensor scans, and the area over which the sensor integrated reflected light. It has been shown that variations in surface brightness is strongly dependent upon slopes. The occurrence of slopes will, then, be indicative of brightness variation, the magnitude and frequency being a function of terrain roughness in areas of uniform albedo. Because of present limitations on resolution to about 1 to 2 kilometers resolution of brightness variations can be no better. A brief study has been made of the occurrence of slopes on the lunar mare surface. An attempt was made to derive the distribution of slopes in the best detail afforded by the A.C.I.C. Lunar Atlas Charts. Slopes averaged over 2 kilometer increments of a 500 km profile along 14° S. latitude running east from 28° W. Longitude. The distribution curve is reproduced as Figure 3.3-6. Data points for the slope distributions within 100 kilometer segments were included to indicate variability of terrain within the complete section. No mountainous terrain was crossed by the section. The maximum slope found was 10°, but between 96% - 98% of the measured slopes were less than 5°, while between 40 - 70% were less than 1°. It would appear that over the maria, variations in surface brightness due to slopes will not be a serious problem.

In the case of the upland areas, which generally include comparatively rugged terrain, the problems will be of more concern.

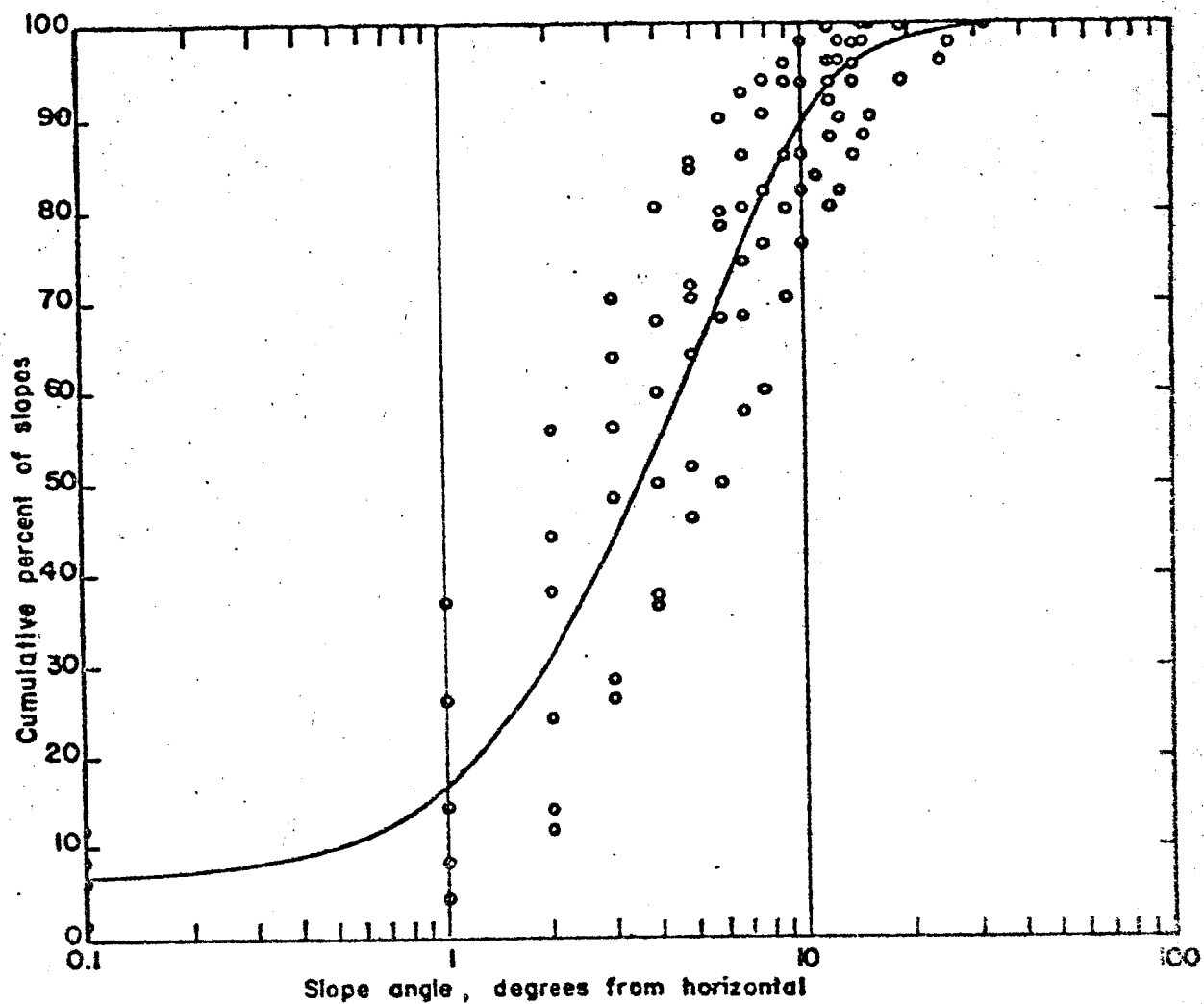
Two profiles across upland areas were drawn from LAC 77, Ptolemaeus. The first was along 4° S. latitude from 10° W to 2° E. longitude and the second along 6° S. latitude from 10° W to 0° longitude. Slopes were computed from the measured elevations between successive 2 kilometer intervals of horizontal distance. A plot of cumulative percent of slopes as a function of slope angle is shown in Figure 3.3-7. Distribution within 100 kilometer segments were also determined and the data points plotted to provide some indication of terrain variability. It should be understood that this curve represents an example of upland terrain, but it is not necessarily representative of all upland areas.

The more rugged nature of the uplands in comparison with the maria becomes apparent in the difference between slope distribution as shown in Figure 3.3-8. While the mare area is shown to have about 60% of its slopes less than 1°, the upland area has but 15%. The upland areas will, as a result, have a larger and more frequent variation in reflectivity during a traverse, due to the slope dependence of the surface photometry.



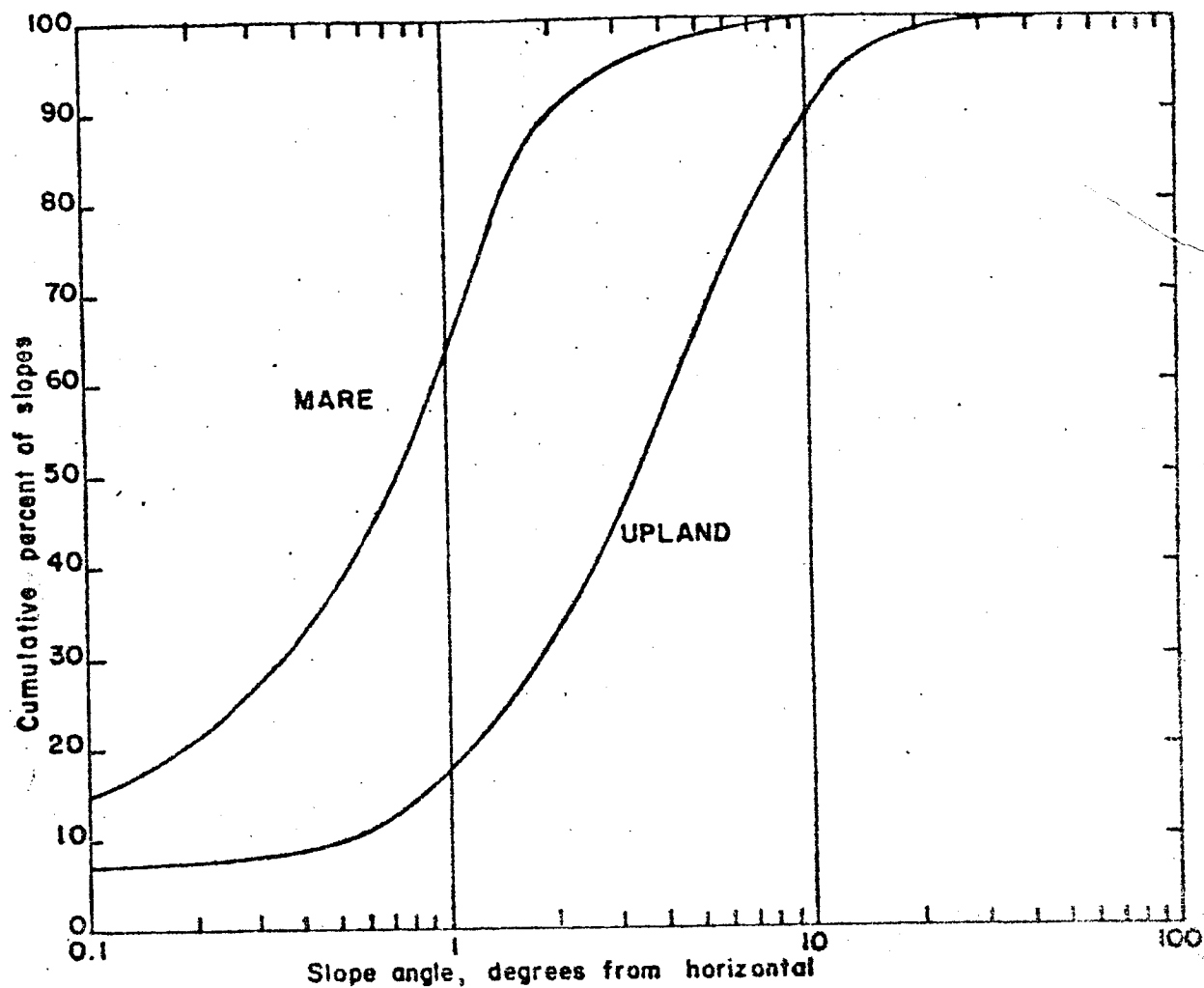
Distribution of slopes on a lunar mare area. Slopes averaged over two kilometer intervals of a 500 kilometer profile. Data points for 100 kilometer segments.

Figure 3.3-6



Distribution of slopes on a lunar upland area. Slopes averaged over two kilometer intervals of a 625 kilometer profile. Data points for 100 kilometer segments.

Figure 3.3-7



Distribution of slopes on lunar mare and upland areas. Slopes averaged over two kilometer intervals.

Figure 3.3-8

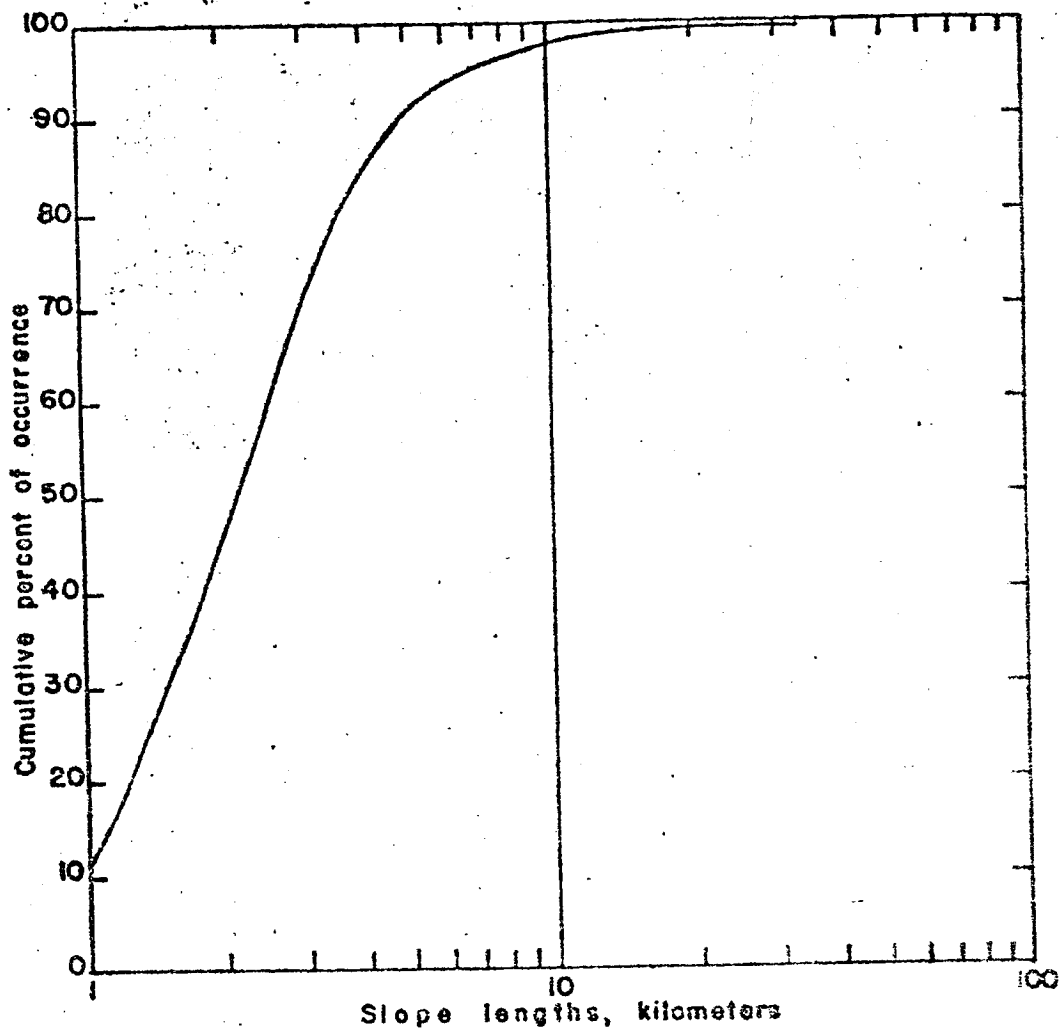
The distances between major slope changes will give an indication of the frequency of occurrences of brightness differences due to terrain features. The horizontal distance between the major slope changes was measured on the profile drawn for the upland areas, and the cumulative percent of occurrence computed as a function of length. This data has been plotted as Figure 3.3-9. It is seen that the mean distance between slope changes is about 2 kilometers and that over 98% are less than 16 kilometers, the long dimension of the high resolution camera field of view. If an equal probability of rising and falling slopes is assumed, this would indicate that about half the time, slopes in opposite directions would appear at either side of the photograph and result in increased contrasts.

At perilune altitude, the vehicle velocity over the ground is 2.2 kilometers per second. Thus, the light fluctuations at the nadir point will have a mean frequency of about 1 per second or 0.5 cycle/sec. from the larger terrain features. Small surface detail which cannot be resolved at present will undoubtedly introduce additional higher frequency variations which may likely have equal or greater amplitude than indicated by slopes obtained from current lunar surface contouring.

An attempt was made to estimate the occurrence of shadows in the upland areas on the basis of the profile prepared from the ACIC Chart. Slopes were checked graphically using a small template prepared to represent the two sun angles of 50° and 75° on the 10:1 vertical exaggeration of the profile. Where shadows were indicated by slopes equal to or exceeding the template, their horizontal length was measured. No attempt was made to alter the sun angle along the traverse and thus the measurements reflect values for a constant sun angle at the nadir point. As a simple check, shadow determinations were made for both morning and evening direction of illumination. The results obtained from the measurements along the 660 kilometers of profile are listed below:

| | Morning | | Evening | |
|----------------------------|---------|---------|---------|---------|
| | 50° Sun | 75° Sun | 50° Sun | 75° Sun |
| Total length measured | None | 59.6 km | None | 55.5 km |
| Percent of length shadowed | 0 | 8.9% | 0 | 8.4% |
| Average length of shadows | 0 | 1.8 km | | 1.6 km |

The above measurements agree reasonably well with the slope distribution curve (Figure 3.3-7) which was obtained by averaging slopes over 2 kilometer distance. The method used here can indicate only gross shadows and gives no information relative to shadows produced by terrain detail such as ejecta fragments or small craters which are not resolved by the 2 kilometer averaging.



Distribution of slope lengths of a profile through upland area north of Ptolemaeus.

Figure 3.5-9

An approximate representation of surface brightness variations due to gross terrain features, surface character, and illumination has been derived as a "luminance profile" across an equatorial section of the moon. In order to simplify the study, apparent brightness of the surface at the nadir point only was considered. Where the local surface was very close to level, the value of α would be zero and would vary only as a result of surface slopes. Variations in α due to the angular field of view were not considered. Values for the albedo of the surface have been determined for only a limited number of localized areas (Reference 1 and 3). Because of this lack of data, it was necessary to assign values for various types of surface based upon measurements of presumably similar character. Obviously, such a procedure introduces an error into the representation, but it is probably within about 10%. Construction of the profile was based on the A.C.I.C. Lunar Atlas Charts covering the equatorial area from 50° East to 70° West Longitude. Beginning at 50° East, the horizontal distance was measured to positions along the equator where terrain features or surface character changes were believed to affect brightness. Where appreciable, slopes were computed from elevation changes indicated by chart contours. In the areas of upland-type terrain, where slope changes were very frequent and irregular and the elevation changes too small to be contoured, a slope variation of $\pm 3^\circ$ was assumed. In some cases, this slope variation was modified according to the representation on the charts.

During an orbital pass across the moon's nearside, rotation of the moon is not enough to change phase for the purpose of this study, thus the illumination angle could be considered as a function of lunar longitude. Three conditions of illumination were considered:

1. Full moon, with the subsolar point at 0° Latitude and 0° Longitude
2. First quarter, with the sub-solar point at 90° E Longitude and 0° Latitude, and the terminator along 0° Longitude
3. Last quarter, with the sub-solar point at 90° W Longitude, 0° Latitude and the terminator along 0° Longitude

With these phases the value of g at any point along the equator would be:

- Equal to East and West Longitude at Full Moon, with the value of α changing sign, for a given slope direction, at 0° Longitude

- 90° - East Longitude at First Quarter, where only the eastern half of the visible disk is lighted.
- 90° + West Longitude, at Last Quarter where only the western half of the visible disk is lighted

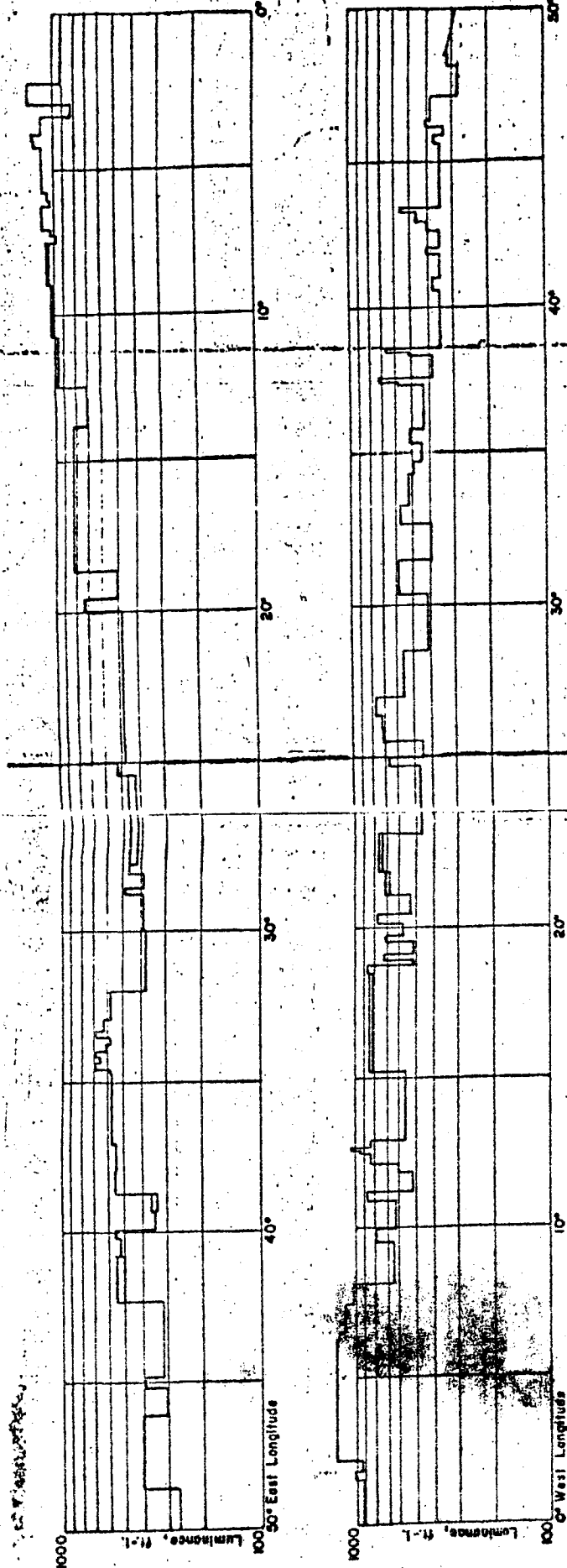
Since the mean length of the individual sections was about 14 kilometers, the mean Longitude of the section normally was used to determine the value of g . In the case of the few long sections over 100 kilometers, where the surface was more nearly uniform in character, as in the maria, a linear variation of g across the section was considered to be an adequate approximation. A direction of travel from east to west was assumed.

The albedo assigned to a given section was considered constant across its full length although it is recognized that variations undoubtedly exist and that in many cases an albedo change will occur as a more gradual blending rather than as sharply defined boundaries.

The value of the photometric function, ϕ , was determined for each section based on Fedoret's observations. The relative brightness of each section is the product of ϕ and the albedo, ρ . Using a solar constant of 1.31×10^4 foot candles, the surface luminance in foot-lamberts was computed for each section. These values were then plotted as luminance profiles for the three specified times of lunar phase, and are shown in Figures 3.3-10 and 3.3-11.

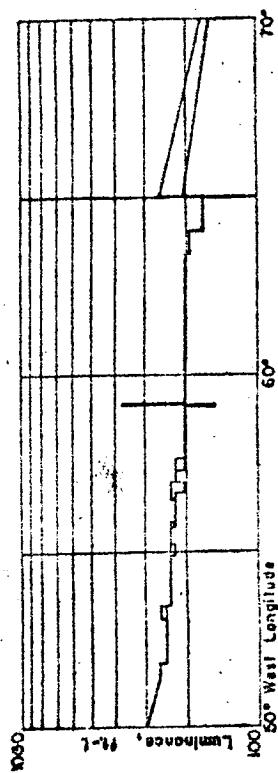
In Figure 3.3-10 where the profile extends from 50° E to 70° W under full moon illumination, the terminator is not crossed and no slopes sufficient to produce hard shadows were encountered on the gross topography. For this reason, at no point does the luminance drop to zero. On the two passes crossing the terminator, Figure 3.3-11, hard shadows exist, and because of terrain irregularities, the areas near the terminator show marked fluctuations between the highlight and shadows. In the sections of the profiles covering the L.O. illumination limits of 50° - 75° no shadows were encountered, although the general level of luminance changed by a factor of about 3 to 4.

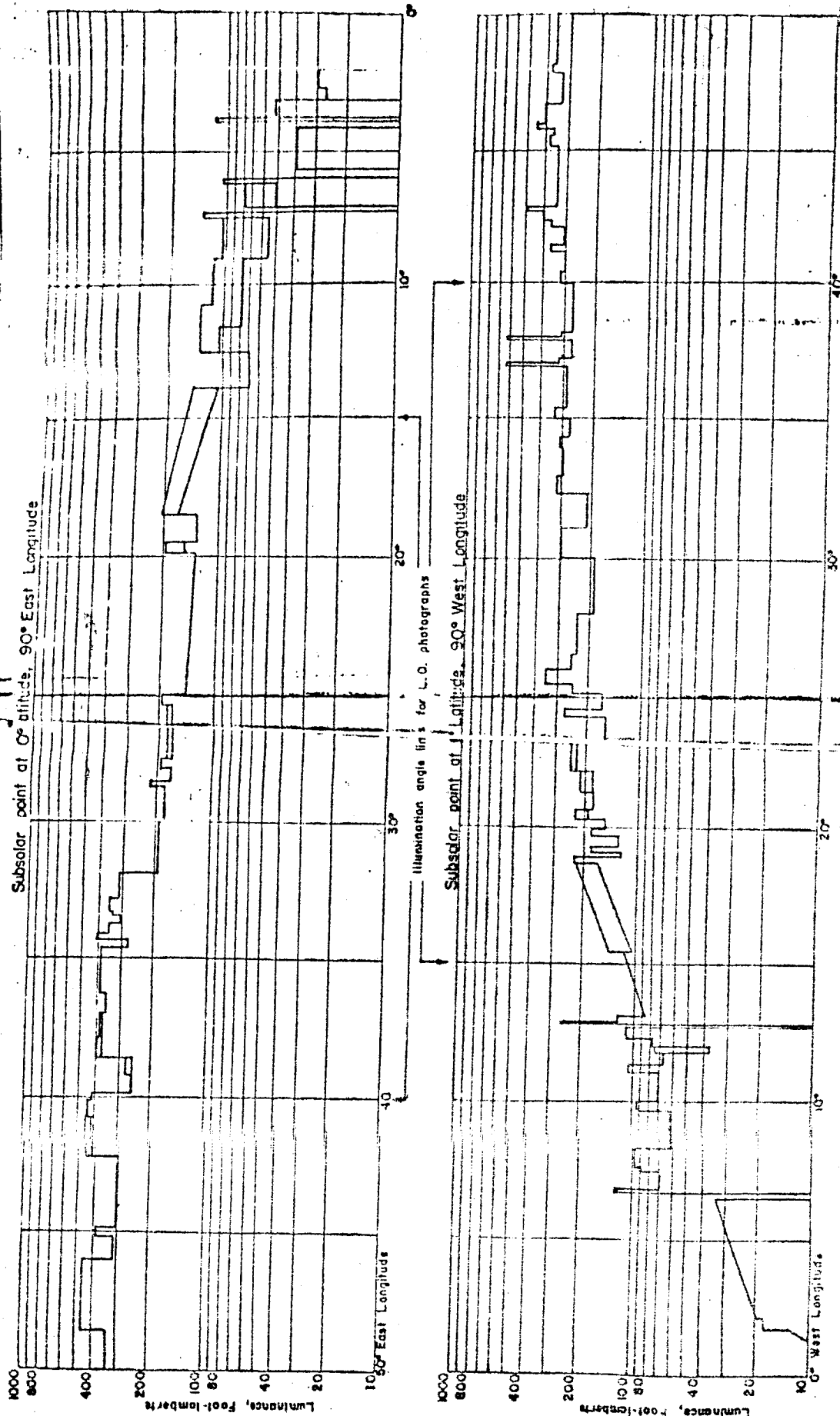
The luminance changes due to surface character occurred with variable frequency and amplitude. The frequency of change is a function of the size of feature, or in this study, the length of the section considered. A plot of the section length and cumulative percent of occurrence is shown in Figure 3.3-12. The time frequency may be obtained by dividing the section length by the orbital velocity of the L.O. It is seen that the mean length of section is 14 km and at an orbital velocity of 1.7 km/sec., the mean frequency of change is thus about 8.2 seconds.



Variation in luminance, in foot-lamberts, of the lunar surface along the equator between 50° East Longitude and 70° West Longitude, with the subsolar point at 0° Latitude, 0° Longitude.

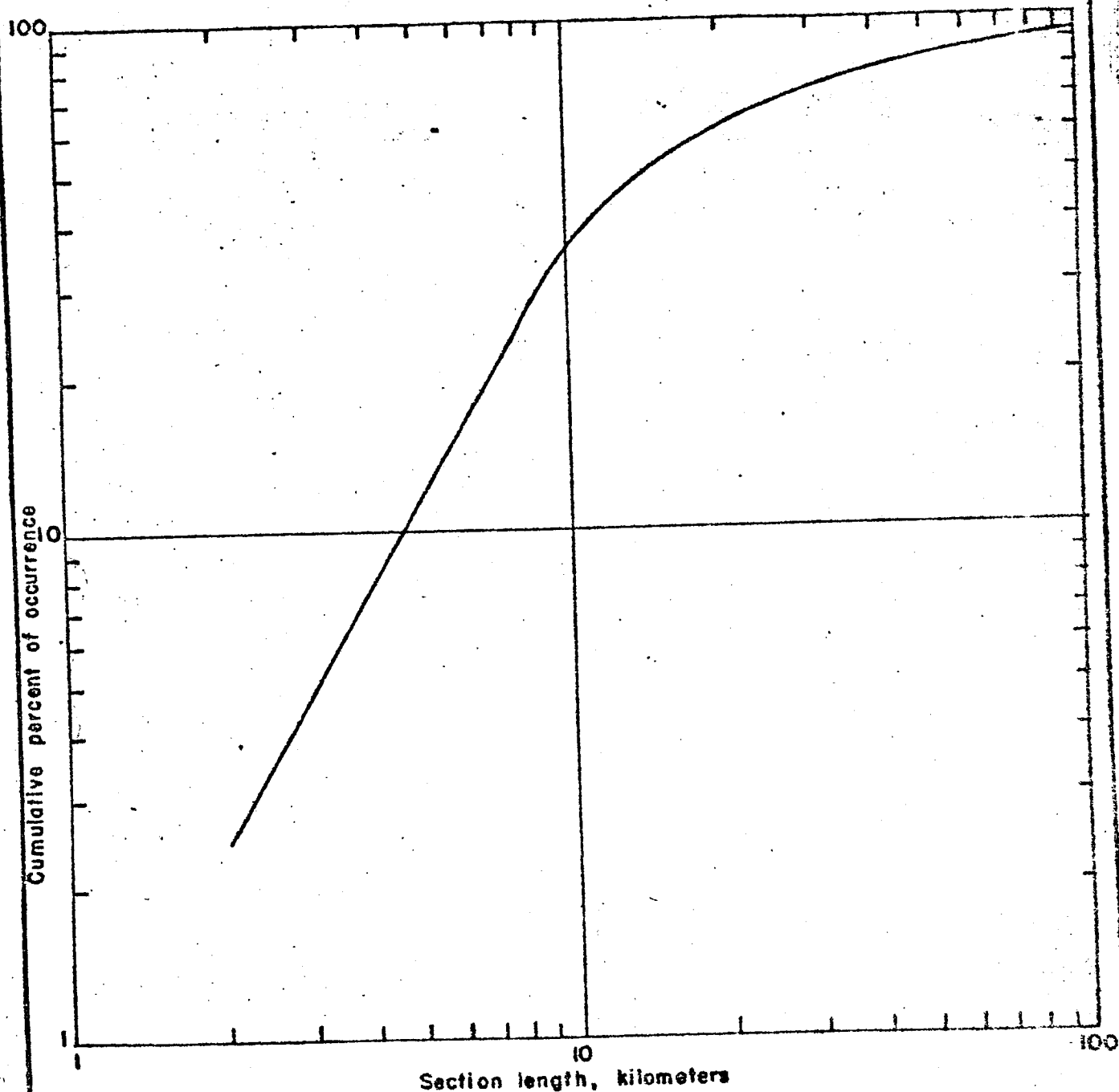
Figure 3.3-10





Variation in luminance, in foot-lamberts, of the lunar surface along the equator

Figure 3.3-11



Distribution of section lengths in luminance profiles.

Figure 3.3-12

U3 4288 2000 REV. 3/64

REV SYM _____

BOEING

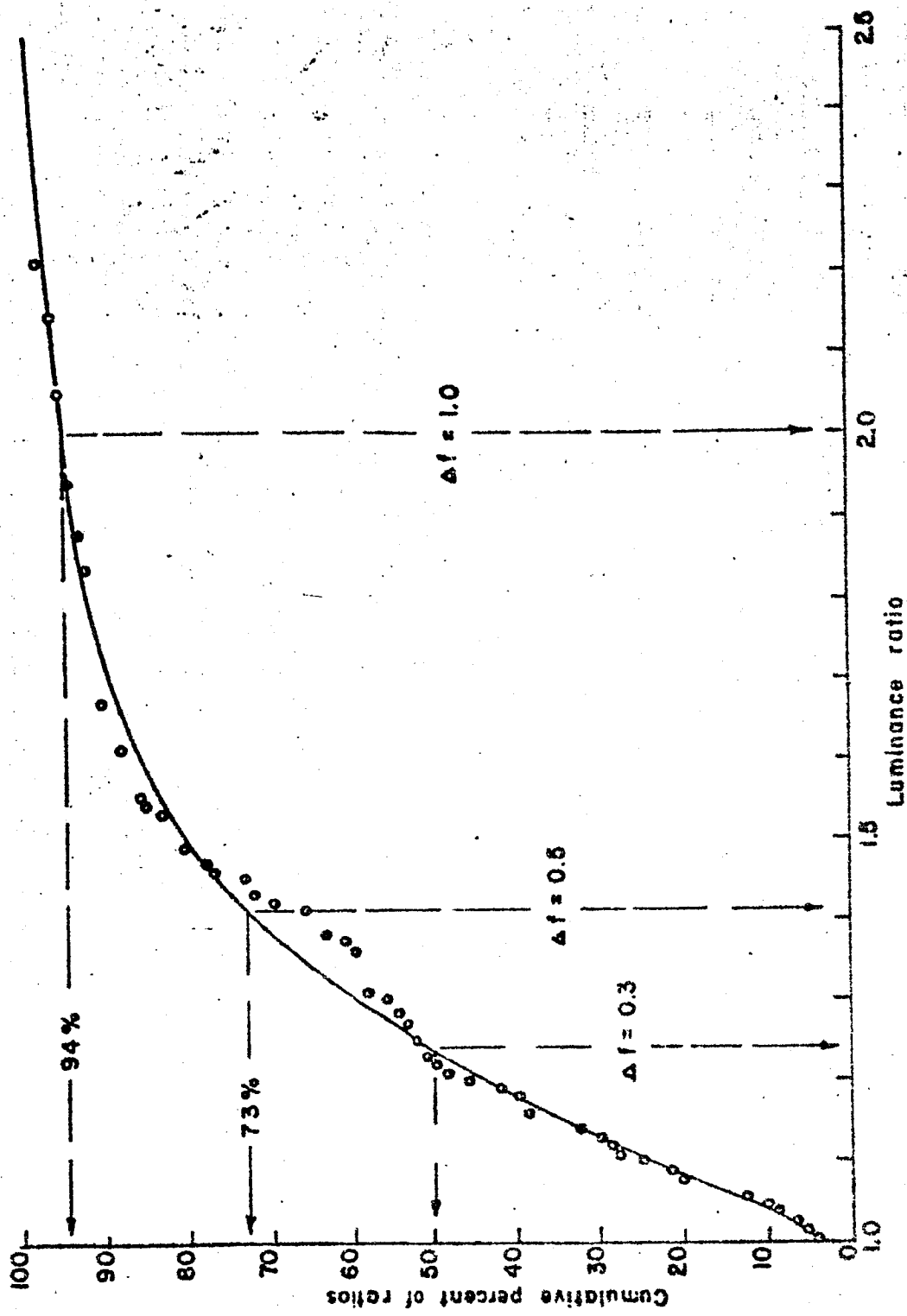
NO. D2-100293-2

PAGE

85

The magnitude of the luminance variations has been computed as the ratio of luminance values of a change. In Figure 3.3-13, the cumulative percent occurrence of change ratios limited to sun angles between 50° and 75° has been plotted.

Within the sun angle limitations imposed on the LO, luminance ratios up 1.4, equivalent to ± 0.5 photographic f. stop, will account for about 70% of the changes. Only about 10% of the changes appear to exceed ± 1 f. stop, or a ratio of 2.



Distribution of luminance ratio, or contrast ratios, between adjacent sections of luminance profile with sun angle between 50° and 75°. On camera axis at nadir.

Figure 3.3-13

U3 4284 2000 REV. 3/64

REV SYM _____

BOEING

NO. D2-100293-1

PAGE

87

References Section 3.0

1. Fessenkov, V. G., "Photometry of the Moon", in, "Physics and Astronomy of the Moon", Ed. Z. Kopal, Academic Press, 1962
2. Sytinskaya, N. N. and Scharonov, V. V., "An Investigation of the Reflecting Power of the Lunar Surface", Uch, Zapisky Univ. Leningrad, No. 153, 1952
3. Sytinskaya, N. N. "Svondnyy katalog absolyutnykh znacheniy vizual'noy otrazhatel'noy sposobnosti 10^4 lunnykh ob'yektov", Astronomicheskii Zhurnal 30:295 (1953)
4. Fedorets, V. A., "Photographic Photometry of the Lunar Surface" Kharkov State University, U.S.S.R., 1951
5. Wildey, Robert L. and Howard A. Phon, "Detailed Photoelectric Photometry of the Moon". Contribution No. 1254, Division of Geological Sciences, California Institute of Technology, Pasadena, California

4.0

Signal and Noise

Transfer of information which requires its conversion to some form of signal suitable for the subsystem involved, will result in degradation of that information; absolute equivalence of the signal to the original input rarely is possible. Limitations are imposed on the range and detail. Accuracy of equivalence may be variable, and spurious components, or noise, which obscures the signal at some level, may be introduced. Modulation transfer functions are used for evaluating degradation of information by the system components individually and in combination. The effects of lens and film combinations, exposure, image motion and conversion of the photographic image to an electrical signal in terms of resolution have been studied by this method.

Noise is introduced by film granularity and by the electrical components involved in scanning the photograph, transmitting, receiving, and reconstituting it. Analysis of noise contributions is necessary for the determination of the limitations on accuracy or resolution by consideration of the signal-to-noise ratio.

Transfer Functions

A starting point for a discussion of the Modulation Transfer Function (MTF), or the frequency response function as it is sometimes called, is with its relationship with the more common spread function. The lens will be used as the primary example for discussion, although the utility of the transfer function lies in the fact that it can be used to describe the net effect on the image as well as the individual contributions of lens, film, scanner elements, electronics, etc.

Any lens system, no matter how good, can not reproduce a point source as a point image. Rather, the image is spread over some finite area. The aberration-free lens system reproduces a point according to the diffraction limit as represented by the spread function of the common Airy Disc. This spread function, which is shown in Figure 4.1-1, shows the intensity distribution in the image plane resulting from a point source in the object plane. Fourier analysis tells us that a spread function is made up of a combination of sinusoidal functions of varying frequency and intensity. Taking the Fourier Transform of the Airy diffraction image gives us the frequency response curve or MTF as shown in Figure 4.1-2. The frequency (1/mm) cutoff point is a function of the relative aperture of the lens system and the wavelength. The MTF also varies as a function of the distance off-axis and as a function of focus position. The transfer function shown in the figure is for a diffraction limited $f/5.6$ lens on axis at 5500 Å. An actual lens system is not aberration free and thus the response is lower than that of the theoretical diffraction limited function. The MTF of the 24 inch focal length, $f/5.6$ LOS lens is shown for comparison in the dashed line in Figure 4.1-2.

The Fourier Transform of a point source target which produces the image plane spread function is a constant, i.e., it contains all frequencies at equal intensity. The lens (or other system element) does not perfectly reproduce all spacial frequencies (lines/mm). The low frequencies are well reproduced; the intermediate frequencies are reproduced with reduced signal modulation; and the high frequencies are not reproduced at all. The quantitative plot of the response of the particular lens or system element as a function of frequency is shown by its modulation transfer function (MTF).

The MTF for a total system is simply the product of the MTF's for each individual subsystem. The film, photomultiplier tube, and other elements of the system have finite minimum image spread functions and thus, MTF's. This permits a total signal frequency response analysis through the spacecraft payload, communications, and the optics and electronics of the ground reconstruction equipment.

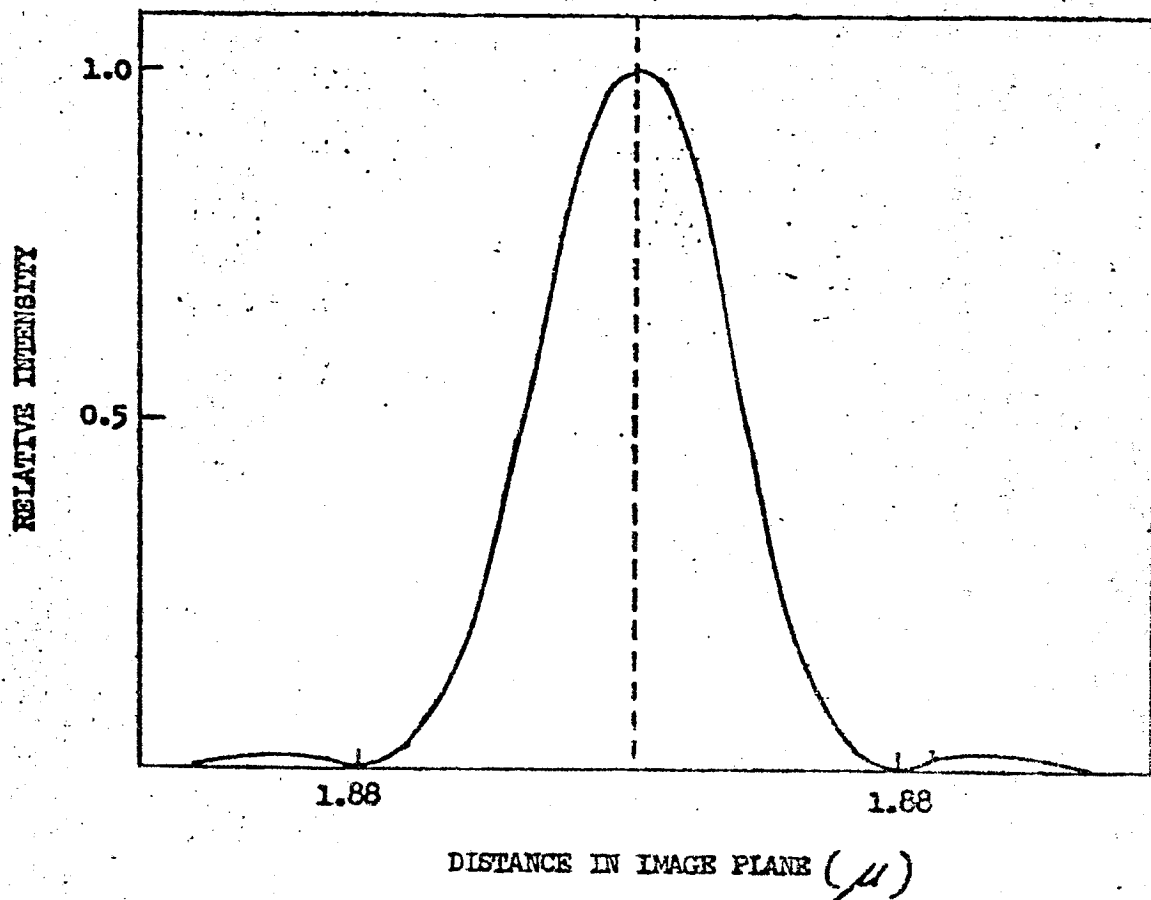


IMAGE SPREAD FUNCTION OF AIRY DISC FOR AN $f/5.6$ OPTICAL SYSTEM
AT 5500 Å

FIGURE 4.1-1

US 4288 2000 REV. 3/64

REV SYM _____

~~SECRET~~

NO.

D2-100293-1

PAGE

91

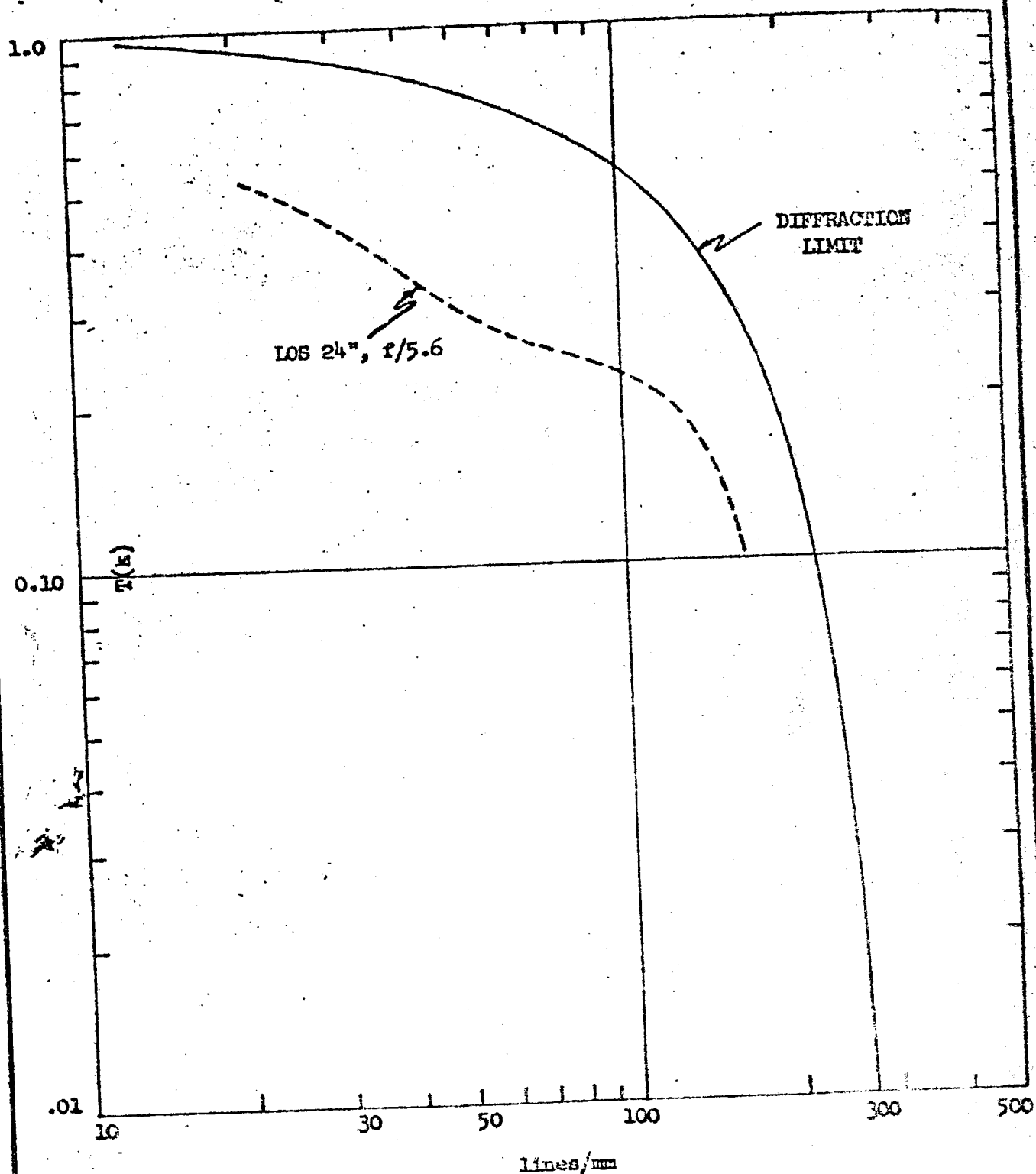


FIGURE 4.1-2 MODULATION TRANSFER FUNCTION (FOURIER TRANSFORM) OF DIFFRACTION LIMITED (AIRY SPREAD FUNCTION) f/5.6 OPTICS AT 5500 Å

U3 4288 2000 REV. 2/84

REV SYM _____

BOEING

NO.

D2-100293-1

PAGE

92

The MTF or frequency response is commonly measured with a sine wave test target. This is a pattern of bars and spaces with a sinusoidal variation in intensity which can be described by the equation: (see also Figure 4.1-3)

$$I_o(x_o) = A_o + B_o \cos w_o x_o$$

where,

$I_o(x_o)$ = target brightness as a function of x_o

A_o = average brightness = $\frac{I_{\max} + I_{\min}}{2}$

B_o = $\frac{I_{\max} - I_{\min}}{2}$

w_o = $2\pi N_o$, where N_o indicates lines/mm

x_o = distance in object plane perpendicular to target bars

The modulation, M_o = $\frac{B_o}{A_o}$ and

the contrast, C_o = $\frac{1 + M_o}{1 - M_o} = \frac{I_{\max}}{I_{\min}}$

Thus, a target scene with a contrast of 3/1 would have a modulation of 0.50.

In the relationships above, the subscript o denotes the object plane. The same formulas describe the relationships of these parameters as the object scene is reproduced in the image plane with the subscript i used to denote the image plane. Thus, the modulation in the image plane becomes

$M_i = \frac{B_i}{A_i}$, and the contrast $C_i = \frac{1 + M_i}{1 - M_i}$

The ability of the lens system to reproduce the contrast of the object plane in the image plane is shown quantitatively by the ratio of $\frac{M_i}{M_o}$ as a function of frequency, N_o , thus T(k) plot of $\frac{M_i}{M_o}$ as a function of frequency (lines/mm) is called the modulation transfer function (MTF) of the lens (or particular subsystem element, i.e.,

MTF = $\frac{M_i}{M_o}$ as a function of frequency

Experimentally, therefore, the MTF of a lens (or lens + film, etc.) can be determined by measuring the object modulation and resultant image modulation for a series of sine wave test targets of varying spatial frequencies or line spacings. As this modulation decreases as it is cascaded through the various system elements, a factor that becomes important is the minimum modulation on the film that is detectable by the eye. This is normally considered to be .04

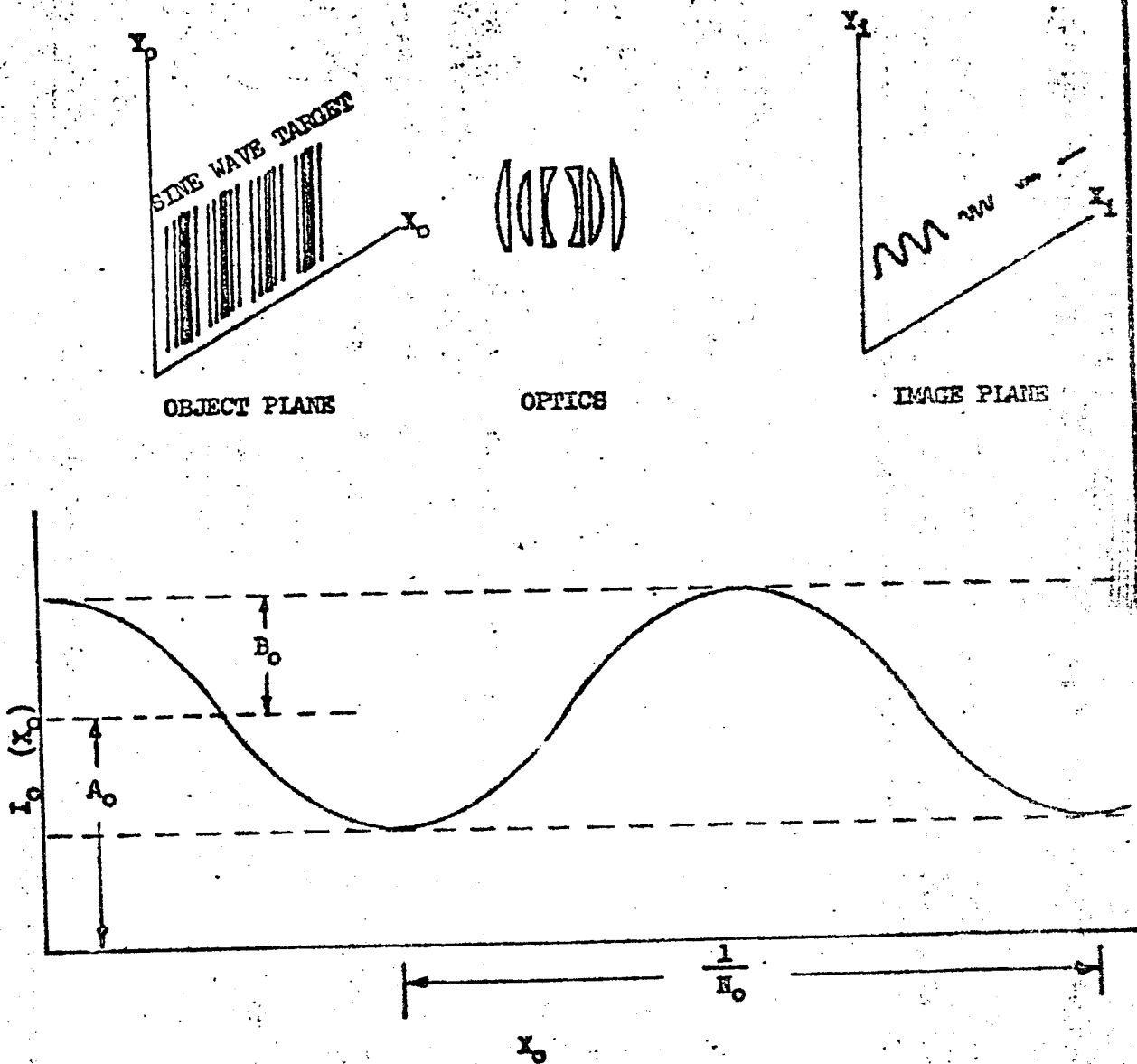


FIGURE 4.1-3 REPRESENTATION OF SINE WAVE RESPONSE MEASUREMENT

at lower frequencies. At higher frequencies, as the detail becomes finer, the grain of the photographic material begins to interfere with the ability of the observer to see the detail and thus the modulation of the image must be greater. This is shown quantitatively in Figure 4.1-4. With reference to the notations on the figure, the 50% modulation of the target scene is plotted as line (1); the MTF of the 24 inch lens is curve (2); the MTF of S.O. 243 film with bimat processing is line (3). Thus, by cascading these functions, the resultant signal modulation out of the processor is shown in curve (4). The threshold detection curve for S.O. 243 film is shown as curve (5). As indicated, the resolution of the system at the processor output is approximately 140 lines/mm. This signal would then be carried through the system elements of the scanner, communications link, and ground reconstruction equipment by adding the MTF's of these elements.

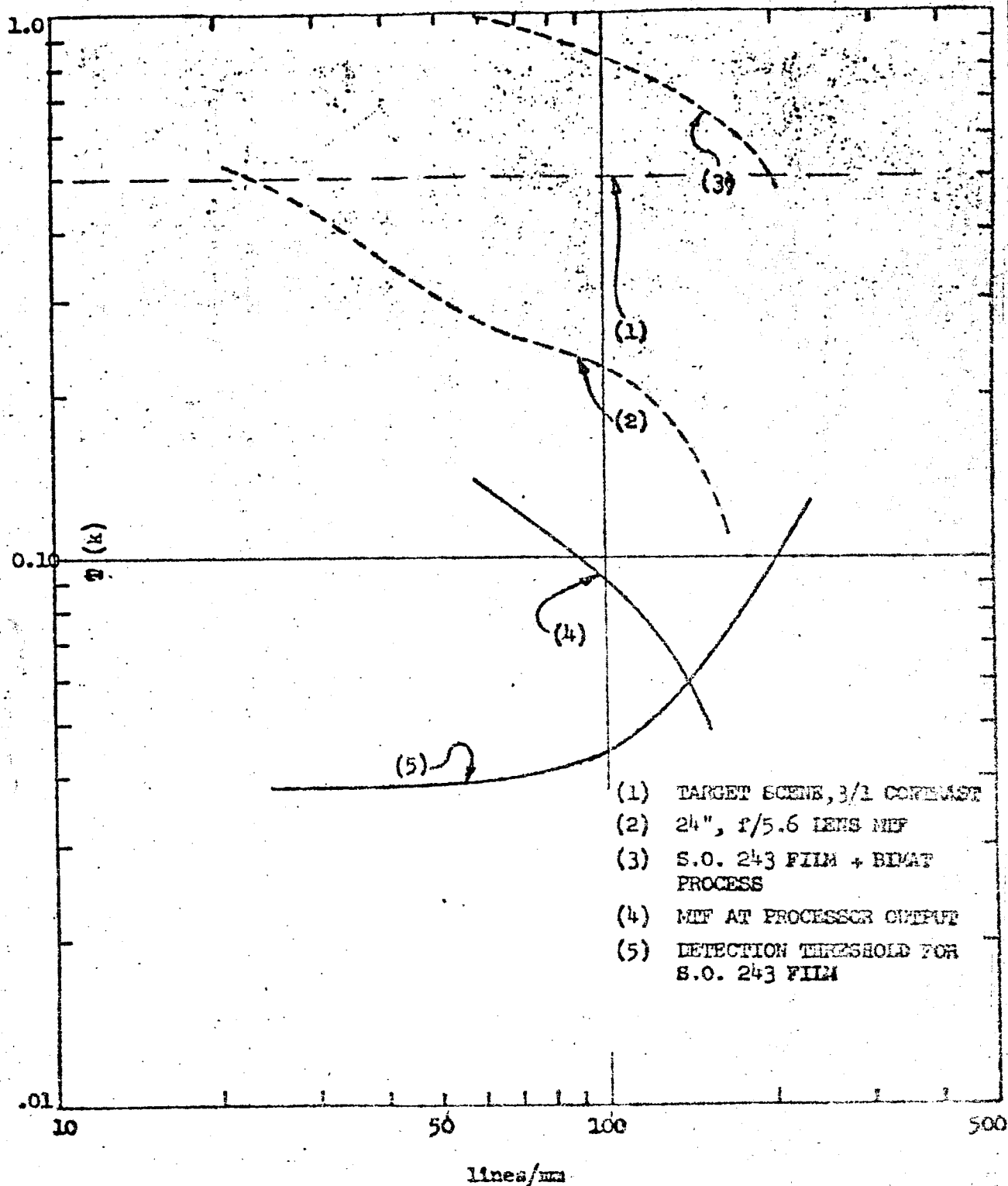


FIGURE 4.1-4 MODULATION TRANSFER ANALYSIS OF SIGNAL THROUGH PROCESECR AND MINIMUM MODULATION REQUIRED FOR DETECTION

U2 4288 2000 REV. 2/64

REV SYM _____

SECRET

NO. E2-100293 -1

PAGE

96

Scientific and technical uses of photography have resulted in a marked change in consideration of the photographic image. Rather than being considered in terms of the subjective values of a pictorial or an aesthetic nature, some applications place photography in a position closely allied to communications systems where many of the concepts of communications theory and information theory may be applied. In this context, a photograph is solely a means of recording and storing information. Examination of the photograph visually or by optical instruments to extract quantitative data constitutes the readout process. The amount of information stored by a photograph may vary from nearly zero to millions of bits per square inch. The capacity of film to store information is dependent upon a number of factors. Some of these are:

- . The characteristics of the image projected on the film.
- . The type of sensitive emulsion used.
- . The development process.
- . The readout method.

Each of these factors are, to some extent, interrelated. For example, variation in the development process can produce marked differences in the properties of the resulting image on a particular film emulsion. For any film there is an upper limit to storage capacity per unit area.

In the following discussion, the limitations imposed by the photography film, independent of the camera optics, are considered in the context of an information communications system. A major consideration is the system noise and the signal-to-noise ratio.

Everyone who has enlarged a small negative into a large photograph is immediately confronted by the problem that the photographic image is composed of small grains of silver. Image density, when small areas are considered, is not uniform. The visual impression is graininess, and the erratic spacing and intensity of density variations due to graininess is expressed as granularity. In terms of a communication system, granularity constitutes a noise.

Image density is determined by measuring the light transmission through a known film area commensurate with the image size of concern. The grains in an emulsion are distributed at random, and consequently, in a "uniform" image, give rise to random fluctuations even though the individual grains are not resolved. It becomes apparent that the size of the densitometer aperture affects the frequency and amplitude of the fluctuations since it results in an averaging of the density produced by the grains. The larger the aperture, the more closely the measurement approaches the average

image density, provided, of course, that the aperture size does not exceed the size of the image measured.

The concept of film noise is readily demonstrated. If a section of film, exposed uniformly and developed, is scanned rapidly by a microdensitometer and the output recorded as an electrical signal, the granularity produces fluctuations corresponding to the familiar white noise. Thus, where a density difference between an image and the background constitutes a signal, granularity, which is also a density variation, becomes noise. The conventional method of treating the problems of signal detection and signal to noise ratio of communication systems are to a large extent applicable to the problems of film noise. Film noise, and the film signal to noise ratio is of major concern in a photographic system where the maximum information content on the film is desired, the recording of image detail to resolution limits is required, and brightness differences between an object and its background is low.

It has been pointed out that the grain of a film emulsion is distributed randomly. Considering a uniformly exposed and processed film, granularity will follow a Poisson distribution with the magnitude being a function of the scanning aperture. Meaningful determination of an image, or signal, against its background must be in terms of some average. Where ΔD_i is the deviation of each of n density readings from the mean, the variance is defined as:

$$\sigma^2 = \frac{\sum \Delta D_i^2}{(n-1)}$$

and σ is the standard deviation or rms granularity. Selwin (1935) showed that granularity, defined by the equation

$$S = [\sigma(D)] [a^{\frac{1}{2}}]$$

where a is the densitometer aperture area, should be a constant. This relationship, now referred to as Selwin Granularity was confirmed by Higgins and Stultz (1959) where the average density is constant, but they show that for a particular film, S varies with the mean density. Since density is a factor in granularity, the relationship

$$\sigma = 0.07 (D - 0.15)^{.428}$$

has been established for SO 243 film scanned with an aperture of 5 μ .

The significance of film noise becomes apparent when considering images having a low contrast with the background. At any given point on the film, the density may vary from the nominal mean and may be sufficient to place it within the density level of either the object image or the background. The probability of such an error is related to σD such that 68% of all readings fall in the interval $\pm \sigma$. If an error of one part per thousand is permissible, the density levels must be separated by 3σ . For a very fine grain film (such as SO 243), σ is about 0.06 for a 5μ aperture, or 0.18 for 3σ . If the available density range of the film is 0.9 there would be about five separately distinguishable density levels or gray levels available for recording with 99.9% reliability.

The problem of film granularity takes on an added significance for the Lunar Orbiter Photo Subsystem. After exposure and processing, the film is scanned by a 5μ diameter spot of light moving across the image. The light that is transmitted through the film as a function of image density is received by a photomultiplier and converted into an electrical signal which is the input to the communications subsystem. In effect, the readout portion of the photo subsystem is a microdensitometer with an aperture diameter of 5μ . Film granularity which is resolvable by the scanner thus generates a noise component as part of the communication subsystem input.

Filter Characteristics

The detailed analysis and discussion of the effects of the communication system filters on the photographs has not been completed. This work will be included upon its completion.

4.4 Communications System

4.4.0 Introduction

The communication system accepts as input the composite video waveform from the airborne scanner. Both picture-information and noise components of the scanner output in the spacecraft are transmitted indiscriminantly to the receiving station on the Earth where they are supplied to the Ground Reconstruction Equipment (GRE) of the photosystem. Noise received by the ground antenna, as well as noise generated by the front-end of the receiving apparatus, cause the output of the communication system to differ from a true replica of the scanner output. This section describes the functional elements of the communications system, discusses the signal processing and noise generation and indicates the extent of the degradation of the GRE input with respect to the output of the airborne scanner.

4.4.1 System Description

4.4.1.1 Spacecraft

The functional elements of the picture transmission portion of the spacecraft communications system are indicated in Figure 4.4-1. The output of the scanner, assumed to be nominally in the frequency range between 0 and 230 kc, amplitudes - modulates a 310 kc subcarrier in a balanced modulator. The balanced modulator suppresses the subcarrier in the output, thus producing a double-sideband suppressed-carrier (DSB-SC) signal. The lower sideband of this signal extends from 80 kc to 310 kc, the upper sideband -- from 310 kc to 540 kc. The DSB-SC signal is then passed through a vestigial sideband filter which passes the lower end of the lower modulation sideband (80 kc to 230 kc), provides for a linear roll-off between the upper end of the lower sideband and lower end of the upper sideband (i.e., in the 230 kc to 390 kc region) and rejects the upper end of the upper sideband (i.e., frequencies greater than 390 kc). This vestigial sideband suppressed carrier (VSB-SC) signal is then passed through a high-pass filter which passes frequencies above 55 kc. By rejecting signals at frequencies below the nominal lower end of the lower sideband, this filter has the same effect as an input low-pass filter with a cutoff at 280 kc; it is included in the system to alleviate the input filtering requirements. The VSB-SC signal is then mixed with a 38.8 kc pilot tone and with a performance telemetry signal to derive the composite modulation baseband signal.

The pilot tone is a 48 submultiple of the subcarrier frequency, derived from the subcarrier oscillator. It is transmitted to provide a reference for the regeneration of the subcarrier signal required in the demodulation process.

The composite baseband signal phase modulates a 2295 Mc carrier in the transponder. The output of the transponder is amplified to a 10 watt level in a traveling wave tube (TWT) amplifier, and is then

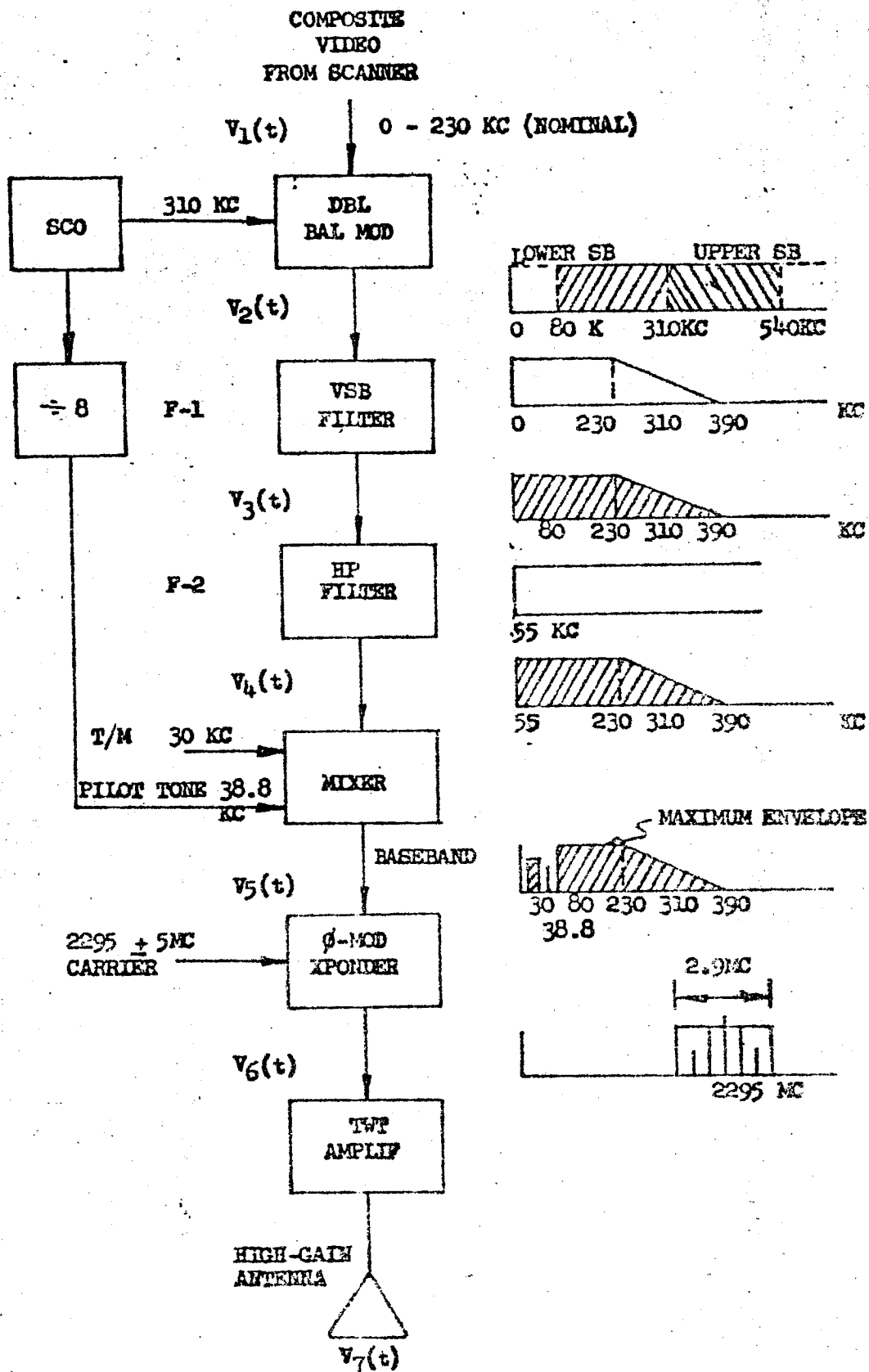


FIGURE 4.4-1

US 4298 2000 REV. 2/64

BLOCK DIAGRAM OF COMMUNICATIONS SYSTEM: SPACECRAFT

REV SYM _____

BOEING NO. 12-100293-1
PAGE 101

radiated by the high-gain antenna (3 foot parabolic dish) of the spacecraft.

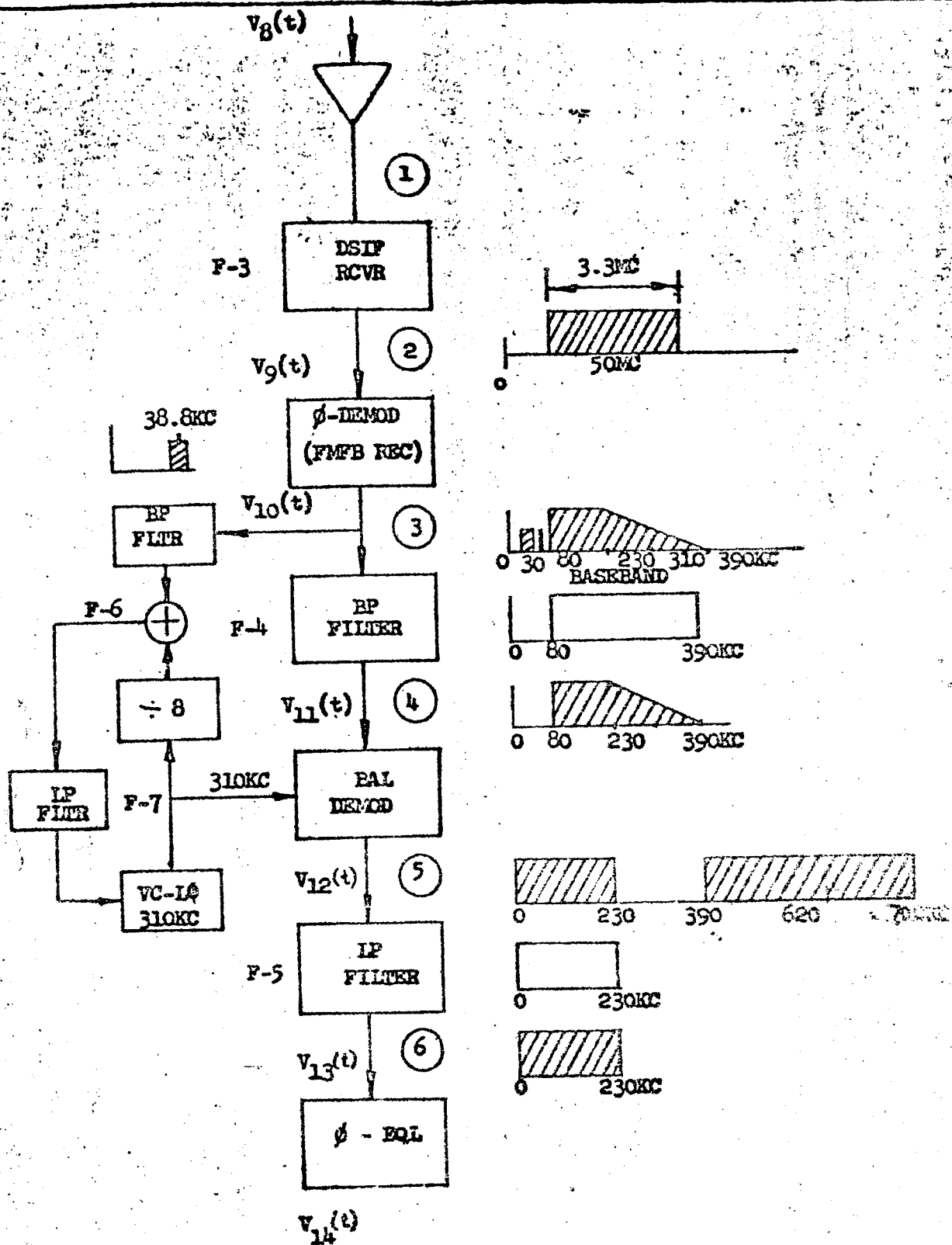
4.4.1.2 Earth Terminal

The receiving stations on Earth will utilize the DSIF antennas and receivers, together with the additional Lunar Orbiter program-peculiar equipment necessary for the recovery of the Modulating signal. The major functional components of the receiving system are indicated in Figure 4.4-2. The DSIF parabolic 85 ft. antenna receives the phase-modulated signal from the spacecraft. The signal is amplified in a maser pre-amplifier and is downtranslated to an intermediate carrier frequency of 50 mc in a 3.3 mc bandwidth. The 50 mc phase-modulated signal is detected in a frequency-feedback receiver, the output of which is the received version of the modulation baseband. A bandpass (80 kc to 390 kc) filter separates the VSB-SC picture signal, which is then applied to a balanced demodulator. The local subcarrier frequency injected into the balanced demodulator is coherent with the subcarrier frequency used in the modulator in the spacecraft. The coherency is achieved by phase locking the ± 8 frequency submultiple of a 310 kc local oscillator on the ground with the pilot tone recovered from the baseband. The output of the balanced demodulator contains two sidebands. The lower sideband extends from 0 to 230 kc and is the desired video signal. The upper sideband, extending from 390 kc to 790 kc is rejected in a low-pass filter following the balanced demodulator. The video signal is then passed through a phase equalizer, which network compensates for the group-delay variations incurred by the signal in the various filters of the system. The output of the phase equalizer constitutes the received composite video signal and is supplied to the ground reconstruction equipment (GRE).

4.4.2 Signal Processing

4.4.2.1 General

Signal processing by the communications system can be best indicated by following the transmission of a single-frequency sinusoidal signal through the functional elements of the system, starting at the input from the scanner and terminating at the output from the phase equalizer. Since at the present time the development of the actual hardware has not progressed to the point at which actual filter characteristics are available, idealized filter characteristics are assumed in the subsequent discussion. The discrepancy incurred by this approximation will be negligible with respect to signal and noise power calculations.



BLOCK DIAGRAM OF COMMUNICATIONS SYSTEM: CIRCLED

FIGURE 4.4-2

4.4.2.2 Signal Processing in the Spacecraft

For the purpose of analysis it is assumed that the input from the scanner is given by

$$V_1(t) = m \cos \omega_m t \quad (4.4-1)$$

The balanced modulator multiplies the input by $K_{12} \cos \omega_s t$, ω_s being the subcarrier angular frequency:

$$\begin{aligned} V_2(t) &= K_{12} m \cos \omega_m t \cos \omega_s t \\ &= \underbrace{K_2 \cos (\omega_s - \omega_m) t}_{\text{lower sideband}} + \underbrace{K_2 \cos (\omega_s + \omega_m) t}_{\text{upper sideband}} \end{aligned} \quad (4.4-2)$$

If the maximum modulating frequency is designated by ω_a , equation (4.4-2) shows that the spectrum of the output of the balanced modulator lies between $\omega_s - \omega_a$ and $\omega_s + \omega_a$. Numerically, ω_a corresponds to 230 kc, so that the preceding frequency limits correspond to 80 kc and 540 kc. The sideband filter F_1 in Figure 4.4-1 is characterized by its amplitude response $A_1(\omega)$ and its phase response $\phi_1(\omega)$. The idealized amplitude response is defined by

$$A_1(\omega) = \frac{1}{2} [1 + K(\omega)] \quad (4.4-3)$$

where

$$\begin{aligned} K(\omega) &= 1, & 0 < \omega < \omega_a \\ K(\omega) &= \frac{\omega_a}{\Delta\omega} (-\omega + \omega_s), & \omega_a \leq \omega \leq \omega_b \\ K(\omega) &= -1, & \omega_b < \omega \end{aligned}$$

and

ω_b - upper vestigial sideband frequency (390 kc)

$$\Delta\omega = \omega_s - \omega_a - \omega_b - \omega_s,$$

with

$$\Delta f = \frac{\Delta\omega}{2\pi} = 80 \text{ kc.}$$

The idealized phase response of the VSB filter is given by

$$\phi_1(\omega) = -T_f \omega \quad (4.4-4)$$

The filter response, characterized by equations (4.4-3) and (4.4-4) has the following properties:

$$\begin{aligned} K(\omega_s + \omega_m) &= -K(\omega_s - \omega_m) \\ -\phi(\omega_s) + \phi(\omega_s + \omega_m) &= -\phi(\omega_s - \omega_m) - \phi(\omega_s) \end{aligned} \quad (4.4-5)$$

The output of the vestigial sideband filter is hence given by

$$V_3(t) = \frac{1}{2} K_2 [1 + K(\omega_s - \omega_m)] \cos[(\omega_s - \omega_m)t + \phi(\omega_s - \omega_m)] + \frac{1}{2} K_2 [1 + K(\omega_s + \omega_m)] \cos[(\omega_s + \omega_m)t + \phi(\omega_s + \omega_m)] \quad (4.4-6)$$

setting

$$K(\omega_s - \omega_m) = K, \quad 0 \leq K \leq 1$$

$$\phi(\omega_s - \omega_m) = -\tau_1(\omega_s - \omega_m)$$

and

$$t' = t - \tau_1$$

and taking into account equations (4.4-5), equation (4.4-6) becomes

$$\begin{aligned} V_3(t) &= \frac{1}{2} K_2 [1 + K] \cos(\omega_s - \omega_m)t' + \frac{1}{2} K_2 [1 - K] \cos(\omega_s + \omega_m)t' \\ &= K_2 \sqrt{\cos^2 \omega_m t' + K^2 \sin^2 \omega_m t'} \cos[\omega_s t' - \tan^{-1}(K \tan \omega_m t')] \\ &= K_2 \sqrt{\frac{1}{2}(1 + K^2) + \frac{1}{2}(1 - K^2) \cos 2\omega_m t'} \cos[\omega_s t' - \tan^{-1}(K \tan \omega_m t')] \end{aligned} \quad (4.4-7)$$

The high pass filter F_2 has no effect on the signal shape as long as the signal lies in the nominal frequency range $0 < \omega_m < \omega_s$. The purpose of the filter F_2 is to help restrict the effective input video bandwidth to the nominal frequency range.

Hence,

$$V_4(t) = K_3 \sqrt{\frac{1}{2}(1 + K^2) + \frac{1}{2}(1 - K^2) \cos 2\omega_m t'} \cos[\omega_s t' - \tan^{-1}(K \tan \omega_m t')] \quad (4.4-8)$$

The maximum amplitude of the video portion of the baseband signal is hence given by the amplitude term in equation (4.4-8). This term has its maximum value K_3 when $\cos 2\omega_m t' = 1$. The minimum amplitude is similarly determined to be $K_3 K$. The instantaneous frequency ω_i of the modulating signal is given by

$$\begin{aligned} \omega_i &= \frac{d}{dt} [\omega_s t' - \tan^{-1}(K \tan \omega_m t')] \\ &= \omega_s - \frac{K \omega_m}{\cos^2 \omega_m t' + K^2 \sin^2 \omega_m t'} \\ &= \omega_s - \frac{2K \omega_m}{(1 + K^2) + (1 - K^2) \cos 2\omega_m t'} \end{aligned} \quad (4.4-9)$$

Maximum instantaneous frequency occurs when $\cos 2\omega_m t' = 1$

then

$$\omega_i = \omega_s - K \omega_m \quad (4.4-10)$$

Transmission of the baseband $V_5(t)$ through the RF portion of the system is likewise evaluated by considering the transmission of a single-frequency sinusoidal signal. Hence, it is assumed that the baseband signal is given by

$$V_5(t) = A_5 \cos \omega_m t \quad (4.4-11)$$

To allow for different amplitudes of the modulating signal, the following notation will be used

$$A_5 = \alpha A_{5p} \quad (4.4-12)$$

where $0 \leq \alpha \leq 1$ and $A_{5p} = \text{Max } A_5$

The phase-modulated output of the transponder is then

$$V_6(t) = A_6 \cos [\omega_c t + K_5 \alpha A_{5p} \cos \omega_m t] \quad (4.4-13)$$

The peak phase deviation Φ is given by

$$\Phi = K_5 A_{5p} \quad (4.4-14)$$

Hence, equation (4.4-13) can be restated as

$$\begin{aligned} V_6(t) &= A_6 \cos [\omega_c t + \alpha \Phi \cos \omega_m t] \\ &= A_6 \sum_{n=-\infty}^{+\infty} J_n(\alpha \Phi) \cos [(\omega_c + n \omega_m) t] \end{aligned} \quad (4.4-15)$$

The frequency band occupied by this signal can be estimated from the approximate FM bandwidth formula

$$\begin{aligned} BW &\approx 2(f_d + f_m) \\ &= 2(\beta f_m + f_m) \\ &= 2(\beta + 1) f_m \end{aligned} \quad (4.4-16)$$

The corresponding formula for phase modulation is obtained by replacing β with $\alpha \Phi$ in equation (4.4-16):

$$BW \approx 2(\alpha \Phi + 1) f_m \quad (4.4-17)$$

Allowing a deviation of 3.6 radians, the approximate RF bandwidth corresponding to a full-amplitude ($\alpha = 1$) modulating signal at the maximum frequency ω_5 (at $K = 0$ in equation 4.4-9) becomes

$$BW \approx (2)(3.6 + 1)(0.31) = 2.85 \text{ mc}$$

4.4.2.3 RF Link Performance

Between the output of the transponder and the input to the DSIF receiver the form of the signal remains essentially unchanged if the additive noise appearing at the input to the receiver (see Section 4.4.3) is neglected. The only change undergone by the signal in the RF transmission process is then an attenuation of the signal amplitude. With reference to equation (4.4-15), the signal input to the DSIF receiver is given by:

$$V_g(t) = A_g \cos[\omega_c t + \alpha \phi \cos \omega_m t] \quad (4.4-16)$$

The relationship between the signal amplitude at the output of the transponder (A_g) and the amplitude at the input to the DSIF receiver (A_r) is derived from an evaluation of the gains and losses of the RF link. Table 4.4-1 summarizes the parameters of the RF link:

R-F Link Parameters

| Parameter | Nominal Value | Worst Case Value |
|---------------------------------------|---------------|------------------|
| Transmitted Power (10 watts) | 40 dbm | 40 dbm |
| Transmitting Circuit Loss | - 0.4 db | - 0.5 db |
| Transmitting Antenna Gain | + 23.5 db | + 23.5 db |
| Transmitting Antenna Pointing Loss | - 2.0 db | - 3.0 db |
| Space Attenuation @ 2295 mc | -211.3 db | -211.8 db |
| Polarization Loss | - 0.1 db | - 0.2 db |
| Receiving Antenna Gain | + 53.0 db | + 52.5 db |
| Receiving Antenna Pointing Loss | 0.0 db | 0.0 db |
| Receiving Circuit Loss | - 0.2 db | - 0.4 db |
| System Performance Degradation Margin | - 3.0 db | - 3.0 db |
| Total Received Power | -100.5 dbm | -102.9 dbm |

TABLE 4.4-1

While most of the items in the preceding table are self-explanatory, the system performance degradation margin requires some clarification. Initial system requirements stipulated a 6 db safety margin in the link analysis to allow for tolerances in the link parameters. Recently, a requirement for a 3 db margin over the worst-case parameter values has been advocated. In order to compare both nominal and worst case performances on the same basis, a 3 db figure is used in the preceding tabulation.

The above link analysis establishes that in the nominal case, $\frac{1}{2} A_g^2 = 8.9 \times 10^{-14}$ watts \cong C NOM, in the worst case $\frac{1}{2} A_g^2 = 5.1 \times 10^{-14}$ watts \cong C MIN, where C represents the received RF signal power.

4.4.2.4 Signal Processing in the Receiving Equipment

Between antenna input terminals and the discriminator of the phase-modulation receiver, the form of the signal remains unchanged, except for a scaling factor K_9 . The multiplier K_9 signifies the gains in the DSIF preamplifier and receiver, and in the predetection portion of the PM receiver. Hence, at the input to the discriminator the signal is given by

$$\begin{aligned} V_9(t) &= K_9 V_8(t) \\ &= K_9 A_8 \cos [\omega_c t + \alpha \Phi \cos \omega_m t] \end{aligned} \quad (4.4-19)$$

Under normal operating conditions when the signal-to-noise ratio at the input to the discriminator is above a threshold value of 6db, the output of the PM receiver is given by

$$\begin{aligned} V_{10}(t) &= K_{10} \Phi \alpha \cos \omega_m t \\ &= K_{10} K_5 A_5 \cos \omega_m t \\ &= K_{10} K_5 V_5(t) \end{aligned} \quad (4.4-20)$$

The bandpass filter F-4 separates the video signal from the baseband. Hence, with reference to equation (4.4-8) the output of F-4 is given by

$$\begin{aligned} V_{11}(t) &= K_{11} K_{10} K_5 V_4(t) \\ &= K_{11} K_{10} K_5 A_4 \cos (\omega_s t - \varphi_4) \end{aligned} \quad (4.4-21)$$

where $A_4 = K_3 \sqrt{\frac{1}{2}(1+K^2) + \frac{1}{2}(1-K^2) \cos 2\omega_m t}$

and $\varphi_4 = \tan^{-1} [K \tan \omega_m t]$

Since $K_3 = \text{Max } A_4 \triangleq A_{4p}$, it follows from an analogy with equations 4.4-12, 4.4-14, that $K_5 K_3 = \Phi_v$, i.e., peak phase deviation corresponding to the video amplitude in the baseband, and

$$\alpha = \sqrt{\frac{1}{2}(1+K^2) + \frac{1}{2}(1-K^2) \cos 2\omega_m t}$$

Therefore, equation (4.4-21) can be rewritten as

$$\begin{aligned} V_{11}(t) &= K_{11} K_{10} \Phi_v \alpha \cos (\omega_s t - \varphi_4) \\ &= K_{11} K_{10} \Phi_v \sqrt{\frac{1}{2}(1+K^2) + \frac{1}{2}(1-K^2) \cos 2\omega_m t} \cos (\omega_s t - \varphi_4) \\ &= \frac{1}{2} K_{11} K_{10} \Phi_v [(1+K) \cos (\omega_s - \omega_m)t + (1-K) \cos (\omega_s + \omega_m)t] \end{aligned} \quad (4.4-22)$$

The balanced demodulator performs a multiplication of the received video signal with a locally reproduced subcarrier. Designating the local oscillator signal by $K_{12} \cos(\omega_s t + \psi)$, with ψ denoting the phase error of the reinserted subcarrier, the output of the balanced demodulator is

$$\begin{aligned} V_{12}(t) &= K_{12} \cos(\omega_s t + \psi) \cdot V_{11}(t) \\ &= \frac{1}{2} K_{12} K_{11} K_{10} \Phi_v \left[(\cos \psi \cos \omega_m t - K \sin \psi \sin \omega_m t) + \right. \\ &\quad \left. + \frac{1}{2} (1+K) \cos(2\omega_s t - \omega_m t + \psi) + \frac{1}{2} (1-K) \cos(2\omega_s t + \omega_m t + \psi) \right] \end{aligned} \quad (4.4-23)$$

The low-pass filter F-5 passes only the low-frequency components of $V_{12}(t)$, rejecting the sidebands about the second harmonic of the local oscillator frequency:

$$\begin{aligned} V_{13}(t) &= \frac{1}{2} \Phi_v K_{10} K_{11} K_{12} K_{13} (\cos \psi \cos \omega_m t - K \sin \psi \sin \omega_m t) \\ &= \frac{1}{2} \Phi_v K_R \sqrt{\cos^2 \psi + K^2 \sin^2 \psi} \cos[\omega_m t + \tan^{-1}(K \tan \psi)] \end{aligned} \quad (4.4-24)$$

where

$$K_R \triangleq K_{10} K_{11} K_{12} K_{13}$$

The effects of the subcarrier insertion phase error ψ are discussed in Section 4.4.4.3. Assuming ideal operation, with no subcarrier insertion phase error

$$V_{13}(t) = \frac{1}{2} \Phi_v K_R \cos \omega_m t \quad (4.4-25)$$

$V_{13}(t)$ is then passed through a phase equalizer. In the preceding analysis, whenever it was stated that a filter has no effect on the signal shape, it was assumed that the phase response of the filter has the form $\phi(\omega) = -T_0 \omega$. Since actual filters depart from this ideal phase characteristic, output phase equalization is necessary to obtain an end-to-end phase response of the ideal form.

The final output of the communications system is thus given by

$$V_{14}(t) = \frac{1}{2} \Phi_v K_R \cos \omega_m t \quad (4.4-26)$$

4.4.3 Noise Effects

4.4.3.1 Noise Sources

Noise in the communications system arises principally from two sources; (1) noise generated by the receiver and (2) thermal radiation from outside sources received by the receiving antenna. Both types of noise in the DSIF receiving system have been measured and the following noise temperatures have been obtained. With the antenna pointing at a "quiet" area of the sky, the system noise temperature has been found to be $55^\circ \pm 10^\circ \text{ K}$ (Reference 1). With the antenna boresight aligned with the center of a full moon, the system noise temperature has been found to increase by $110^\circ \pm 25^\circ \text{ K}$ (Reference 2). Therefore, a system noise temperature of 165° K will be assumed for the nominal case while 200° K will be used for the worst-case calculations.

4.4.3.2 Noise Processing

The noise appearing in the output of the communication system is calculated by finding the output of the receiving system when the transmitted signal consists of an unmodulated carrier.

The noise power density referred to the input of the DSIF receiver is given by

$$W_1(f) = K_B T_S \quad (4.4-27)$$

where T_S is the system noise temperature in degrees K, and $K_B = 1.37 \times 10^{-23}$ is the Boltzmann constant

At the phase modulation receiver (Point "2" in Figure 4.4-2), as a result of the bandlimiting introduced by the presellector filter of the DSIF receiver, the noise power density is given by

$$W_2(f) = K_9 W_1(f) \left[U(f - f_0 + \frac{B_{IF}}{2}) - U(f - f_0 - \frac{B_{IF}}{2}) \right] \quad (4.4-28)$$

where $U(f)$ - a unit step function

f_0 - intermediate frequency (50Mc)

B_{IF} - IF bandwidth (3.3 Mc)

K_9 - a constant (Cf. Section 4.4.2.4)

The noise power contained in each infinitesimal frequency interval of $W_2(f)$ can be assumed to be caused by a sinusoidal noise voltage $n(t)$:

$$n(t) = e_N \cos 2\pi f_c t \quad (4.4-29)$$

Invariance of power in the various representations of noise requires that

$$W_2(f) df = \frac{1}{2} e_N^2 \quad (4.4-30)$$

With an unmodulated carrier the total input to the phase demodulator is

$$V_g(t) = K_g A_g \cos \omega_c t + e_n \cos \omega_c t \quad (4.4-31)$$

setting $\omega_i = \omega_c + \omega'$

so that $-\pi B_{IF} \leq \omega' \leq \pi B_{IF}$

equation (4.4-31) becomes

$$\begin{aligned} V_g(t) &= (K_g A_g + e_n \cos \omega' t) \cos \omega_c t - e_n \sin \omega' t \sin \omega_c t \\ &= A_g(\omega') \cos [\omega_c t + \varphi_g(\omega')] \end{aligned} \quad (4.4-32)$$

where

$$A_g(\omega') = \sqrt{K_g^2 A_g^2 + e_n^2 + 2 K_g A_g e_n \cos \omega' t}$$

$$\varphi_g(\omega') = \tan^{-1} \left[\frac{e_n \sin \omega' t}{K_g A_g + e_n \cos \omega' t} \right]$$

The output of the phase detector is given by

$$n_{10}(t) = K_{10} \varphi_g(\omega') = K_{10} \tan^{-1} \left[\frac{e_n \sin \omega' t}{K_g A_g + e_n \cos \omega' t} \right] \quad (4.4-33)$$

Since $e_n \ll K_g A_g$ for all carrier-to-noise power ratios greater than 1, the following approximations hold:

$$n_{10}(t) \approx K_{10} \tan^{-1} \left(\frac{e_n}{K_g A_g} \sin \omega' t \right) \approx K_{10} \frac{e_n}{K_g A_g} \sin \omega' t \quad (4.4-34)$$

The noise power corresponding to the noise voltage $n_{10}(t)$ is

$$\begin{aligned} W_3(f) df &= K_{10}^2 (2) \left(\frac{1}{2} \right) \left(\frac{e_n}{K_g A_g} \right)^2 [u(f) - u(f - \frac{B_{IF}}{2})] \\ &= K_{10}^2 \frac{e_n^2}{K_g^2 A_g^2} [u(f) - u(f - \frac{B_{IF}}{2})] \end{aligned} \quad (4.4-35)$$

where $W_3(f)$ is the noise power density at the point "3" in Figure 4.4-2 (The factor 2 in the derivation of equation (4.4-35) is required to account for both positive and negative frequencies represented by ω').

From equations (4.4-30), (4.4-28) and (4.4-27), it is found that

$$e_N^2 = 2W_2(f)df = 2K_9^2 K_B T_S df \quad (4.4-35)$$

so that

$$W_3(f) = K_{10}^2 \frac{K_B T_S}{C} \left[u(f) - u\left(f - \frac{\omega_{IF}}{2}\right) \right] \quad (4.4-37)$$

At the output of the bandpass filter F-4 (point "4" in Figure 4.4-2) the noise power density is given by

$$W_4(f) = K_{11}^2 K_{10}^2 \frac{K_B T_S}{C} \left[u(f-f_a) - u(f-f_b) \right] \quad (4.4-38)$$

where

$$f_a = 80 \text{ KC}$$

$$f_b = 390 \text{ KC}$$

The output of the balanced demodulator is given by

$$\begin{aligned} \eta_{12}(t) &= K_{10} K_{11} \frac{e_N}{K_9 A_8} \sin \omega' t \times K_{12} \cos \omega_s t \\ &= K_{10} K_{11} K_{12} \left(\frac{e_N}{K_9 A_8} \right) \left[\underbrace{\frac{1}{2} \sin(\omega' + \omega_s) t}_{\text{upper sideband}} + \underbrace{\frac{1}{2} \sin(\omega' - \omega_s) t}_{\text{lower sideband}} \right] \end{aligned} \quad (4.4-39)$$

Since ω' has both positive and negative values, equation (4.4-39) can be rewritten

$$\begin{aligned} \eta_{12}(t) &= K_{10} K_{11} K_{12} \left(\frac{e_N}{K_9 A_8} \right) \frac{1}{2} \left[\underbrace{\sin(\omega' + \omega_s) t + \sin(-\omega' + \omega_s) t}_{\text{upper sideband}} \right. \\ &\quad \left. + \underbrace{\sin(\omega' - \omega_s) t + \sin(-\omega' - \omega_s) t}_{\text{lower sideband}} \right] \end{aligned} \quad (4.4-40)$$

In equation (4.4-40) ω' has positive values only. However, linear addition of terms containing ω' and $-\omega'$ is not permissible, since the corresponding noise voltages are incoherent. Because of the bandlimiting action of the bandpass filter F-4, the domain of $\eta_{12}(t)$ is restricted to $\omega_a \leq \omega' \leq \omega_b$. Hence, the upper sideband of the balanced demodulator will contain frequencies $(\omega_a + \omega_s) \leq \omega \leq (\omega_b + \omega_s)$ and $(-\omega_b + \omega_s) \leq \omega \leq (-\omega_a + \omega_s)$, while the lower sideband will contain $(\omega_a - \omega_s) \leq \omega \leq (\omega_b - \omega_s)$ and $(-\omega_b - \omega_s) \leq \omega \leq (-\omega_a - \omega_s)$.

Numerically, the above frequency ranges correspond to upper sideband: -80 KC to 230 KC, 390 KC to 700 KC - lower sideband: -230 KC to 80KC -700KC to -390 KC. The double sided power density spectrum of $W_S(f)$ is hence given by

$$W_S(f) = \frac{1}{8} K_{10}^2 K_{11}^2 K_{12}^2 \frac{K_B T_s}{C} [u(f+f_s+f_b) - u(f+f_s+f_a) + u(f+f_s-f_a) - u(f+f_s-f_b) + u(f-f_s+f_b) - u(f-f_s+f_a) - u(f-f_s-f_a) + u(f-f_s-f_b)] \quad (4.4-41)$$

In terms of a one-sided power density spectrum

$$W_S(f) = \frac{1}{4} K_{10}^2 K_{11}^2 K_{12}^2 \frac{K_B T_s}{C} [2u(f) - u(f+f_s-f_b) - u(f-f_s+f_a) + u(f-f_s-f_a) - u(f-f_s-f_b)] \quad (4.4-42)$$

At the output of the low-pass filter the power density spectrum becomes

$$W_G(f) = \frac{1}{4} K_R^2 \frac{K_B T_s}{C} [2u(f) - u(f+f_s-f_b) - u(f-f_s+f_a)] \quad (4.4-43)$$

The final output noise power density spectrum is likewise given by equation (4.4-43) since the phase equalizer has no effect on the power spectrum. Figure 4.4-3 shows the output noise power density spectrum.

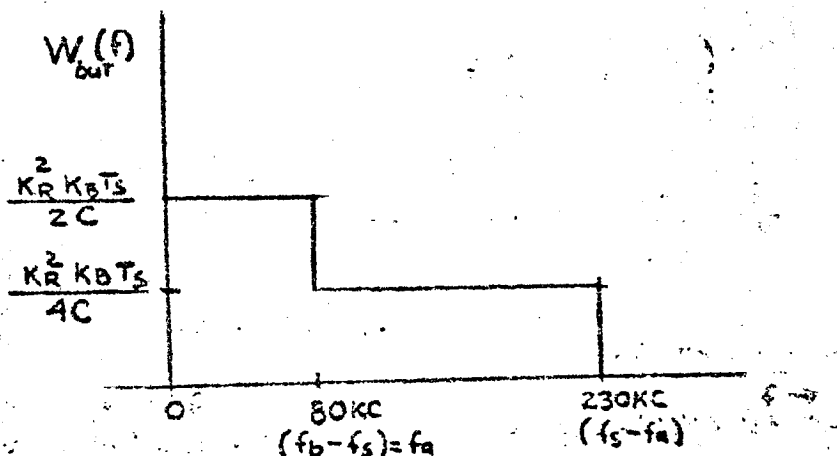


FIGURE 4.4-3

4.4.4 System Performance

4.4.4.1 Video Signal-to-Noise Ratio

Video signal-to-noise ratio is obtained by calculating the output signal power from equation (4.4-26) and by determining the output noise power from equation (4.4-43)

$$\text{Thus, } S_{\text{out}} = \frac{1}{8} \Phi_v^2 K_R^2 \quad (4.4-44)$$

while

$$N_{\text{out}} = \int_0^{f_s - f_a} W_{\text{out}}(f) df = \frac{K_R^2 K_B T_S}{4C} \left[\int_0^{f_a} 2 df + \int_{f_a}^{f_s - f_a} df \right] \\ = \frac{K_R^2 K_B T_S f_s}{4C} \quad (4.4-45)$$

Hence, the video RMS signal to RMS noise power ratio is given by

$$\left(\frac{S}{N} \right)_{\text{out}} = \frac{\Phi_v^2 C}{2 K_B T_S f_s} \quad (4.4-46)$$

The following parameter values apply:

$$\Phi_v = 3.6 \text{ radians}$$

$$K_B = 1.37 \times 10^{-23}$$

$$T_S = 165^\circ \text{ K (nominal)} \quad T_S = 200^\circ \text{ K (worst case)}$$

$$C = 8.9 \times 10^{-14} \text{ watts (nominal)} \quad C = 5.1 \times 10^{-14} \text{ watts (worst-case)}$$

$$f_s = 310 \text{ KC}$$

Therefore,

$$(S/N)_{\text{out}} = 29.1 \text{ db in the nominal case}$$

$$(S/N)_{\text{out}} = 25.9 \text{ db in the worst case}$$

For sinusoidal input signals the above RMS/RMS signal-to-noise ratios can be converted into peak-peak/RMS signal-to-noise ratios by adding 9db to the above values.

4.4.4.2 Relative Output Noise Power Density

The noise power density described by equation (4.4-42) and shown in Figure 4.4-3 involves an unknown factor K_R^2 . Since the same factor appears in the expression for the output signal power (4.4-26), the noise power density can be expressed in terms of output power (assuming full-amplitude video signal):

$$W_{\text{out}}(f) = \frac{2 S_{\text{out}}}{\Phi_v^2} \frac{K_B T_S}{C} [2u(f) - u(f + f_s - f_a) - u(f - f_a + f_a)] \quad (4.4-47)$$

With the parameter values used in Section 4.4.4.1 and assuming an output signal power S out of 1 watt, the relative output noise spectral density (in watts per cycle per watts output signal) is given in Table 4.4-2.

| FREQUENCY INTERVAL | RELATIVE OUTPUT NOISE POWER DENSITY | |
|--------------------|-------------------------------------|-----------------------|
| | NOMINAL | WORST-CASE |
| 0 - 80 KC | 7.82×10^{-9} | 16.5×10^{-9} |
| 80 KC - 230 KC | 3.91×10^{-9} | 8.3×10^{-9} |

TABLE 4.4-2

4.4.4.3 Margin at the Demodulator Threshold

The signal power at the input to the phase demodulator is obtained from equation (4.4-19):

$$P_2 = \frac{1}{2} K_g^2 A_g^2 = K_g^2 C$$

Noise power density at the same point is given by equation (4.4-20). Hence, the noise power is

$$N_2 = \int_0^\infty W_2(f) df = \int_{f_0 - \frac{1}{2} B_{IF}}^{f_0 + \frac{1}{2} B_{IF}} K_g^2 K_B T_s df = K_g^2 K_B T_s B_{IF}$$

The signal-to-noise ratio is hence

$$\left(\frac{C}{N}\right) = \frac{K_g^2 C}{K_g^2 T_s K_B B_{IF}} = \frac{C}{K_B T_s B_{IF}}$$

With $B_{IF} = 3.3$ mc, in the nominal case

$$(C/N) = -100.5 \text{ dbm} + 111.2 \text{ dbm} = 10.7 \text{ db}$$

Similarly, in the worst-case

$$(C/N) = -102.9 \text{ dbm} + 110.4 \text{ dbm} = 7.5 \text{ db}$$

Assuming a phase demodulator (FMFB) threshold of 7db, it is seen that, together with the 3db performance margin allowed for the system degradation, the signal margin at the demodulator is

$$10.7 - 7 + 3 = 6.7 \text{ db in the nominal case}$$

$$7.5 - 7 + 3 = 3.5 \text{ db in the worst case}$$

4.4.4.4 Effect of Subcarrier Insertion Phase Error

As was shown in Section 4.4.2.3 (equation 4.4-24) subcarrier insertion phase error ψ causes an amplitude distortion factor $a(\psi)$

$$a(\psi) = \sqrt{\cos^2 \psi + K^2 \sin^2 \psi}$$

and a phase distortion term

$$\varphi(\psi) = \tan^{-1}(K \tan \psi)$$

Maximum amplitude distortion occurs where $K = 0$, i.e., when the signal frequency is near 0 cps

$$\text{Max } a(\psi) = \cos \psi$$

Maximum phase distortion occurs when $K = 1$, i.e., for signal frequencies between 80 KC and 230 KC. Then

$$\varphi(\psi) = \psi$$

In the design of the communications system maximum allowable subcarrier insertion phase error (3- σ value) is 19.2°. Hence 99.87% of time the maximum amplitude distortion will not exceed

$$20 \log(\cos 19.2^\circ) = -0.5 \text{ db}$$

Maximum delay variation will not exceed

$$\begin{aligned} \delta \tau &= \psi \left(\frac{1}{\omega_1} - \frac{1}{\omega_2} \right) = \frac{19.6}{360} \left[\frac{1}{80} - \frac{1}{230} \right] 10^{-3} \\ &= 0.44 \text{ micro-seconds} \end{aligned}$$

Section 4.4 References

- 1) JPL Technical Memorandum No. 33-83 (Revision 1)
"System Capabilities and Development Schedule of the
DSIF 1964-68"
- 2) Boeing Memorandum 2-1533-53-009 dated May 26, 1964,
"Trip Report for JPL/NASA/Boeing Meeting at Pasadena,
California 18-19 May 1964"

In order to realize the high resolution performance designed into the LOS photographic system, it becomes essential to minimize relative motion between the optical image and the film during exposure. The effect of this motion, of course, would be to produce a blur or smear in the film imagery.

It has been shown by Scott⁽¹⁾ that motion of the image with respect to the film which is directional and continuous during exposure can be represented by a modulation transfer function of the form

$$T(k) = \frac{\sin X}{X}$$

The motions to be analyzed for this system can be considered in terms of image motion along the direction of flight and those components in a perpendicular direction, sometimes designated as cross image motion. The major source of image motion, of course, is that along the direction of flight due to the forward motion of the vehicle in orbit.

The relative velocity of the image in radians/sec. is measured by a V/H sensor. The sensor provides this signal to the image motion compensation (IMC) drive unit which moves the film at the correct rate during exposure to minimize image smear. A realistic error considered for the V/H sensor and IMC drive in performing their functions is taken to be 0.5%, 3σ, for each of these components.

Additional factors which contribute to the image smear are associated with the attitude control system. A portion of the smear budget must be allocated to these contributions. The random attitude pointing errors, 3σ, are set at 0.5 degree for yaw and roll, and 2 degrees for pitch, while the attitude rate is taken as 36 arc-seconds/sec, 3σ.

A chart of the designated smear budget in terms of error specifications and image smear on spacecraft film/exposure time is shown in Figure 5.0-1. This data is for a V/H rate associated with 46 km and a 24 inch focal length optical system. Data is included in the chart to permit the calculation of the smear effect under worst case conditions. This worst case would include utilizing the maximum exposure time of 1/25 second, 3σ error values, and the smear at the edge of the format in terms of pointing errors.

A group of additional factors, which must be considered in the smear analysis but contribute individually to a lesser extent are lumped into one entry. These include vibration, scan linearity in spacecraft and ground reconstruction equipment, jitter tolerance, et

(1) Scott, R.M., Photographic Science & Engineering, Vol. 3 No5, 1959

Image Plane of 24" lens

V/H = .04164 (46 Km perilune, 1850 Km Apolune)

| Contributor | 30° Error | Smear Along Flight | Smear Perpendicular to Flight |
|--|--|--|---|
| V/H Sensor | 0.5% | 127 microns/sec. | - |
| IMC Drive | 0.5% | 127 | - |
| Roll Rate | 36 sec/sec | - | 107 microns/sec |
| Pitch Rate | 36 sec/sec | 107 | - |
| Yaw Attitude | 0.5° | - | 222 |
| Roll Attitude | 0.5° at edge of 10° half angle | - | 36 |
| Pitch Attitude | 2.0° at edge of 2.5° half angle | 52 | - |
| Additional Factors (vibration, jitter scan linearity, etc.) | | 200 | 200 |
| RSS (30°) | | 294 microns/sec | 320 microns/sec |
| Lunar Surface curvature | 1 1/2° pitch error at each end of 20 frame burst | 38 microns/sec | - |
| Worst Case Total | | 332 microns/sec at edge of 2 1/2° half angle | 320 microns/sec at edge of 10° half angle |
| Worst Case smear (30° errors, edge of field, 1/25 sec. exposure) | | 13.28 microns | 12.8 microns |
| Worst Case "Predicted" Resolution | | 1.6 meters (2 1/2°) | 1.7 meters (10°) |
| Nominal Case Smear (10° errors, on axis, 1/50 sec. exposure) * | | 1.95 microns | 2.14 microns |
| Nominal Case "Predicted" Resolution | | 1.0 meter (on axis) | 1.0 meter (on axis) 1.3 meter (20° off axis) |

*See text

Figure 5.0-1 SMEAR BUDGET

In order to give an indication of the effect on resolution at the edge of the format for the worst case smear conditions, a predicted system resolution was obtained by inserting the modulation transfer functions for these smear values and for the lens off-axis. However, it should be emphasized that the off-axis performance of the lens has not been measured and this curve is only postulated. The resultant "predicted" resolution then becomes only an indication of the expected value.

The Root-Sum-Square of the total smear budget calculates out to be 320 microns/second, 3σ , for the limiting direction which is perpendicular to the line of flight. For purposes of nominal condition signal analysis, a 1σ value of 107 microns/sec. is used.

The other parameter of importance for the smear analysis is the exposure time of the camera. The nominal exposure time is 1/50 second which corresponds to a scene brightness of approximately 200-400 ft.-lamberts*. Thus, the nominal smear considered in the image during exposure is the product of the 1/50 second exposure and the 1σ smear rate of 107 microns/second or an image spread due to smear of 2.14 microns. The transfer function for this image spread is plotted in Figure 5.0-2. It can be seen that, in the frequency region of interest (76 1/mm) for the total system output, the modulation response for the nominal case is 0.96. This would result in decreasing the final resolution by 2 lines/mm which is insignificant in terms of other transfer functions and the accuracy which can be associated with the various data.

In terms of the worst case conditions associated with 3σ smear errors and 1/25 second exposure time, the MTF for the perpendicular smear of 12.8 microns which would be seen at the edge of the 10° half angle field of view is plotted as the dashed line in Figure 5.0.2. This smear would limit resolution to approximately 45 lines/mm.

*See Figure 3.3-11 for estimated scene luminance profile.

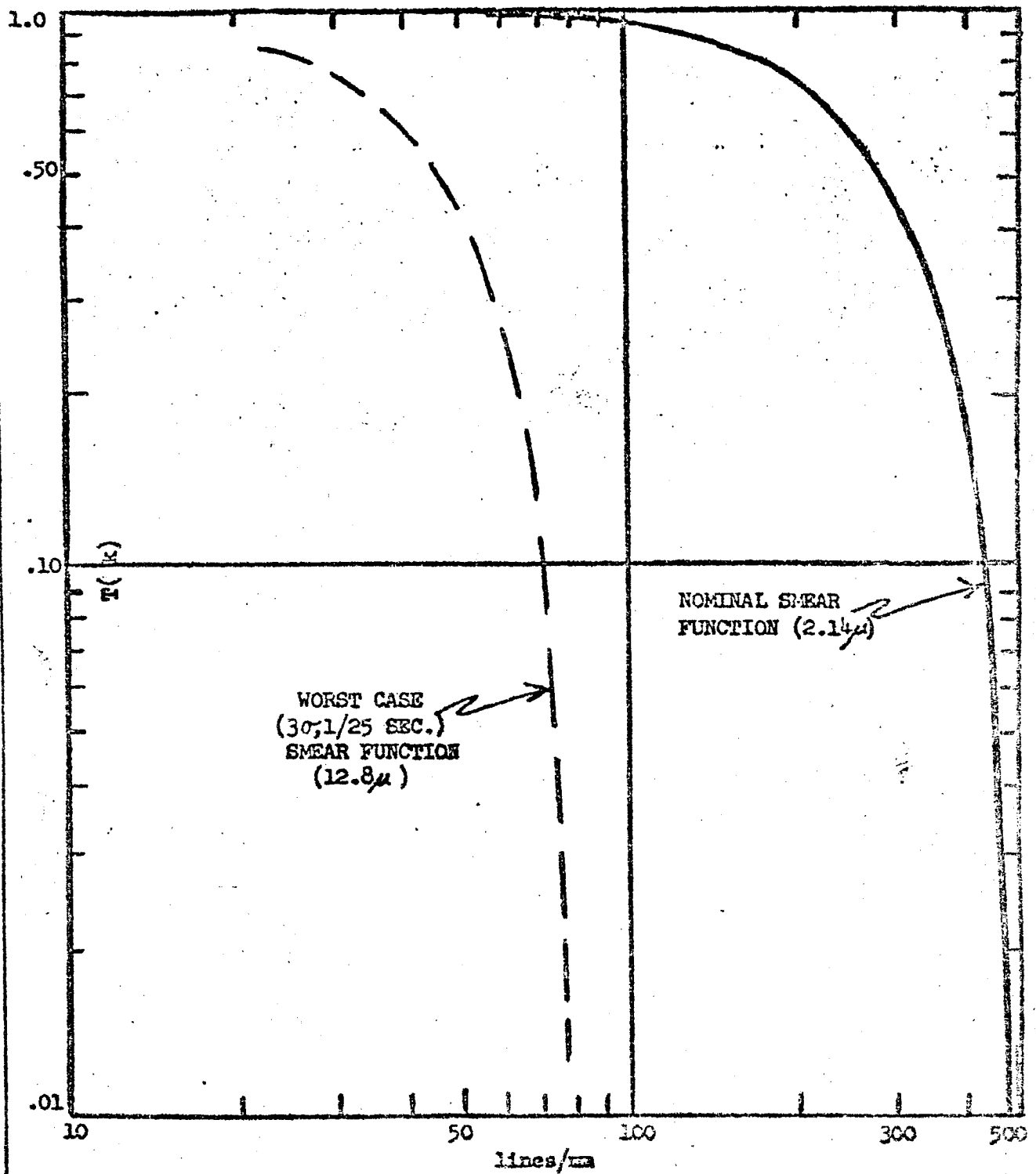


Figure 5.0-2 MODULATION TRANSFER FUNCTION FOR IMAGE

6.0

Natural Environment

The Lunar orbiter will be subjected to characteristics of the space environment, which are of concern to its photographic capabilities, during transit to the moon, and while in lunar orbit prior to completion of its photographic mission. Of primary concern are the effects of ionizing radiation encountered during transit through the belts of geomagnetically trapped radiation near Earth and that originating from solar particle events. Radiation reaching the film results in fogging the photographic film which degrades contrast and thus resolution.

Meteoric particles and, near the moon, ejecta from their impact on the lunar surface may also constitute a hazard to the photographic system by damage to the optical surfaces. Lack of data, other than mostly conjectural or inferred, on the flux of such particulate matter near the moon makes the extent of this hazard difficult to estimate.

6.1 Radiation

6.1.1 Radiation Environment

The major radiation sources to be considered in the analysis of the Lunar Orbiter environment are: (1) geomagnetically trapped radiation, (2) galactic cosmic radiation, (3) solar wind, (4) solar particle event radiation and (5) solar electromagnetic radiation. A brief description of the characteristics of these radiation sources and their intensities is given below.

6.1.1.1 Geomagnetically Trapped Radiation

Geomagnetically trapped radiation, often referred to as the Van Allen belts, consists of charged particles trapped in the Earth's magnetic field. There are two spatially separated regions of high flux, often referred to as the "inner" and "outer" belts. The particles are predominantly protons in the inner belt and electrons in the outer belt. The energy spectrum is a complex function of B , L space. Sophisticated computer programs have been devised to predict the radiation flux and dose for any mission trajectory. (AFWL-TDR-64-71). Nine lunar orbiter trajectories which cover the anticipated ranges of injection conditions were processed by the trajectory and environment code. The flux of each spectral type of trapped radiation encountered was calculated and integrated over these trajectories. The injection conditions of each of these trajectories are given in Table 6.1-1. The encountered fluxes are strongly trajectory dependent. Trajectories numbered 1, 6 and 11 pass through the inner belt and encounter excessive fluxes of penetrating (hard) radiation. Trajectories numbered 5, 10 and 15, skirt the inner belt, but encounter moderate fluxes of the less penetrating electrons (soft) and protons in the outer belt. The remaining trajectories numbered 3, 8 and 13 encounter significantly lower fluxes by passing through the edges of both belts, thus encountering a spectrum intermediate between the hard and soft spectra. The fluxes of each particle type are shown in Table 6.1-2 for each trajectory.

6.1.1.2 Galactic Cosmic Radiation

Galactic cosmic radiation consists of completely ionized atomic nuclei. It is distinguished from other radiation in the vicinity of the earth by its slow time variation (11 year cycle in anti-correlation to sunspot cycle), its flat energy spectrum, and its origin from outside the solar system. The energy spectrum of galactic cosmic radiation is given in Figure 6.1-1. Note that kinetic energy is given in terms of electron volts per nucleon. The galactic cosmic radiation model employed for this study is given in Table 6.1-3. The radiation dose from galactic cosmic radiation inside the lunar orbiter is approximately 0.5 to 1.0 rad per month.

* A reference frame for the geomagnetic field in which B is the field strength and L the equatorial distance of the flux lines.

| Trajectory Number (Reference) | Launch Azimuth (deg) | Approx. Parking Orbit Coast Time (min) | Parking Orbit Inclination (deg) |
|-------------------------------------|----------------------------|--|---------------------------------------|
| 1 | 93 | 5.3 | 28.43 |
| 3 | 93 | 20.41 | 28.43 |
| 5 | 93 | 34.2 | 28.43 |
| 6 | 102 | 1.6 | 30.2 |
| 8 | 102 | 16.6 | 30.2 |
| 10 | 102 | 24.9 | 30.2 |
| 11 | 111 | 0.2 | 33.84 |
| 13 | 111 | 13.4 | 33.84 |
| 15 | 111 | 23.6 | 33.84 |

TABLE 8.1-1

LUNAR ORBITER TRAJECTORIES

US 4203 2000 REV. 2/64

120

REV SYM _____

~~SECRET~~

NO.

D2-100293 -1

PAGE

124

| Trajectory Number | Protons cm ⁻² (40-80 Mev) ⁻¹ | Electrons cm ⁻² (.5 Mev) | Protons cm ⁻² (5-20 Mev) ⁻¹ | Description of Penetrating Spectra |
|----------------------|--|---|---|---------------------------------------|
| 1 | 4.47x10 ⁶ | 1.42x10 ¹¹ | 3.69x10 ⁸ | Hard |
| 3 | 2.67x10 ⁴ | 1.66x10 ¹⁰ | 2.07x10 ⁷ | Moderate |
| 5 | 2.11x10 ⁶ | 3.39x10 ¹⁰ | 5.66x10 ⁸ | Soft |
| 6 | 4.54x10 ⁶ | 1.53x10 ¹¹ | 3.57x10 ⁸ | Hard |
| 8 | 5.60x10 ⁴ | 1.56x10 ¹⁰ | 2.30x10 ⁷ | Moderate |
| 10 | 8.47x10 ⁵ | 2.85x10 ¹⁰ | 3.65x10 ⁸ | Soft |
| 11 | 4.09x10 ⁶ | 1.44x10 ¹¹ | 3.04x10 ⁸ | Hard |
| 13 | 5.99x10 ⁴ | 1.39x10 ¹⁰ | 1.80x10 ⁷ | Moderate |
| 15 | 1.16x10 ⁵ | 2.55x10 ¹⁰ | 1.07x10 ⁸ | Soft |

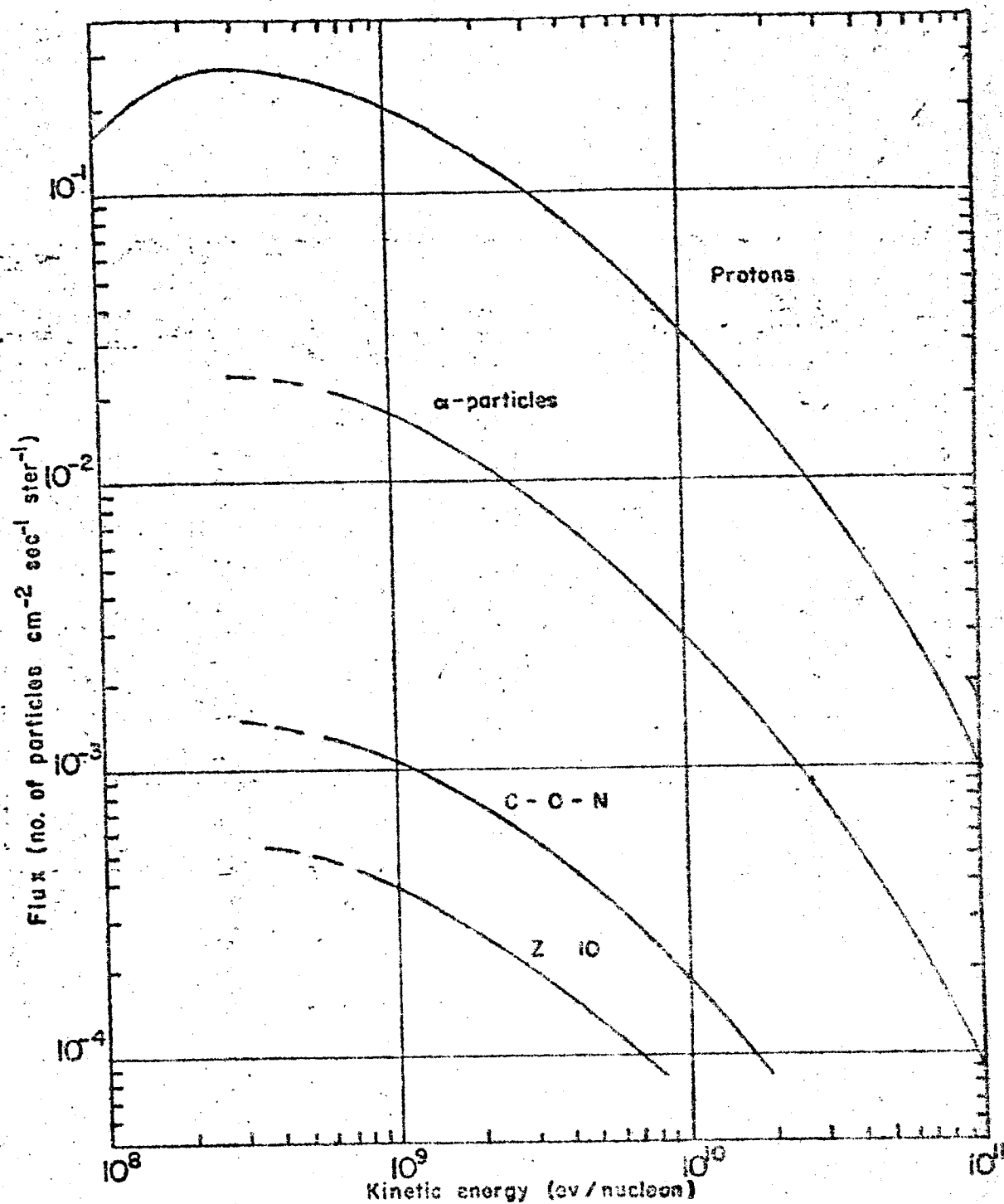
TABLE 6.1-2

TRAPPED RADIATION FLUXES ENCOUNTERED BY THE LUNAR ORBITER

| E (Bev/nucleon) | H | He | Li, Be, B | C, N, O, F | Z $\sqrt{10}$ |
|--------------------|------|-----|-----------|------------|---------------|
| .15 | 8790 | 940 | 16.3 | 53 | 18.2 |
| .20 | 8790 | 925 | 15.4 | 50 | 17 |
| .40 | 8160 | 816 | 12.6 | 41 | 14 |
| .60 | 7850 | 660 | 11.0 | 34 | 13 |
| .80 | 7540 | 560 | 9.7 | 31 | 11 |
| 1.00 | 6910 | 500 | 8.8 | 27 | 10 |
| 2.00 | 4710 | 240 | 5.3 | 15 | 6.0 |
| 4.00 | 2200 | 105 | 2.3 | 6.9 | 2.7 |
| 8.00 | 940 | 50 | .78 | 2.7 | .97 |
| 10.00 | 697 | 40 | .53 | 1.8 | 0.60 |

TABLE 9.1-3

FLUX OF COSMIC RADIATION
PARTICLES PER M² PER SECOND WITH ENERGY
GREATER THAN E



Integral energy spectrum of Primary Galactic cosmic radiation.

Figure 6.1-1

6.1.1.3 The Solar Wind - (from Planet Space Sci. Vol. II No. 8
August 1963, p 885)

Solar wind and storm estimates have been obtained from observations of the zodiacal light, ripples in certain comet tails, whistlers, time lag between the onset of solar flares and magnetic storms, diurnal variation of cosmic radiation, Doppler broadening of emission lines in aurorae, cut-off distance of the geomagnetic field, etc. The extensive literature on this subject was reviewed previously. From these data, Opik arrived at velocities for the protons and α -particles in the solar wind of 200 to 300 km/sec with a flux density of 10^9 protons/cm² sec (210 eV, 50 protons/cm³). Parker summarized the situation by stating that we must be prepared to accept any density value within a factor of 5 of 30/cm³ and velocities within a factor of 2 of 300 km/sec for quiet solar conditions. It is estimated that the positive ion flux is 8% protons, 15% α -particles, 0.1% oxygen and carbon, 10^{-2} % nitrogen and silicon, and 10^{-3} % magnesium, sulphur and iron.

Recently, direct measurements from space probes have been made available. With Explorer X a particle flux of 4×10^8 to 10^9 /cm² sec was measured outside 21.5 Earth radii from the Earth. The protons peak at an energy of 500 eV under quiet conditions and their energy increased to 1000 to 2000 eV during a solar storm on 27 March 1961. Lunik II encountered a flux of between 2×10^8 and 10^9 /cm² sec until it hit the Moon. The most extensive data came from Mariner II. The electrostatic spectrometer showed that a plasma flux from the direction of the Sun was nearly always present at energies of 1664 and 2476 eV. This corresponds to proton velocities of 563 and 690 km/sec respectively. In a two-month period from 29 August to 30 October 1962, eight geomagnetic storms were detected. The plasma density in a storm on 7 October 1962 increased by a factor of 5 and returned to its pre-storm value about 5 hours after the passage of the initial front. Many of the spectra show two peaks. The lower voltage maximum could be due to protons and the higher due to α -particles. For quiet conditions, a plasma flux of 2×10^8 /cm² sec seems to be typical in the region between Earth and Venus orbits. The solar wind model employed in this study is given in Table 4. The radiation dose to the film of L.O. is expected to be negligible from this source.

6.1.1.4 Solar Particle Event Radiation - (largely from D2-90469)

Solar particle event radiation refers to the energetic particles ejected from the sun during, or subsequent, to some solar flares. These particles have been measured by counters and by nuclear emulsions. Analysis of the history of the events and other data, notably riometer data, permits an estimation of the total particle flux per event. The particles reaching the Earth in these events have been found to be primarily protons in most cases with smaller concentrations of alpha particles and heavier nuclei present. In a few events, the alpha particle concentration has been quite large.

| ION | FLUX ($\text{cm}^{-2}\text{sec}^{-1}$) | (KM/sec) | E(kev) |
|--------|--|-------------|---------------------|
| PROTON | | | |
| Quiet | $2 \times 10^8 \text{ p/cm}^2 \text{ sec}$ | 600 KM/sec | 1.85 |
| Storm | $2 \times 10^9 \text{ p/cm}^2 \text{ sec}$ | 1000 KM/sec | 5.00 (1/60 of time) |
| ALPHA | | | |
| Quiet | $.3 \times 10^8 / \text{cm}^2 \text{ sec}$ | 600 KM/sec | 7.4 |
| Storm | $3 \times 10^8 / \text{cm}^2 \text{ sec}$ | 1000 KM/sec | 20.0 (1/60 of time) |

TABLE 8.1-4

SOLAR WIND MODEL

In six events the ratio of alphas to protons at constant rigidity was approximately 1.

The differential spectrum of the particles can be expressed as

$$\frac{dJ}{dP} = \left. \frac{dJ}{dP} \right|_0 e^{-P/P_0}$$

where $P = (\text{momentum}/\text{charge})$ is the particle rigidity. This can be converted to a differential energy spectrum by using the relation $P = 1/Z (E^2 + 2 ME)^{1/2}$, where J is the total integrated intensity in an event.

Thus,

$$\frac{dJ}{dE} = \left. \frac{dJ}{dP} \right|_0 \frac{(E-m)}{Z (E^2 + 2 ME)^{3/2}} e^{-\frac{1}{P_0} (E^2 + 2 ME)^{1/2}}$$

This spectrum adequately fits the spectrum over the entire energy range at any time during the event. However, $\left. \frac{dJ}{dP} \right|_0$ and P_0 are both functions of time.

Early in an event, the low energy component is small. Later, the relative number of high energy to low energy particles decreases. Thus, P_0 is large at first and later decreases.

The time behavior of an event is often very complicated, especially in the case of multiple events. For single events, the time dependence of J_0 can be approximated by an exponential decay both forward and backward in time from the time of maximum J_0 . The e-folding constant for the increasing flux (negative time) varies from 2 to 30 hours. For the decreasing flux, the constant ranges from 8 to 40 hours. The location on the sun of the flare which produced the particles strongly influences these time constants. Flares occurring on the east limb of the sun have the longest time constants while those occurring on the west limb have the shortest. The time delay between the flare and the arrival of the first particles also depends on flare location. Particles from east limb flares may take 3 to 5 hours to reach the Earth, while particles from west limb flares typically require at most a few minutes to one-half hour. The transit time of the particles is much longer than would be required for a straight trajectory. This is a result of the twisted, weak magnetic field that exists between the Sun and the Earth. This field is equivalent to a scattering medium through which the particles must diffuse. Although the field is highly irregular, it has some symmetry. The outward streaming of the solar wind pulls the field out from the sun while the rotation of the sun coils it into a spiral. The difference between the time constants of the east limb and west limb flares is explained on this basis. The east limb particles must diffuse across the coiled field lines while the west limb particles can more closely follow the field lines to reach the Earth.

Table 6.1-5 gives the peak particle fluxes and characteristic rigidity for the events measured in solar cycle 19. Table 6.1-6 gives the information available on the alpha particle fluxes in solar particle events.

6.1.1.5 Solar Electromagnetic Radiation

High energy (> 20 kev) solar X-ray emission both during flares and during quiet times has been measured with detectors carried in rockets and balloons (Chubb, Friedman, and Kreplin, 1960 a, b, 1962), (Acton, Chubb, Kreplin, and Meekins, 1963), (Kreplin, 1961, 1964a, b), (Winckler, May and Masley 1961), (Peterson and Winckler, 1959), and (Vette and Casal, 1961). The observation of X-rays in the quantum energy range 20 to 70 Kev during three flares accompanied by SID's led Friedman to suggest that the presence of such X-rays appeared as an extension of the high intensity flux of 2 to 10 A X-rays, which are the main components responsible for flare time enhanced D-layer ionization (SID). It has been shown statistically by Dodson, Hedeman, and Covington (1954), Hachenberg and Kruger (1960), and Kawabata (1961), that centimeter-wave bursts are closely associated with SIDs. Elvert (1961) theoretically computed the intensity of X-rays by thermal emission from very hot regions and showed that the effective temperature of centimeter-wave bursts ($10^7 - 10^8$ °K) is sufficient to explain the X-rays observed by Friedman during rocket flights. Peterson and Winckler (1959) first proposed a nonthermal mechanism for the production of X-rays and suggested that the hard X-rays originate as bremsstrahlung owing to the braking of high velocity electron jets in the flare or the photosphere. In the development of this concept, DeJager (1960) predicted a close association between meter-wave type III bursts (fast frequency drifting bursts) and flare X-rays. DeJager implied that the passage of type III electron streams through the corona would be sufficient to produce the X-rays. This appeared to be confirmed by subsequent observations of Winckler, May and Masley (1961). Table 6.1-7, excerpted from Kreplin, 1964 b, gives the total energy deposited per cm^2 per sec at the Earth during quiet times and during solar flares for 15 measurements dating from 9/29/49.

6.1.2 Radiation Dose to the Film

The inherent shielding provided by the vehicle structure and equipment must be calculated first to predict radiation dose to the film of the Lunar Orbiter. In early analyses of the preliminary design vehicle, shielding was studied by a system of solid angle sectors about the camera. It was found that only two solid angles need be considered. One is established by the vehicle structure and systems, and the second by the camera package skin only. Subsequently, the major effort was directed toward determining the solid angle subtended by the second sector above, with the greatest possible accuracy. The center of the film package was taken as the dose point in the calculations.

| EVENT DATE | PEAK FLUX (Particles/cm ² sec) | P ₀ (Mv) |
|------------|--|---------------------|
| 2/23/56 | 10,000 | 195 |
| 3/23/58 | 8,000 | 64 |
| 7/ 7/58 | 1,000 | 62 |
| 8/16/58 | 30,000 | 64 |
| 5/10/59 | 39,000 | 84 |
| 7/10/59 | 15,000 | 104 |
| 1/11/60 | 400 | - |
| 4/28/60 | 250 | 104 |
| 5/ 4/60 | 150 | 127 |
| 9/ 3/60 | 450 | 127 |
| 9/26/60 | 300 | 73 |
| 11/12/60 | 32,000 | 124 |
| 11/15/60 | 22,000 | 114 |
| 11/20/60 | 2,200 | 118 |
| 7/20/61 | 400 | 120 |
| 9/28/61 | 500 | 121 |

TABLE 6.1-5

PEAK FLUX OF PROTONS/CM² ABOVE 10 Mev AND CORRESPONDING CHARACTERISTIC RIGIDITY
P₀ SOLAR CYCLE 19

| EVENT DATE | PEAK FLUX* (Particles/cm ² /sec) | AVERAGE CHARACTERISTIC RIGIDITY (Mv) | ** $\frac{J_p(>P)}{J_\alpha(>P)}$ |
|------------|--|--|--------------------------------------|
| 3/23/58 | 420 | 85 | 1.5 + 0.5 |
| 5/10/59 | 5,000 | 75 | 1.5 + 0.5 |
| 7/10/59 | 800 | 95 | 3 + 1 |
| 11/12/60 | 4,000 | 170 | 2 + 0.5 |
| 11/15/60 | 4,200 | 145 | 1.8 + 0.5 |

TABLE 6-6

SOLAR ALPHA PARTICLE EVENT PEAK FLUXES SOLAR CYCLE 19

* Flux of particles $E > 10$ mev/nucleon

** Ratio of protons to alpha particles above the same rigidity

| DATE | TIME UT | SOLAR CONDITION | ENERGY ERGS/CM ² /SEC FOR $\lambda < 8 \text{ \AA}$ ASSUMING 2×10^6 °K DISTRIBUTION |
|----------|------------|--|---|
| 9/29/49 | 1730 | 2 1/2 hrs. after Class 1 Flare (26) | 1.5×10^{-3} |
| 5/ 1/52 | 1459 | Quiet (21) | 1.7×10^{-3} |
| 5/ 5/52 | 1344 | Quiet (23) | 0.5×10^{-3} |
| 11/15/53 | 2240 | Quiet (1.7) | $.007 \times 10^{-3}$ |
| 11/25/53 | 1546 | Quiet (3.0) | $.003 \times 10^{-3}$ |
| 12/ 1/53 | 1529 | Quiet (2.5) | --- |
| 10/18/55 | 2250 | Quiet (9.6) | --- |
| 7/20/56 | 1915 | Class 1 or 1 - Flare | 5.0×10^{-3} |
| 8/20/57 | 1650 | Class 1 Flare | $.64 \times 10^{-3}$ |
| 8/29/57 | 2113 | Class 2 Flare | 15×10^{-3} |
| 7/24/59 | 1634 | Class 3, Surge, Prominence | 13×10^{-3} |
| 8/ 7/59 | 1705 | Quiet (114) | 1.0×10^{-3} |
| 8/14/59 | 1600 | Quiet (138) | 1.0×10^{-3} |
| 8/24/59 | 2247 | 2 + Flare, Max 2239 | 26×10^{-3} |
| 8/29/59 | 1610 | Quiet (132) | 3.3×10^{-3} |
| 8/31/59 | 2252 | 2 + Flare, Max 2252 | $> 220 \times 10^{-3}$ |
| 9/ 1/59 | 1700 | 2 + Flare, Max 1702 | $> 88 \times 10^{-3}$ |

TABLE 6.1-7

X-RAY INTENSITIES

U2 4288 2000 REV. 3/64

REV SYM _____

~~SECRET~~

NO. D2-100293-1

PAGE

134

Sectoring was based upon a coordinate system centered on the dose point and with each axis parallel to the corresponding vehicle axis. This is illustrated in Figure 6.1-2 where X, Y and Z are vehicle axes and X', Y' and Z' are those of the dose point. The relation between the vehicle coordinates and the dose point, referenced to the center of the camera package, are:

$$\begin{aligned} X &= 4.14 \text{ inches} \\ Y &= 7.75 \text{ inches} \\ Z &= 4.38 \text{ inches} \end{aligned}$$

The procedure used in performing the sector analysis was, in principle, as follows: A polar angle, θ_1 , measured from the -X' axis in the X'Z' plane was determined as the first point where only the photo package skin afforded shielding. The angle θ was increased to θ_2 where vehicle structure again contributed to the shielding. Values of θ_1 and θ_2 were determined for each 10° increment of the azimuthal angle, ϕ , measured from the +Z' axis in the Z' Y' plane. The effective solid angle corresponding to that shielded only by the photo package skin, $\Delta \Omega_2$, was computed according to the relation

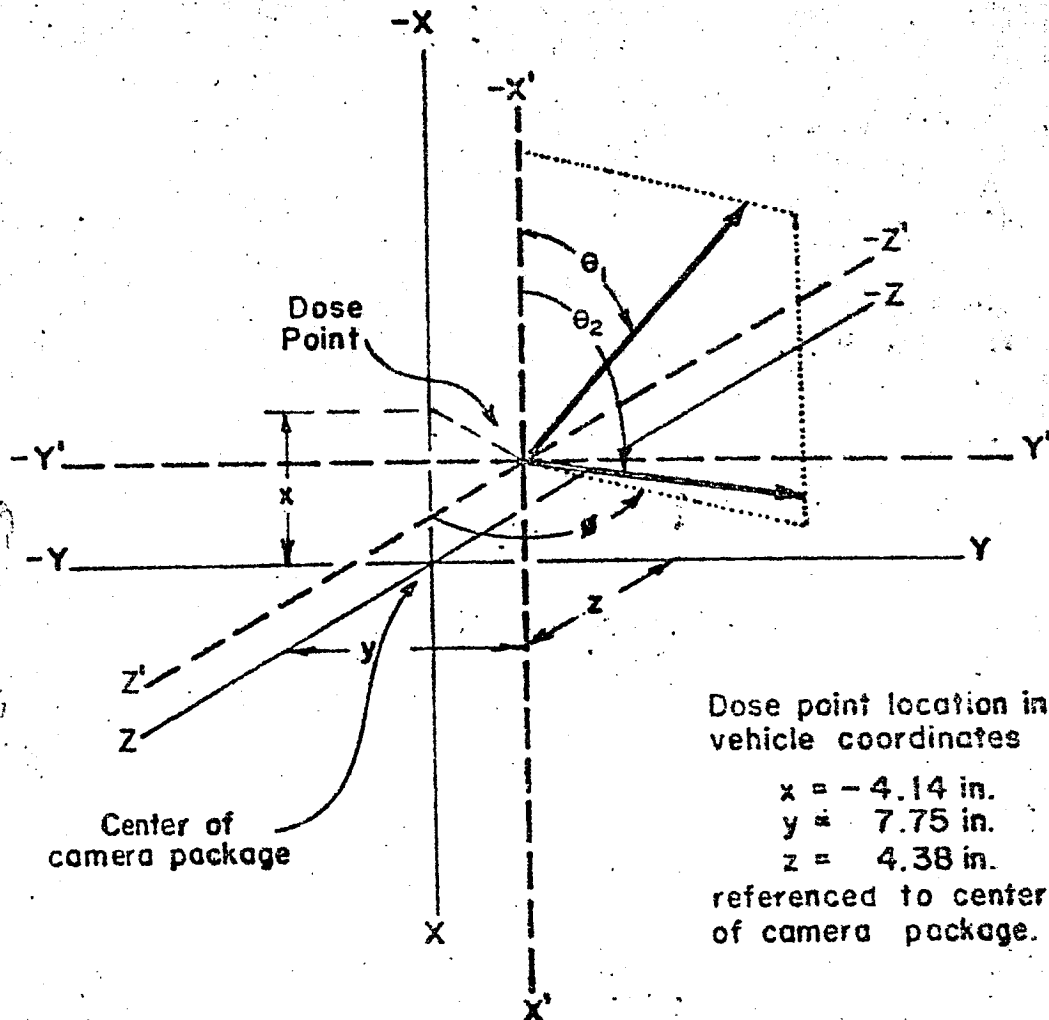
$$\Delta \Omega_2 = \int_0^{2\pi} \int_{\theta_1}^{\theta_2} \sin \theta \, d\theta \, d\phi$$

and found to be 7.944 steradians. For omnidirectional radiation, the ratio

$$\frac{\Delta \Omega_2}{4\pi} = 0.632$$

is the proportional part of the radiation shielded by only the photo package skin where the shielding is equivalent to 2 gm./cm². The remainder, 0.368, is the equivalent solid angle providing a shielding of ≥ 5 gm./cm².

The doses for the trajectories considered and the environment assumed are given in Table 6.1-8. The event chosen as an example of the radiation dose received from a solar particle event is that of July 18, 1961, the eighth largest recorded in the last eight years. The exponential rigidity spectrum for this event is described by $J_0 = 3.1 \times 10^9$ particles/cm² and $P_0 = 102$ Mv. The dose at the film surface for the shielding conditions specified is 46.4 rads. Since the years 1956-57 are equivalent to 1966-67 in the solar cycle, a statistical study of the solar particle events in 1956-57 has been carried out. On the basis of this study, the integral probability vs. flux curve in Figure 6.1-3 has been constructed. This figure indicates that there is roughly a 10% chance of receiving a cumulative flux equivalent to the single event discussed above.



Dose point coordinate system and sector angle relations

Figure 6.1-2

| <u>Trajectory No.</u> | <u>Proton Dose (Rad)</u> | <u>Electron Dose (Rad)</u> | <u>TOTAL Dose (Rad)</u> |
|---------------------------|------------------------------|--------------------------------|-----------------------------|
| 1 | 2.23 | 6.70 | 8.93 |
| 3 | .007 | .074 | .081 |
| 5 | .667 | 1.489 | 2.16 |
| 6 | 2.29 | 7.52 | 9.81 |
| 8 | .016 | .057 | .073 |
| 10 | .31 | 1.14 | 1.45 |
| 11 | 2.07 | 7.42 | 9.49 |
| 13 | .023 | .053 | .076 |
| 15 | .048 | .612 | .66 |

Table 6.1-3

Dose Table for Lunar Orbiter Techniques

4-5143-2

US 4235 2000 REV. 8/62

REV SYM_____

DOEING

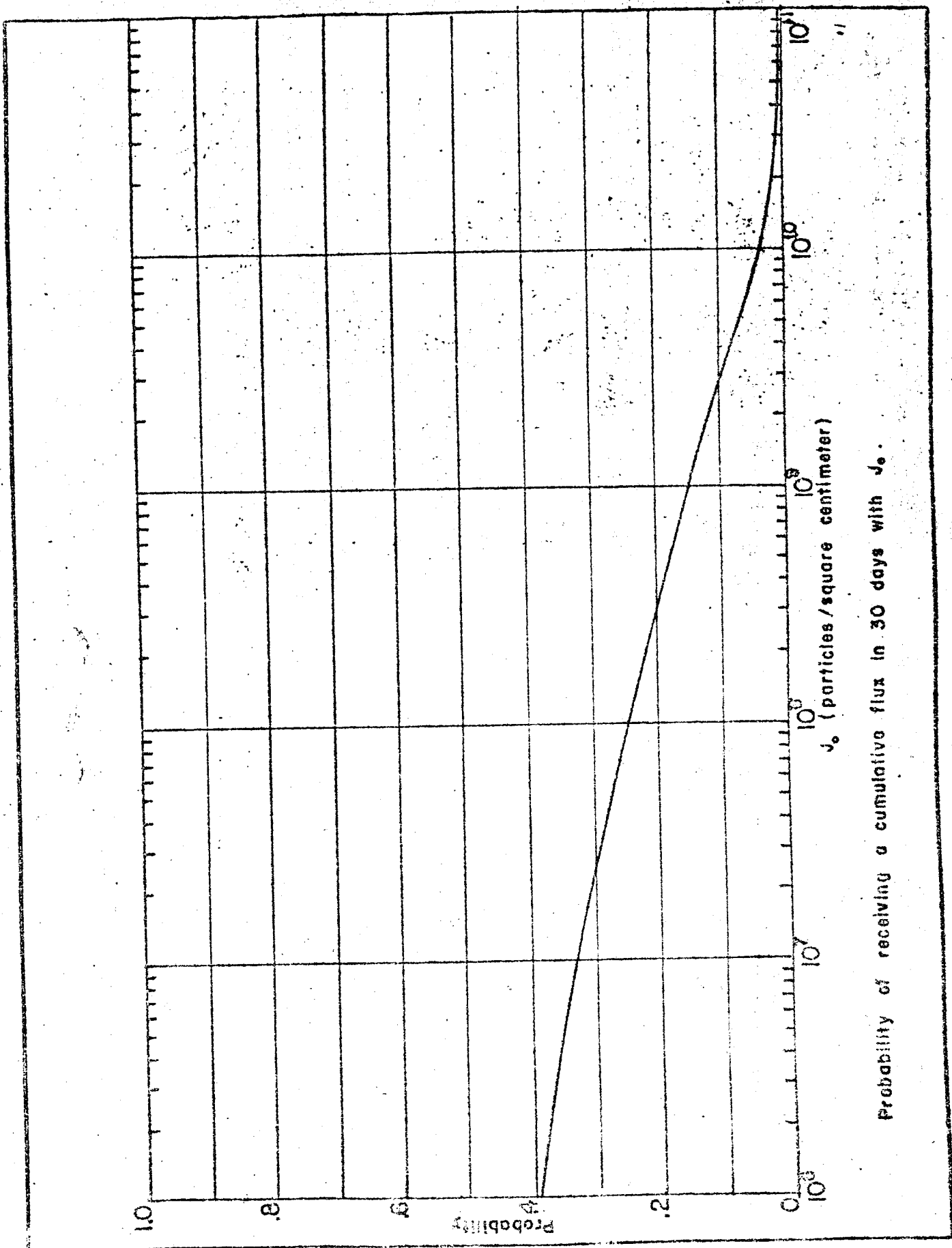
NO.

D2-100293-1

SECT.

PAGE

137



US 4208 2000 REV. 2/68

Figure 6.1-3

REV SYM _____

NO. 12-100293 -1

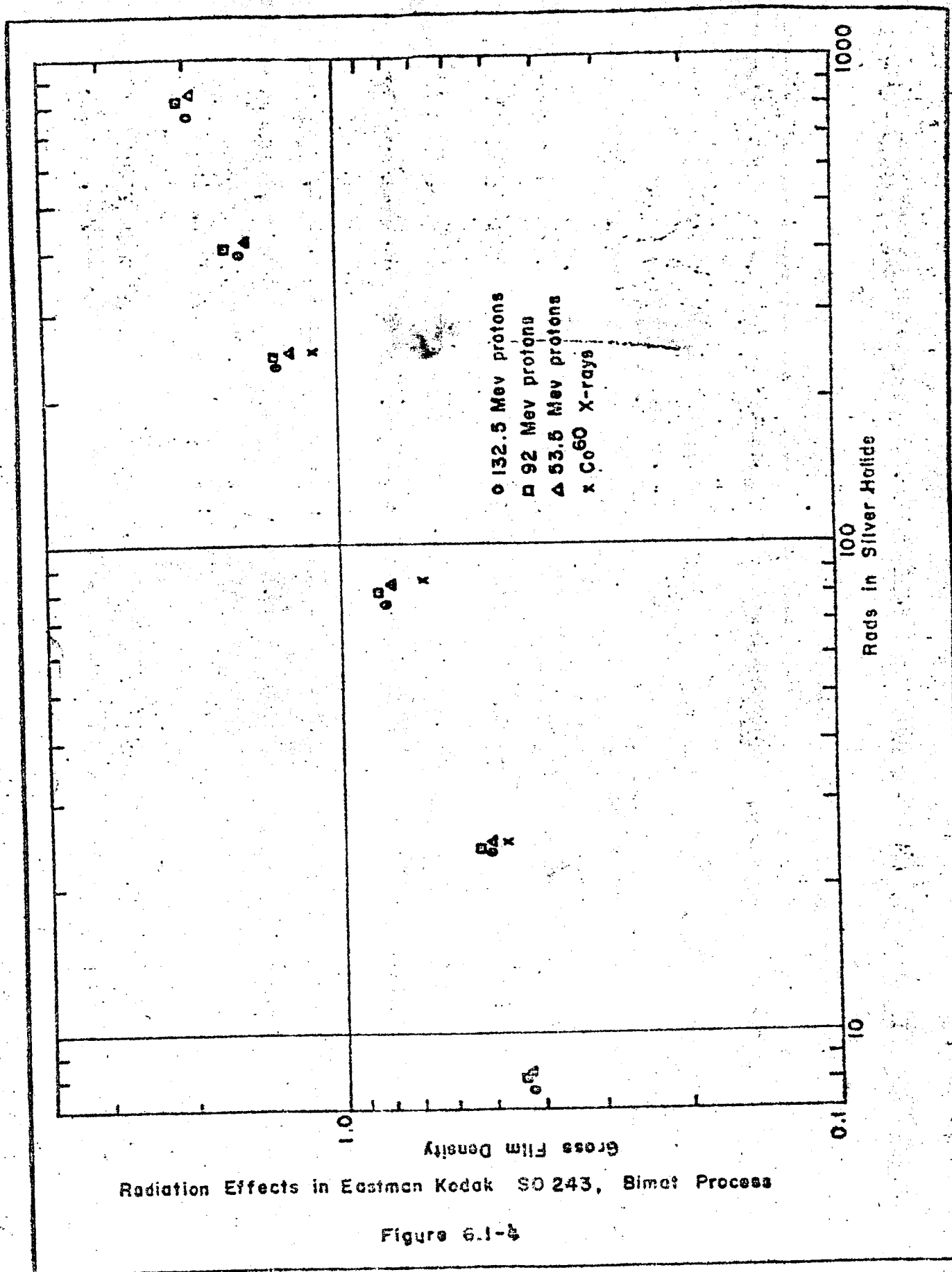
PAGE 138

6.1.3

Film Damage Criteria

Ionizing radiation (protons, electrons, alpha particles, and energetic electromagnetic radiation) effects photographic film by darkening it just as light does. Therefore, when film is exposed to ionizing radiation, as well as image-forming light, the effect is similar to that of any other non-image-forming exposure. In general, the sensitivity of film to ionizing radiation is proportional to the speed of the film.

The response of S.O. 243 film employed in the IO to Co⁶⁰ and 53, 92, and 132 Mev protons is given in Figure 6.1-4, -5 and -6. These data indicates that a damage threshold is a few rads and that the film is unusable in IO at 100 rad. The criteria are tentative until data on low energy protons, alpha particles, electronics, and electro-magnetic radiation are obtained.



US GPO 2000 REV. 2/84

REV SYM _____

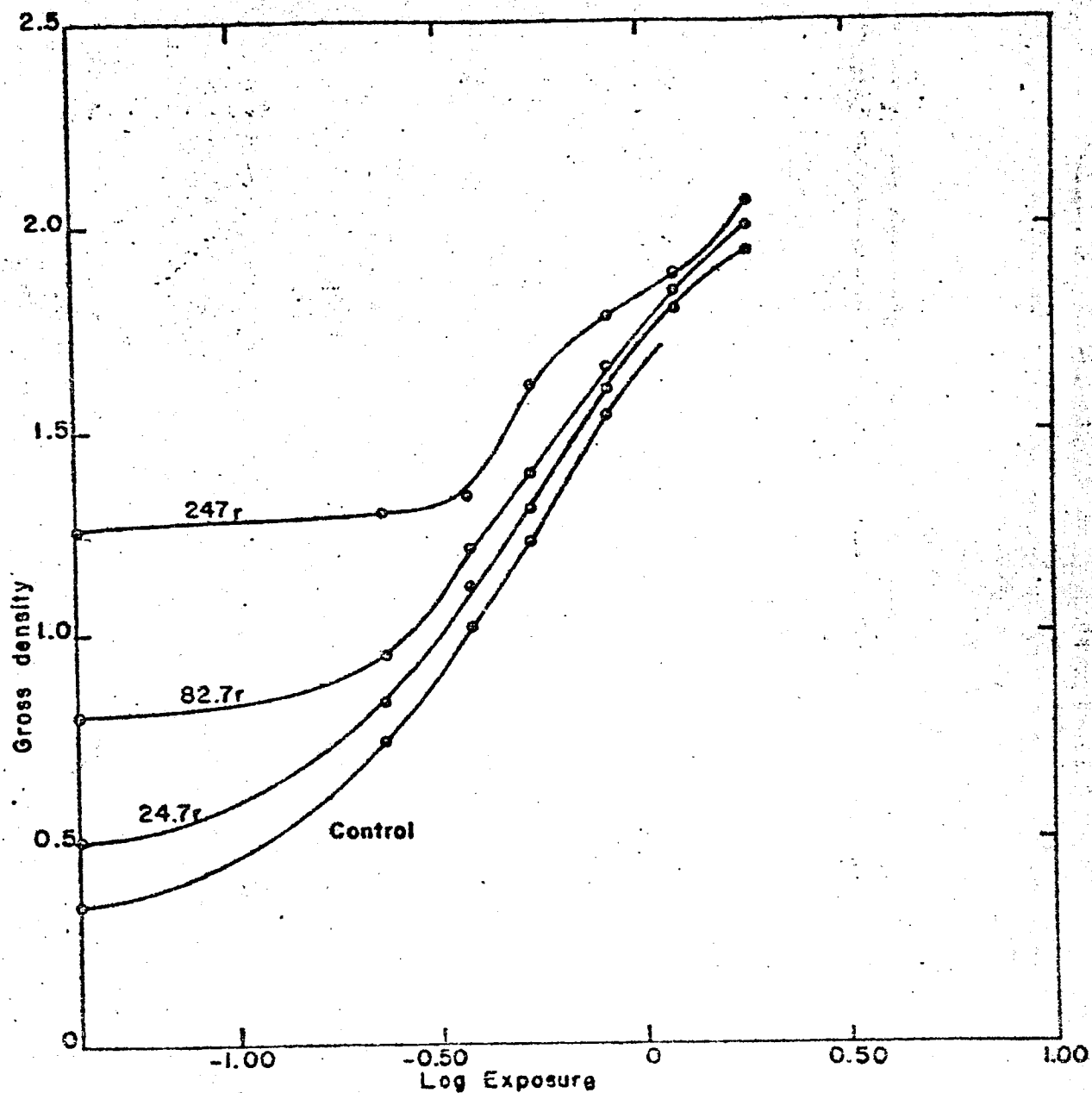
~~SECRET~~

NO.

D2-100293 -1

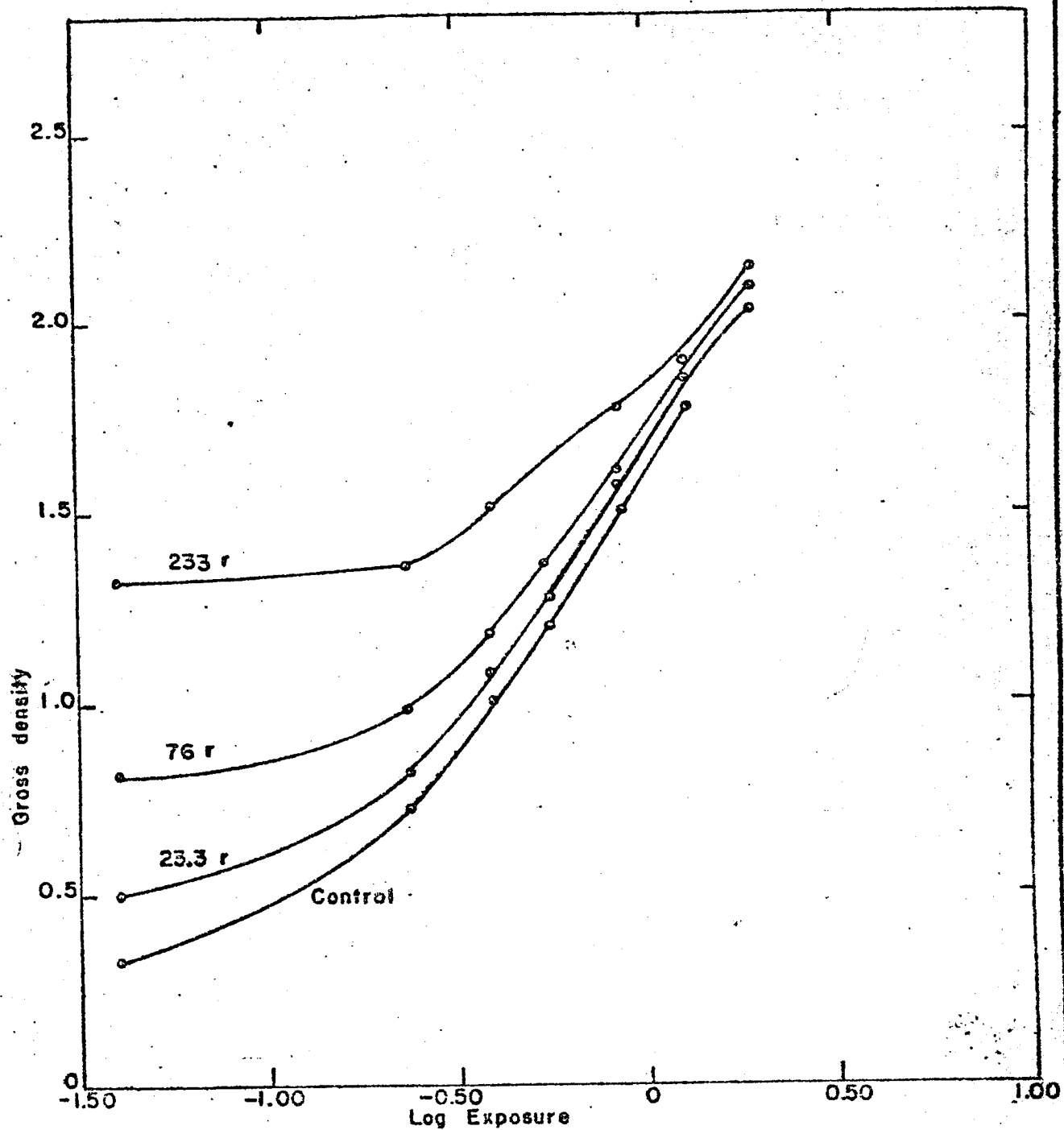
PAGE

140



Radiation Effects in Eastman Kodak SO 243, Bimat Process, 53.5 Mev protons (rads given in silver halide).

Figure 6.1-5



Radiation Effects in Eastman Kodak SO243, Bimat Process, 132.5 Mev protons (rads given in silver halide).

Figure 6.1-6

U3 4288 2000 REV. 3/64

REV SYM _____

BOEING

NO. D2-100293-1

PAGE

142

Conclusions

Although the calculations presented here are preliminary in nature, some major conclusions may be drawn:

- 1) The radiation dose to the film from the encountered trapped radiation may exceed the tolerance level.
- 2) Total mission failure due to one large or several small solar particle events has a probability of occurrence of about 10% or less.
- 3) Present data indicates that radiation damage to film by solar X-rays, solar wind, and by cosmic rays is not significant.
- 4) Shielding equivalent to 2 gm./cm² has been provided in the design.

Section 6.1 References

- Acton, Chubb, Kreplin, and Meekins, J. Geophys. Res., 68, 3335, 1963
- Chubb, Friedman, and Kreplin, Space Research, "Proceedings of the First International Space Science Symposium", January 11-16, 1960 a
- Chubb, Friedman and Kreplin, J. Geophys. Res., 65, 1831, 1960 b
- Chubb, Friedman and Kreplin, J. Geophys. Res., 67, 2231, 1962
- Dodson, Hedeman and Covington, Ap. J., 119, 541, 1954
- Elwert, J. Geophys. Res., 66, 391, 1961
- Hachenberg and Kruger, J. Atoms. and Terrest. Phys., 17, 20, 1960
- deJager, Handbook der Physik, L II, Springer-Verlag, Berlin, 1959
- Kawabata, (1961), paper presented at IAU Symposium on Solar Corona, Cloudcroft, 1961
- Kreplin, Annales de Geophysique, 17, 151, 1961
- Kreplin, "NRL Solar Radiation Monitoring Satellite", presented at COSPAR Symposium - Florence, Italy, May 1964 a
- Kreplin, "Solar X-rays and U V Emission", presented at Symposium on Space Weather, April, 1964 b
- Peterson and Winckler, J. Geophys. Res., 64, 697, 1959
- Vette and Casal, Phys. Rev. Let., April 1, 1961
- Winckler, May and Masley, J. Geophys. Res., 66, 315, 1961

6.2

Meteoric Particles

Dr. Z. Kopal (Reference 1), has pointed out that the flux of interplanetary dust and ejecta from impacts of meteoric particles on the lunar surface may constitute a significant hazard to exposed optical surfaces on the Lunar Orbiter. He based this opinion on two papers, one by Hawkins, (Reference 2), and the second by Gault, Shoemaker, and Moore (Reference 3). Hawkins has presented a curve of particle flux as a function of mass as shown in Figure 6.2-1. These data indicate a flux in space of particles having individual masses greater than (1×10^{-15}) gram of $1 \times 10^5/m^2/sec.$, or 10 impacts per sec. per cm^2 . Gault, Shoemaker, and Moore have investigated the effects of hypervelocity impacts of small particles into basalt rock, and have studied the mass-size distribution of the ejecta and its angle and velocity of ejection. The primary objective of this work was to assess the flux of the ejecta at the lunar surface resulting from primary impacts. A number of relationships between the parameters of the primary projectile and the ejecta were presented. They show that the flux of secondary particles at the surface of the moon may be in the range of 4 orders of magnitude greater than the primary flux, but the flux decreases with altitude above the surface to about 10^{-3} surface flux at the nominal LO perilune of 46 km. The combined data from several sources has been used to obtain the mass-frequency plot which is shown as Figure 6.2-2. This plot better demonstrates current knowledge concerning this problem. Attention should be given to the scales represented and the uncertainties in the data.

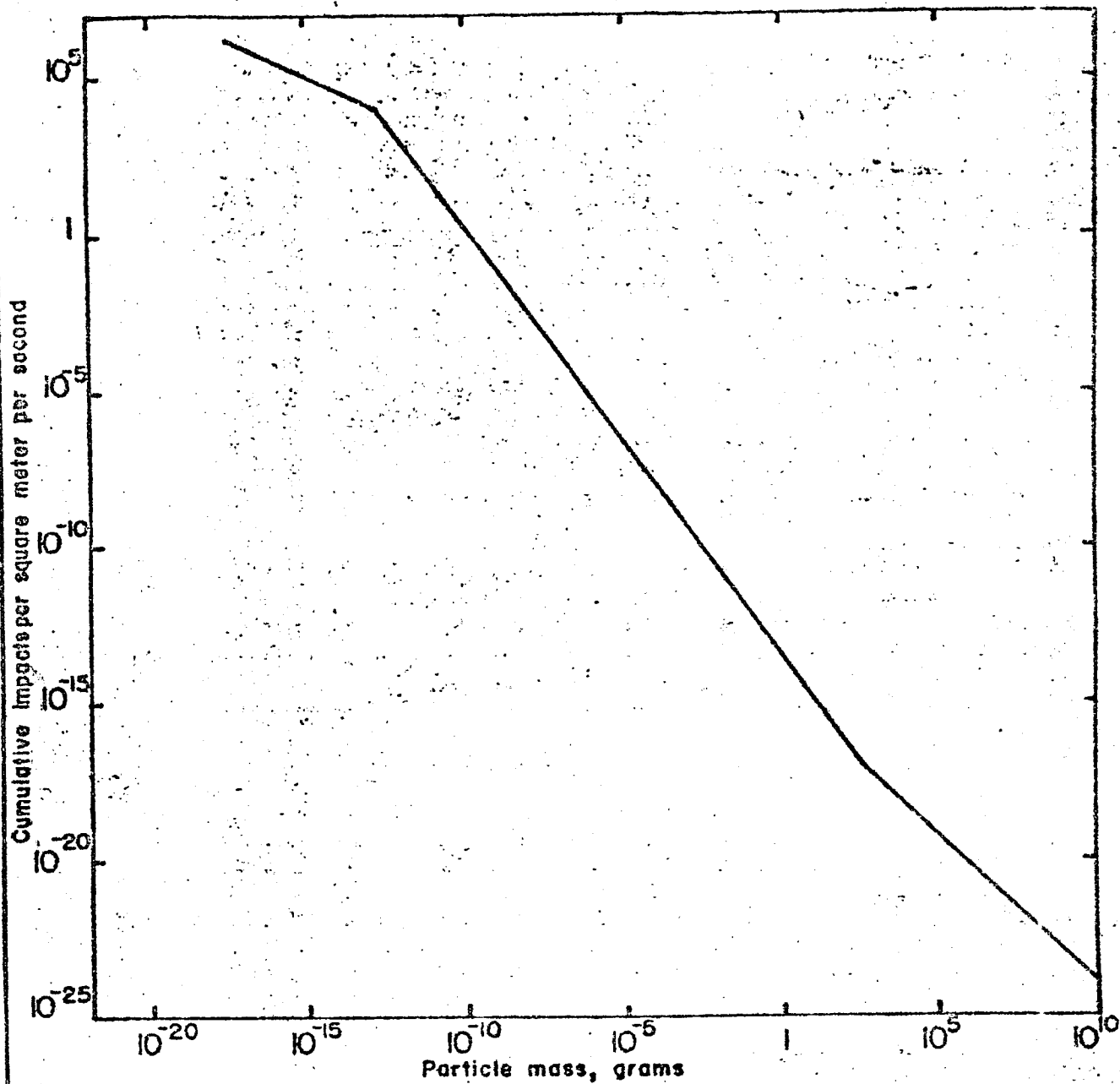
6.2.1

Flux of Particles Impacting the Moon

There are no direct measurements or observations of the flux of particles impacting the lunar surface or in the immediate vicinity of the moon. The only data available is from visual, photographic, and radar observations of meteoric infalls in the Earth's atmosphere, high altitude rocket and satellite measurements, and observations of zodiacal light observations. None of these techniques provide data over the entire range of particle mass occurring as interplanetary debris, and since each method is dependent upon different parameters, the results are dependent upon the correlation between the observed measurement and the mass of the particle. In some cases this correlation is not well established and, in many cases, it is dependent upon an assumed value for a parameter such as velocity.

Observational Methods

Although, as will be shown later, there is an upper limit of particle mass which will be of concern in assessing the hazard to the LO mission, the methods used for observing larger particles will be included.



Flux of extraterrestrial objects. (Hawkins, August 1963.)

Figure 6.2-1

U2 4288 2000 REV. 2/C4

REV SYM _____

DOEING

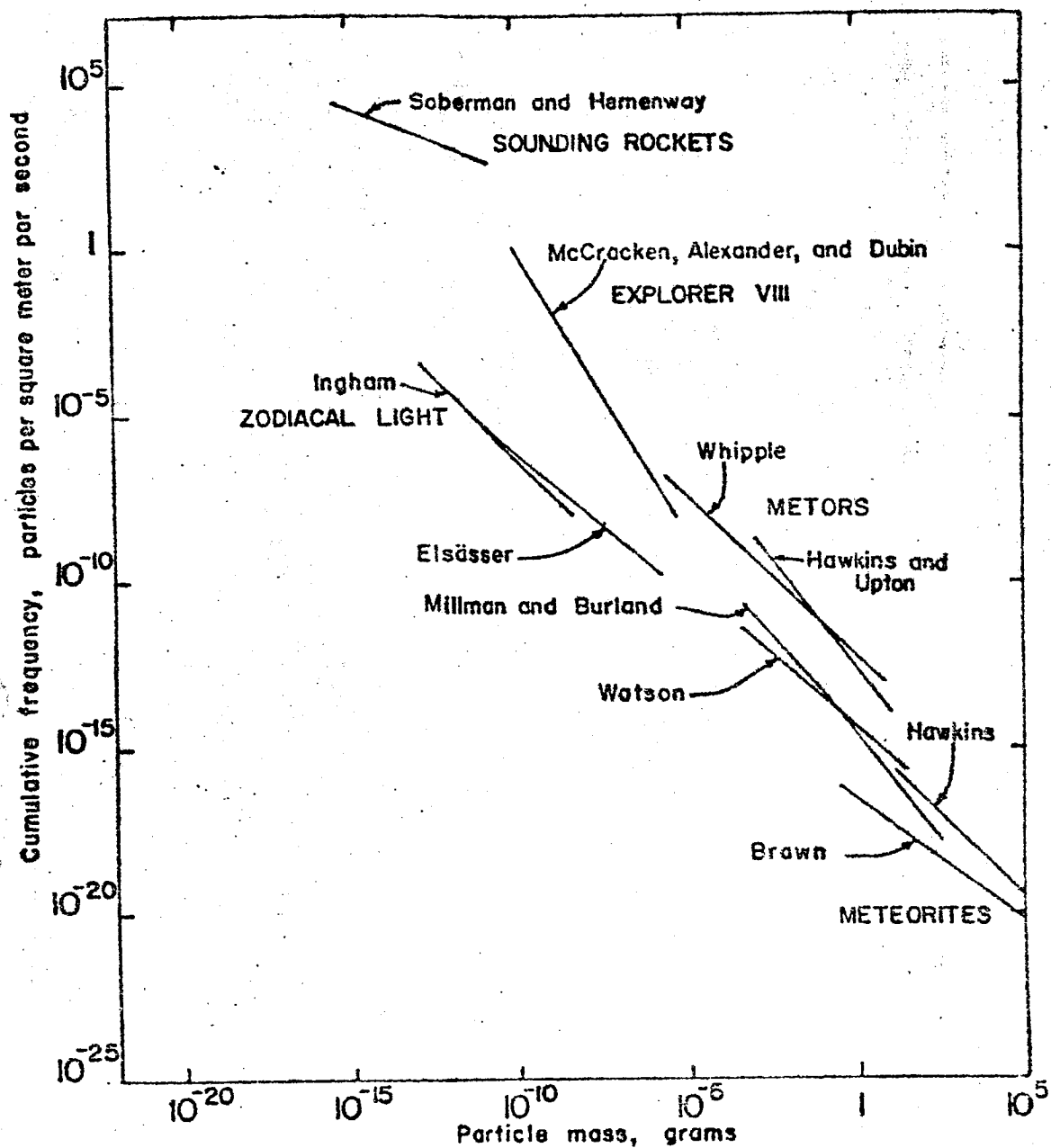
NO.

D2-100293 -1

PAGE

146

142
116



Cumulative frequency-mass distributions for interplanetary meteoric particles.

Figure 6.2-2

Visual Observations

Brown (Reference 4), has estimated the frequency of meteorite impact on the Earth's surface from the numbers of falls over a period of a century in Japan, India and Western Europe. Later, he found that his results had been influenced by the effect of population density on the probability of observation and recovery and revised his estimates upward by a factor of 3.4 (Reference 5). Even where meteorites are recovered, data on the original size or mass of the body cannot be precise because of ablation and break-up during entry through the atmosphere.

In the case of meteors where the particle does not reach the surface, visual observations provide only limited information. The probability of detection decreases as the magnitude increases so that only a few meteors of magnitude greater than about +2 or +3 are seen (+6 is usually considered the limit of visibility of stars). Visual observation provides only an estimate of magnitude and velocity.

Radar and Photographic Observation

Both radar and photographic observations of meteors have some similarities in methods and techniques, in that both determine meteor characteristics in terms of magnitude or brilliance. Photographic methods are dependent upon luminous efficiency, in terms of visual or photographic light from the meteor, which is a function of mass, density, velocity, light intensity, time and a constant γ_0 which relates magnitude and mass (Reference 6). It is apparent that to be photographed, a particle must convert kinetic energy to heat and light, thus its velocity must be reduced before it is detected. It is also apparent that this technique will not detect micro meteorites whose velocity is attenuated at a rate too low to cause light emission. The rate of deceleration and penetration of the atmosphere is also dependent upon the density of the meteoric material. Whipple, (Reference 6), reports estimates of density ranging from 0.05 gm/cm³ to near 1, with a mean of 0.4 gm/cm³. These densities are much lower than that of stones and irons which reach the Earth's surface. The relationship between mass and magnitude adopted by Whipple is $m_0 = 1$ gm, for a zero magnitude visual meteor with a velocity of 30 km/sec. before it enters the atmosphere. An increase of 1 magnitude corresponds to a decrease in particle mass of 2.5. McCracken and Dubin (Reference 7) have adopted Whipple's value of $m_0 = 1$ gm, but point out that Levine (Reference 8) believes that the value should be reduced by a factor of 10 to 100. Other values used have ranged from 0.05 to 25 gms. Hawkins, (Reference 2) used a value of 4.4 grams.

Radar measurements of meteoritic influx are dependent upon radar reflection from the ionized gas produced by the passage of the particle into the atmosphere. During deceleration, about 90% of the energy appears as heat, 1% as light and perhaps less than 1% as ionization (Reference 9). As in the photographic method, radar observations are in terms of magnitude, and a mass-magnitude relationship is required to obtain a mass-frequency distribution. The relation is similar to the photographic and the radar and visual magnitudes are approximately equal (Reference 7). The relationship is not constant and is affected by ionization characteristics in the ionosphere and other variables mentioned for photographic methods. The ionization falls to zero for the very small meteorites, limiting this method to particles larger than about 10^{-4} gm.

Rocket and Satellite Measurements

Distributions of interplanetary dust have been defined on the basis of about 10,000 impacts on space vehicles. The microphone detector, and piezoelectric crystals with photomultipliers for detecting light flashes from impacts, and other sensors have been used. McCracken, Alexander, and Dubin (Reference 10), determined the mass distribution function for the range of 10^{-6} to 10^{-10} gm. using data from Explorer 1, Vanguard III and Explorer VIII. An average velocity of 30 km/sec. was assumed to convert the measured impact momentum to mass data. The direct measurement of particle impacts from satellite and rocket sensors have shown large fluctuations in flux including daily variations often greater than one or two orders of magnitude (Reference 11). Variations of two orders of magnitude are attributed to dust showers associated with meteor streams.

Zodiacal Light

Photometric data on the zodiacal light and the solar corona have been analyzed a number of times in order to obtain information about the interplanetary matter (Reference 12). The results from such studies are generally expressed in terms of the number density of particles of a given radius at a certain distance from the sun. There is lack of agreement concerning the range of particle size that contributes most to the scattered light in interplanetary space. The radii favored by different observers vary from a fraction of a millimeter down to the radiation pressure limits (0.4μ). The comparison of spacial densities derived from direct measurements and zodiacal light studies indicates that the spacial density of dust particles near earth is about 10^3 times greater than in interplanetary space.

It is of interest to note that Bowen (Reference 12), observed that the rate of meteors recorded by radar varied with lunar phase. Brierley and Davis (Reference 13), investigated the Jodrell Bank data for December 1954 - November 1955 and from November 1956 to December 1958 and found a correlation which seemed to confirm

Bowen's findings. The physical mechanism is uncertain.

For the present purposes it will be assumed that the curves of flux are the best approximations of available data. Figure 6.2-2 presents the best available estimate of the flux of particles impacting the lunar surface. McCracken and Dubin (Reference 7) believe that the data obtained by Soberman and Hemmenway (Reference 14) from high altitude rocket for the very small particles (Venus Flytrap) is not applicable for the vicinity of the moon and that the data by Ingham (Reference 15), and Elsasser (Reference 16) is more nearly correct. The uncertainty then, is possibly two or three orders of magnitude in the case of particles having a mass $>10^{-5}$ gm. and as much as 5 orders of magnitude for masses $>10^{-5}$ gm.

6.2.2 Effects of Impacts

The hazard to a vehicle orbiting the moon from the impact of particulate matter arises from two sources: (1) the flux of primary cosmic debris and (2) ejecta thrown out from the moon by impacts of the primary particles on the lunar surface. The extent of the hazard from (1) is a function not only of the flux, but also of the character and velocity of the impacting particle and the time of exposure of critical surfaces to the flux. In the case of (2) this flux may be in addition to (1), depending upon position and orientation of the surfaces with respect to the velocity vector of the particles. Gault, Shoemaker, and Moore (Reference 3) have indicated that the flux of ejecta from the lunar surface will be a function of the flux of impacting particles. Their data is based upon experimental studies of ejecta resulting from the impact of small projectiles on massive basalt. Projectile velocities of about 6.5 km/sec., were obtained and results extrapolated to impact velocities of 15 and 28 km/sec.

The effects of hypervelocity impacts of small particles (<1 gm.) on the lunar surface is a matter of conjecture because of the lack of knowledge of the surface properties of the moon and of the effects of impacts of average meteoric velocity. Many techniques have been used to derive a concept of the lunar surface properties. The data seem to indicate a surface of fine dendroidal structure on a layer of very low bulk density material having a depth of from 10 cm to several meters (17, 18, 19). Experiments on deposition of dust under high vacuum have shown that molecular bonding occurs and the surface layer will not be loose and fluffy but may have a sintered character. Exposure of bare rock is expected to be uncommon although thermal measurements reveal anomalous cooling rates near some large rayed craters (Tycho, Aristarchus) which may be indicative of bare or thinly covered rock.

Direct experimental studies of hypervelocity impacts is limited in application to lunar studies, since impact velocities equaling meteoric impact velocities have been achieved only within the lower limits. Most of the work has been done using metal targets and thus is not directly applicable. Gault, et al, have impacted basalt and have also impacted projectiles in quartz sand. Gault, Heitowit, and Moore (Reference 20), report recent observations that impacts into sand and pumice targets result in forms of ejecta of complex structure and form that are totally unlike the parent material. They report that "Ejecta from pure quartz sand targets (43% porosity) contain lumpy, shagreen-textured aggregates of finely crushed quartz grains bonded together with fused and partially fused grains. Glassy material including slender rods and fibers resembling segments of pulled taffy has also been observed. Fantastically contorted aggregates with dendritic structure have been recovered from pumice targets." Their observations indicate a progressive change in the physical characteristics of the ejecta with increasing target porosity. McCracken and Dubin (Reference 7) point out that reasons exist for believing that the effects of hypervelocity impacts on a surface of dendroidal structure would be considerably different from those of impacts on metals, rock, sand, or dust. The major reason for this difference is the compressibility of the material. The momentum of the projectile would be absorbed in the essentially inelastic medium. At high velocities the projectile may fracture, but the fragments would be trapped in the compressible porous matrix. Experimentally, very little, if any, ejecta results from such an impact. For impacts in a dendroidal structure the projectile can penetrate deep below the surface and, while fracturing, can disperse into the medium. If the projectile impacts a solid material underlying the dendritic structure, it may trap the ejecta or lower its velocity, depending upon the thickness of the overlying material, and the size and velocity of the projectile.

Because of the uncertainty regarding the nature of the lunar surface, any estimate of the flux of ejecta resulting from primary impacts is also extremely uncertain and the validity of an evaluation of the resulting hazard should be considered very questionable.

6.2.3 Meteoroid Hazard to the Photographic System

An attempt to use numbers in assessing the possible damage to the LO camera lens from impacts of particulate material is extremely difficult, and it may be questioned whether the results are even "ball park" answers. The starting point must be the curve for cumulative mass distribution and, as pointed out by Dubin and McCracken (Reference 21), some sections of the approximate cumulative mass distribution curve are based on speculation, especially for particles with masses less than about 10^{-13} gm. It is noted that the curve for near-Earth dust particles with masses smaller than about 10^{-8} gm. departs markedly from the constant-mass-per-magnitude curves used to represent results from meteor observations.

From Figure 6.2-2 it is seen that the flux of particles 1 gram or larger is about 1×10^{-14} per square meter per second. The hazard of such a particle impacting the vehicle is thus low enough virtually to be ignored. The lunar area of interest is approximately 4×10^6 km² and extends for 1/3 the lunar circumference. Without considering the variation in velocity due to the elliptical orbit, the vehicle will, then be over the area of interest about 1/3 of the time, or 1×10^6 seconds per month, or 2.5×10^{-1} sec. per square kilometer. The rate of impact of 1 gram particles is shown to be 1×10^{-8} /km²/sec. This would indicate a probability of about 10^{-9} that the vehicle would be over any particular square kilometer at the time of impact of a 1 gram particle. It would seem that a 1 gram meteoroid is an upper-limit of size that need be considered, on the basis of frequency of occurrence, as stated by Kopal (Reference 1), from the standpoint of primary impacts of ejecta thrown out at high angles and velocities.

The minimum particle mass which may be of concern may be approximated, if a few more assumptions are made.

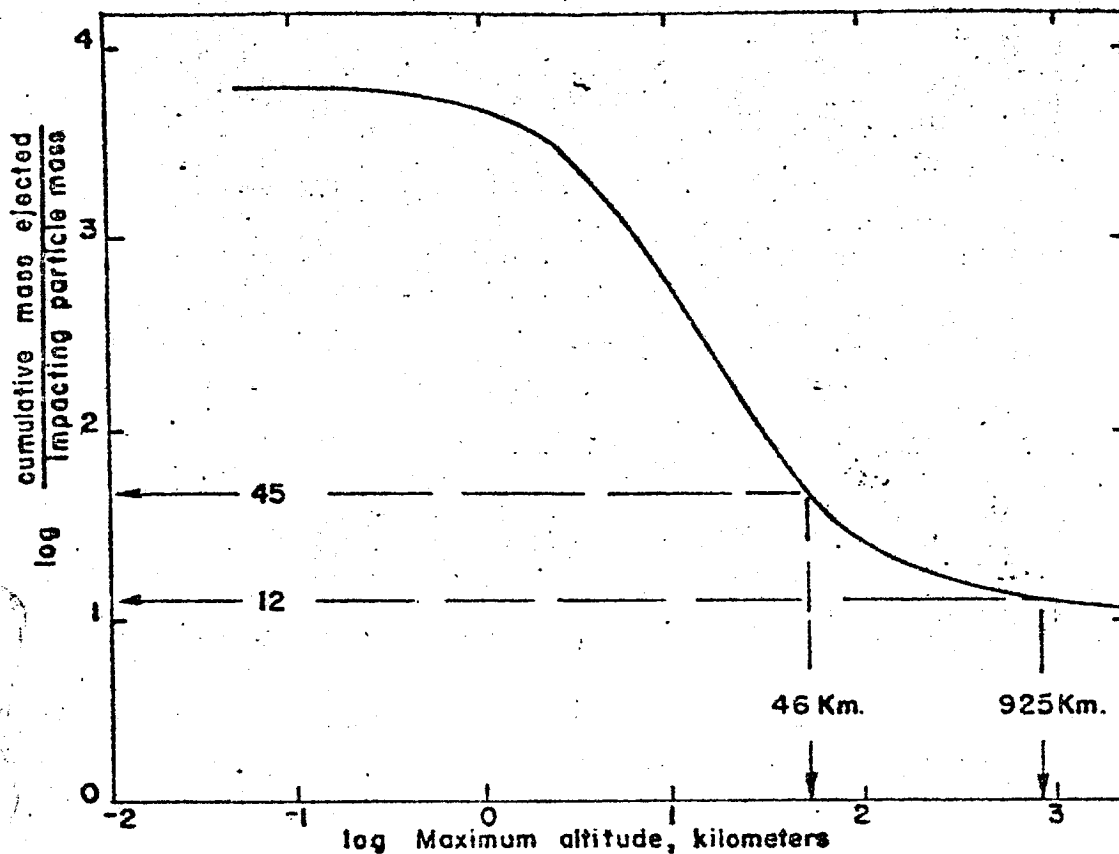
If a pit of 0.5 radius is set as the lower limit of size, which is considered damaging to a lens, it will require excavation of about 5×10^{-2} gram. Gault, et al, have used a value of $1/8 \times 10^8$ gm/erg as the relation between impact energy and ejected mass for the small projectile impacts. Formation of the above pit will then require an impact energy of 4×10^{-3} erg. Assuming a velocity of 30 km/sec. for the impacting particle, the required mass is

$$m = \frac{2E}{V^2} = 1 \times 10^{-15} \text{ gram}$$

An extrapolation of Ingham's data on Figure 6.2-1 indicate a flux of particles of mass 10^{-15} gm. or greater, of about 1×10^{-1} /m²/sec., while Hawkins' curve, Figure 6.2-2 indicates 1×10^5 /m²/sec. When the LO vehicle approaches the moon it is believed that ejecta produced by impacts of meteoric particles on the moon may appreciably increase the impact hazard. The work by Gault, et al, has been used to obtain insight to this problem although there may be much uncertainty concerning direct application of their findings.

In order for an ejecta fragment from the lunar surface to constitute a hazard to the LO, it must attain at least the perilune altitude of 46 km. Using the plot of ejecta mass vs. maximum altitude given by Gault, et al, redrawn here as Figure 6.2-3, it is seen that the flux of ejecta at 46 km would be 45 times the mass of primary particles.

There is no established relationship between the size of ejecta particles and their velocity and ejection angle. Thus there is no basis for estimating what proportion of a size range within the ejected mass will reach or exceed the perilune altitude. It has been noted that the size distribution of meteoric material from asteroidal size on down approximates the well known comminution law derived from studies of rock crushing and grinding. This relation was used by Gault, et al, to derive the size distribution



Ejecta from 28 kilometer per second impacts. Ratio of ejected mass to impacting particle mass above the lunar surface. From Gault, Shoemaker, and Moore, 1963 (Reference 3).

Figure 6.2-3

within the ejected mass of impact cratering. It seems reasonable, then, to assume that the size distribution within the ejecta flux follows that of the primary particles. If this logic holds, the curve of Figure 6.2-2 may be used to indicate the total flux of particles by increasing the indicated flux scale by a factor of about 50. This approximation was also suggested by Kopal (Reference 1). Similarly the particle flux at other altitudes may be approximated according to a factor obtained from Figure 6.2-3.

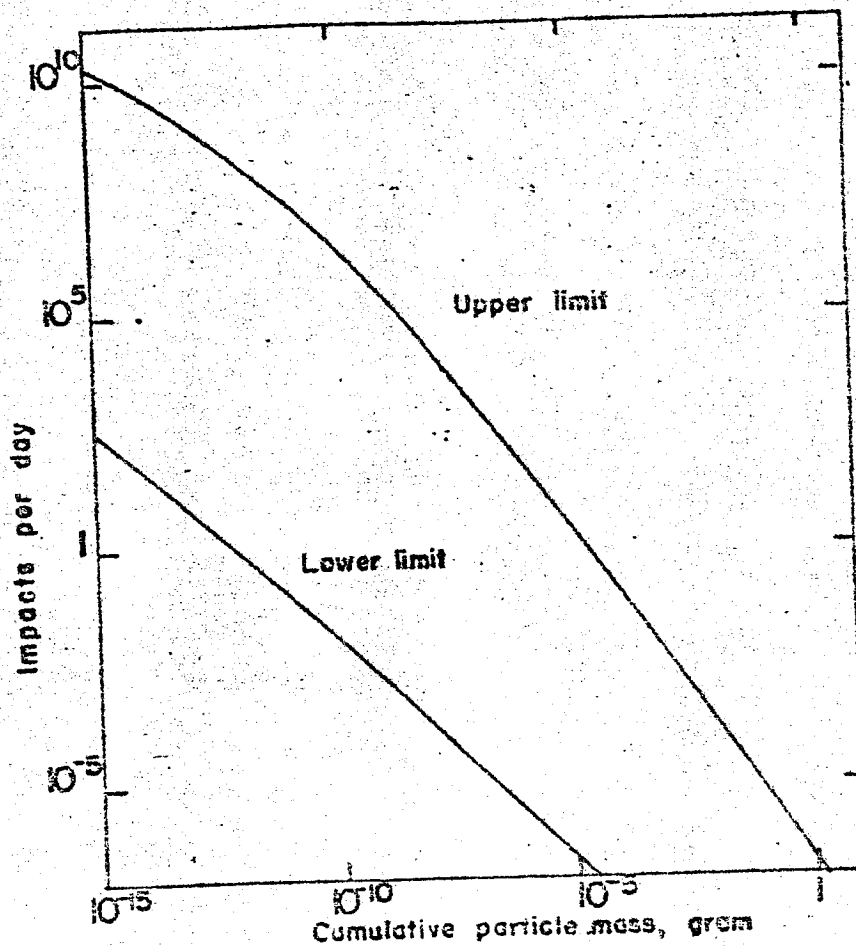
From Figures 6.2-2 and 6.2-3, the impacts which may occur on the lens area at perilune altitude may be estimated within the bounds of the observed flux. This is shown in Figure 6.2-4. It should be pointed out, however, that this curve is based upon the assumption of no directional effect. Since the vehicle is oriented in inertial space over most of the orbit, the hit rate on the lens will vary as a result of its changing orientation with respect to its velocity vector. At times when the lens is pointing more nearly in the direction of travel, the hit rate will be at a higher rate than when the camera is pointing away and the vehicle provides shielding.

When a particle strikes the lens, it will produce a pit - if its mass is great enough, if its velocity is high enough, and if its density is not too low. By assuming a velocity averaging 30 kilometers per second, the pitting relationship given by Gault, et al, and the flux rates shown, the rate of pitting of a lens may be approximated within the limits of the flux data. This has been done as shown in Figure 6.2-5.

Since the data on flux rates is so uncertain, the possible rate of pitting may be considered from a somewhat different standpoint. By assuming that the pitting follows the relationship between mass and velocity, the rate of pitting as a function of flux rate may be computed. This is shown as Figure 6.2-6 where the following is assumed:

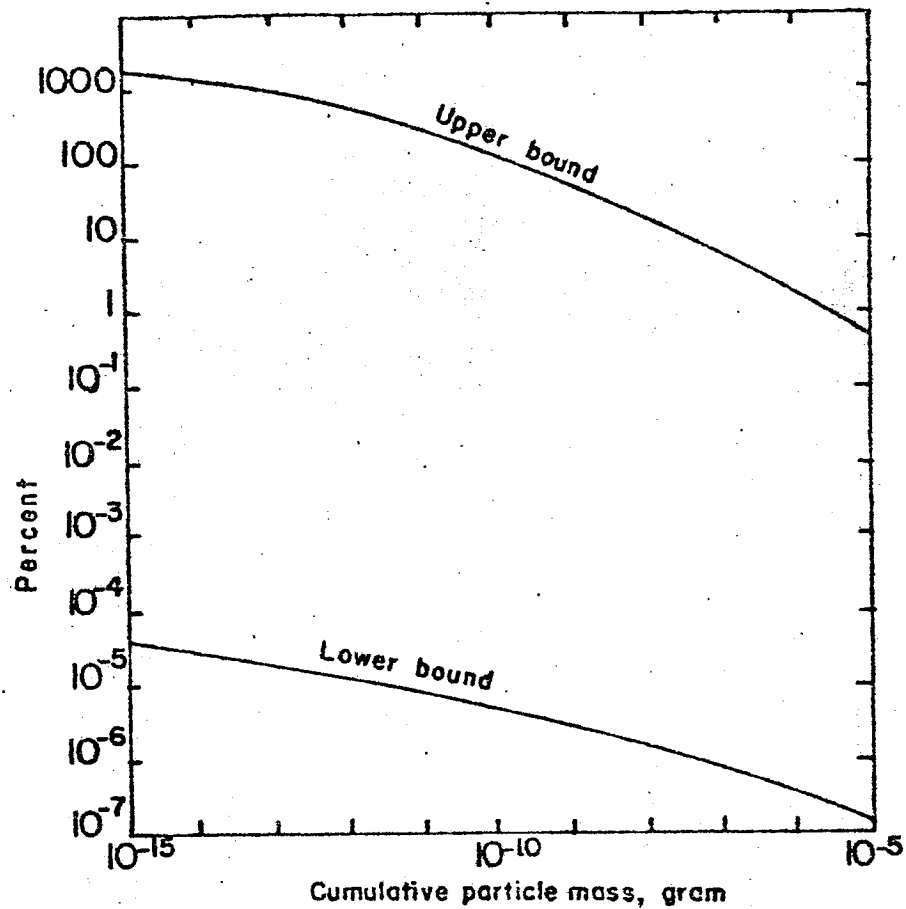
- Perilune flux is the space flux increased by the ejecta factor $K = 50$
- Impacting particle velocity is 30 km/sec.
- Mass excavated by impact is 10^{-9} gm. per erg
- The pit is hemispherical
- The lens is not shielded
- The flux is of particles with mass greater than 10^{-15} gram

The effect of pitting on the optical characteristics of a lens is not known quantitatively. Because of this, there is no reliable method of relating the curve of "Impacts per day", Figure 6.2-5, to degradation of resolution or picture quality.



Estimated number of particle impacts per day on lens area at perihelion altitude of 46 kilometers.

Figure 6.2-4



Percent of lens area pitted per day by particle impacts at perilune.

Figure 6.2-5

US 4283 2000 REV. 2/64

REV SYM _____

BOEING

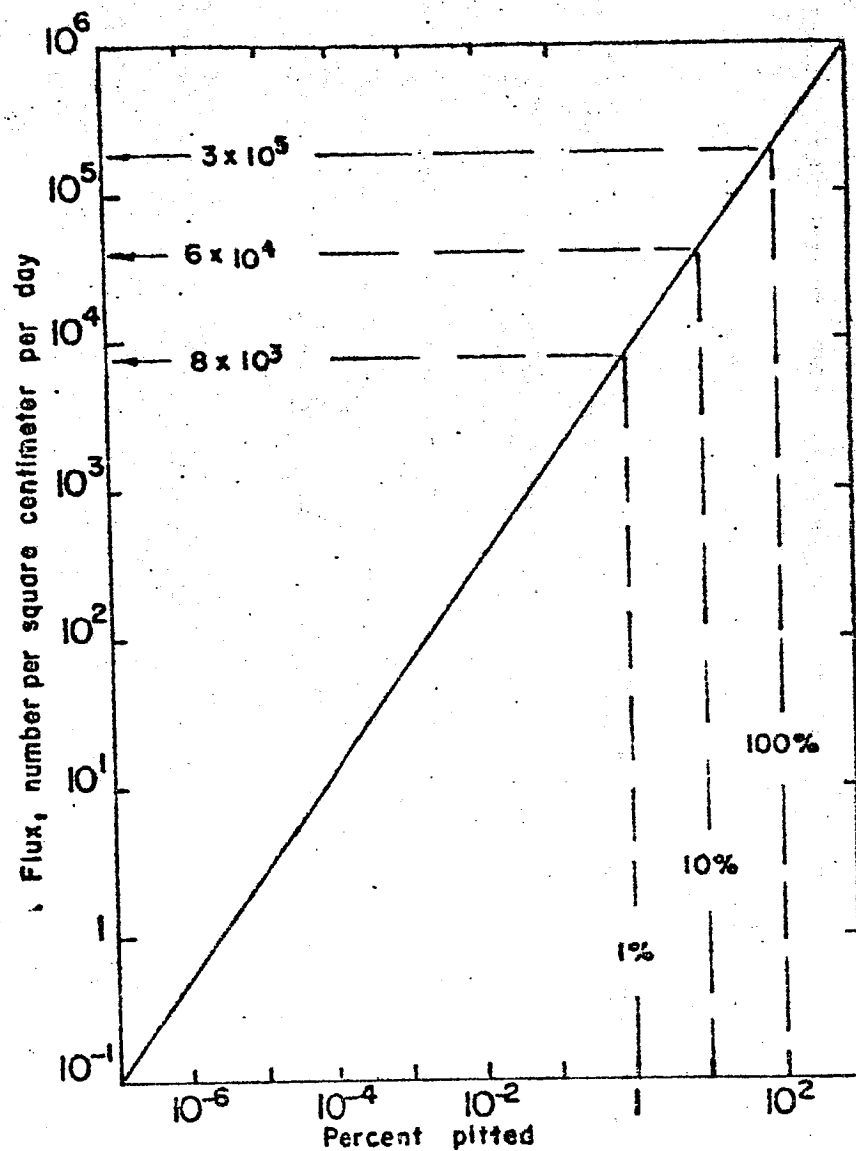
NO. T2-100293-1

PAGE

156

152

156



Percent of lens surface pitted per day at perilune as a function of the flux of meteoric particles.

Figure 6.2-6

U3 4228 2000 REV. 3/64

REV SYM _____

DOEING

NO.

D2-100293-1

PAGE

157

References for Section 6.2

1. Kopal, Z., Conference at The Boeing Company, March 30, 1964.
2. Hawkins, G.S., "The Meteor Population", Harvard College Observatory, Smithsonian Astrophysical Observatory, Research Report No. 3, August, 1963.
3. Gault, D.E., Shoemaker, E.m., and Moore, H.J., "Spray Ejected from the Lunar Surface by Meteoroid Impact", NASA Technical Note D-1767, April 1963
4. Brown, H., "The Density and Mass Distribution of Meteoritic Bodies in the Neighborhood of the Earth's Orbit", J. Geophys. Research, No. 65, pp. 1679-1683, 1960
5. Brown, H., "Addendum: The Density and Mass Distribution of Meteoritic Bodies in the Neighborhood of the Earth's Orbit", J. Geophysics, Res. 66 (4), pp. 1316-1317, April 1961
6. Whipple, F. L. "On Meteoroids and Penetration", J. Geophys. Res. 66 (17) pp. 4929-4939, September 1, 1963.
7. McCracken, C. W., and Dubin, M. "Dust Bombardment on the Lunar Surface", NASA Technical Note D-2100, December 1963
8. Levine, B. "Fragmentation of Meteor Bodies", Nature 196 (4854) pp. 527-528, November 10, 1962
9. McKinley, D. W. R., "Introduction: Symposium - Small Meteoric Particles in the Earth's Neighborhood", The Astronomical Journal 67 (5) pp. 233, June 1962
10. McCracken, C. W., Alexander, W.M., and Dubin, M., "Direct Measurement of Interplanetary Dust Particles in the Vicinity of the Earth", NASA Technical Note D-1174, December 1961
11. Dubin, M., Alexander, W. M., and Berg, O.E., "Direct Measurements of Cosmic Dust Showers", NASA Technical Note D-1544, January 1963
12. Bowen, E.G., "A Lunar Effect on the Incoming Meteor Rate", J. Geophys. Res., 68 (5): pp. 1401-1403, March 1, 1963
13. Brierley, D.M., and Davis, J.G., J. Geophys. Res. 68 (22), November 15, 1963
14. Soberman, R.K., and Hemenway, C. L., "Micrometeorite Collection from a Recoverable Sounding Rocket", GRD Research Note 71, R. K. Soberman, ed., Article III, Nove. 1961, pp. 41-50
15. Inham, M. F., "Observations of the Zodiacal Light from a Very High Altitude Station, IV. The Nature and Distribution of the Interplanetary Dust", Monthly Notes, Ray Astronomical Soc., 122 (2), pp. 157-175, 1961

U2 4283 2000 REV. 3/64

REV SYM _____

| | | |
|--------|------|-------------|
| BOEING | NO. | 12-100293-1 |
| | PAGE | 158 |

154

16. Elsasser, H., "Die raumliche Verteilung der Zodiakallicht materie", Zeit. F. Astrophys., 33 (4), pp. 274-285, 1954
17. Hapke, B. and VanHom, H., "Photometric Studies of Complex Surfaces, with Applications to the Moon", J. Geophys. Res. 68(15), pp. 4545-4570, August 1, 1963
18. Hapke, B. "A Theoretical Photometric Function for the Lunar Surface", J. Geophys. Res. 68 (15), pp. 4571-4586, August 1, 1963
19. Hapke, B., "Packing Properties of Fine Powders and Depth of the Lunar Dust Layer", Cornell Univ., Center for Radiophysics and Space Research, Ithica, N. Y., CRSR-147, June 20, 1963
20. Gault, D. E., Heitowit, E. D., and Moore, H. J., "Ejecta with Complex Structures from Craters formed by Hypervelocity Impact", Abstract of paper to be presented at the 45th Annual Meeting, American Geophysical Union, Washington D.C., April 21-24, 1964, Trans. Am. Geophys. Union, 45 (1), p. 74, March, 1964
21. Dubin, M. and McCracken, C. W., "Measurements of Distributions of Interplanetary Dust", Astronomical Journal 67 (5), pp. 248-256, June, 1962
22. Wood, J. A., "Physics and Chemistry of Meteorites" in: The Moon, Meteorites and Comets, Vol. IV, The Solar System, ed. Barbara M. Middlehurst and Gerard P. Kuiper, Univ. of Chicago Press, 1963, Chap. 12, pp. 337-401

7.0 Monitoring Techniques

The principal sources of information for monitoring and calibrating the photo subsystem after the Lunar Orbiter has been launched are pre-exposed film edge data, time track data, and telemetry data. The requirements for and method of utilizing these data will be discussed below.

7.1 Pre-Exposed Film Edge Data

The requirement for pre-exposed edge data arises from the need to determine insofar as possible a calibration on the photo subsystem readout for resolution, linearity, exposure, density stability and scale. Since the data is pre-exposed, it checks the film processing, readout and reconstruction system, but not the camera itself. There will be no absolute measure of the actual resolution achieved on the lunar surface since objects of accurately known size and spacing on the lunar surface are not available. However, the pre-exposed data will provide a known exposure of a known target to be compared with a calculated exposure of an inaccurately known target, the images of which will be processed, read out and reconstructed in exactly the same manner. Variations in the readout and reconstruction process in flight may readily be compared with performance achieved in testing on the ground.

7.1.1 Resolving Power Bar Charts

System resolution is expected to be such that one meter resolution will be obtained on the lunar surface. For the photo subsystem parameters, this corresponds to approximately 76 lines/mm on the spacecraft film. Resolving power bar charts which bracket this resolution by a substantial margin are consequently required. The proposed format, Figure 7.1-1, will include three sets of bars and spaces with pitches varying from 32 to 160 lines/mm. On the ground, due to a magnification factor of 7.5:1 between ground and airborne image size, the corresponding range of bar spacing is 4.3 - 21.4 lines/mm.

Each set will consist of a low and a high contrast chart. One set of bars will be transverse, one parallel and one 45 degrees to the long dimension of the film. The high contrast resolving power test targets will have in the 32 lines/mm frequency pattern minimum density (light bars) no more than .05 above the first (1st) step density of the density tablet. The maximum density (dark bars) will be at least as great as that of the ninth (9th) step. The low contrast resolving power test targets will have in the 32 lines/mm frequency pattern an apparent minimum exposure (light bars) equal within $\pm .05$ in log exposure to that of the fifth (5th) step of the grey scale. The apparent maximum exposure in this pattern will be $0.30 \pm .05$ in log exposure greater than the minimum exposure. A microscope mounted on the quality evaluation viewer will provide the necessary magnification to conveniently examine these bar charts.

PRE-EXPOSED EDGE DATA

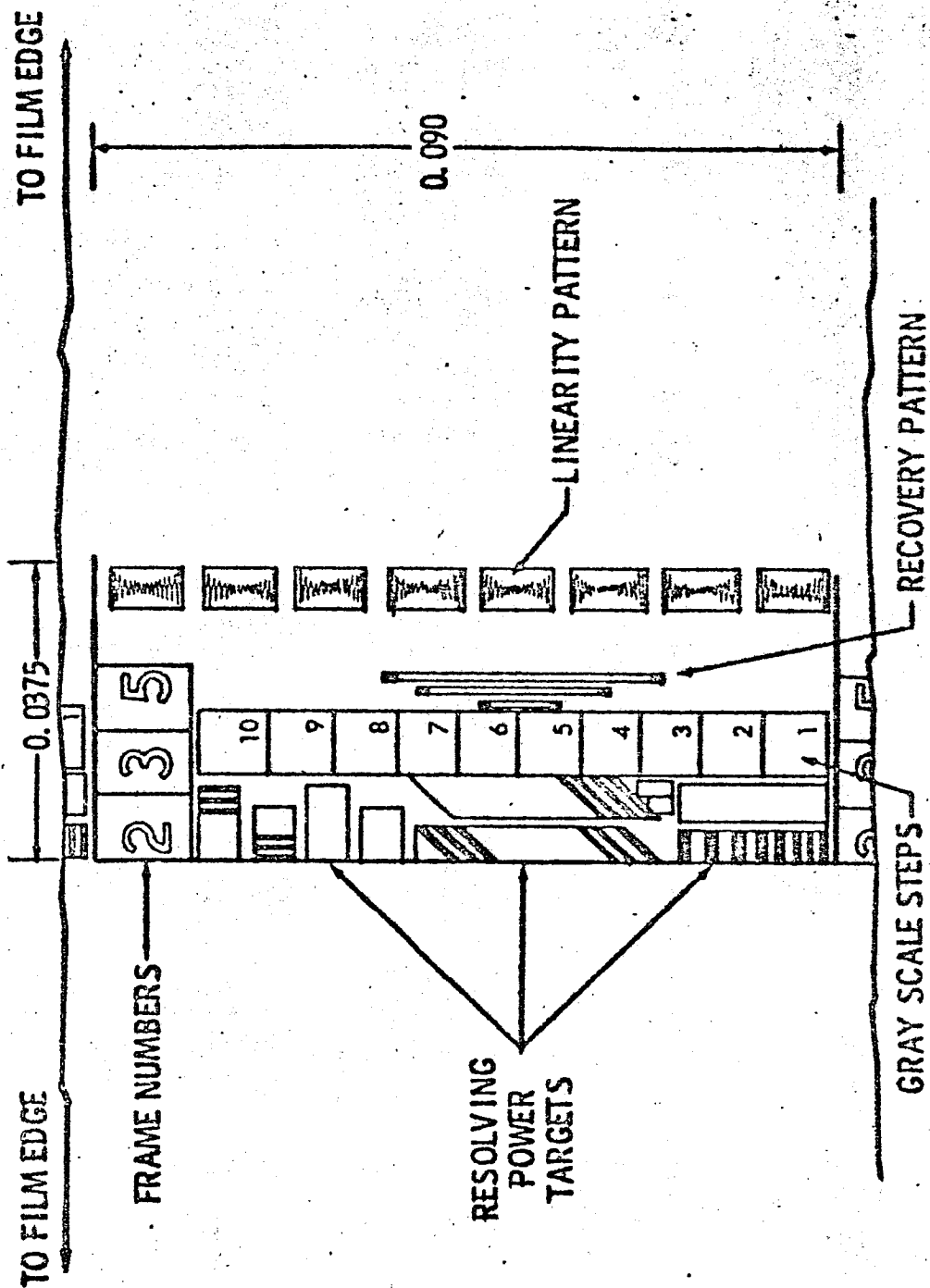


FIGURE 7.1-1. EDGE DATA FORMAT

000000

VOL
SEC

NO D2-1000293
PAGE 161

A supplementary resolving power bar chart covering the range of 180 to 1400 lines/mm is included in the format to be used in measuring the quality of the pre-exposure edge printing equipment.

7.1.2 Gray Scale

There is a requirement for a gray scale to provide data for correction in exposure which may be necessary due to lack of precise data on the albedo of the lunar surface or change in lighting conditions. This scale provides a repeatable calibration of system performance during ground tests, prelaunch checkout, during lunar approach prior to actual photography and during the active portion of the mission. The range of density levels in the picture data may be as much as 0.3 to 1.8. A ten step gray scale with approximately 0.15 change in log exposure per step has been proposed by Kodak. This will be pre-exposed in the edge data of the 70 mm film as shown in Figure 7.1-1. The density of the second step in the gray scale will be equal to the background density within ± 0.02 . The background density will equal an equivalent readout density of 0.3 ± 0.5 .

7.1.3 Linearity Marks

A precisely spaced linearity pattern is required on the spacecraft film to calibrate the horizontal linearity of the readout and reconstruction subsystems. The precision of the linearity markers should be adequate to permit measurement of any non-linearities that would significantly affect the interpretation and use of the final picture data. This is difficult to precisely specify since a specific requirement for the dimensional accuracy of the reconstructed photographs has not been set as a program requirement.

A linearity pattern of eight $.0050 \pm .0002$ by $.00925 \pm .00011$ inch bars spaced $.01125 \pm .00005$ leading edge to leading edge will be provided for each framelet throughout the entire film length. The linearity pattern lines will have a density not less than 1.5. The non-linearities of this pattern on the 70 mm film are between one and two orders of magnitude smaller than the probable non-linearities that will be introduced in the readout and reconstruction subsystem.

A film quality evaluation viewer with traversing microscope will be used to measure the linearity of the pattern on the 35 mm reconstruction film.

7.1.4 Recovery Test Pattern

A series of three bars of different lengths with their long dimension along the direction of the electronic scan will be used in checking the low frequency response of the readout and reconstruction subsystems. The density of the recovery test pattern lines will be not less than 1.5.

7.1.5 Identification

The edge data must also include serial numbers which will positively identify each scan framelet so that the frame to which it belongs and its position in the frame are known. The requirement is especially acute for cases in which noise or transmission difficulties have made much of the signal return unintelligible. The proposed Kodak format would provide a three digit number for each framelet which would permit unambiguous numbering for under 9 dual frames. The numbers then repeat.

7.1.6 Reassembly Reference

A pre-exposed reference line is required to enable accurate reassembly of the scanned framelets in the reassembly printer. This dashed line simply enables sensors in the reassembly printer to accurately position the 35 mm framelets in a vertical direction as they are projected side by side on the 9 1/2" wide reassembly film. The linearity pattern described above also serves as the reassembly reference line.

7.2 Time Track

Relative time information is required to help identify sequences and position of the photographic frames and to aid in establishing the relative position of points on the lunar surface. Due to the lack of precision in knowing position of the spacecraft in orbit and orientation of the camera, 0.1 second precision of the timing information will be more than adequate.

In the proposed system, a twenty bit code is recorded between each pair of high and low resolution frames which indicates time to the nearest 0.1 second. The 20 digit code permits time recording for a period of 29 hours before the time code repeats. For initial missions, currently contemplated, the film in the spacecraft will all be exposed within this time interval. In possible future missions, in which photography is taken over longer time intervals, there may be ambiguities in the timing information recorded unless additional digits are added to the timing code.

7.3

Telemetry Data

In addition to the data on system performance which may be derived from the picture data and the pre-exposed edge data, additional information on parameters in the photo subsystem are required at the ground sites both for purposes of diagnosing operational problems and adjusting equipment performance and for later interpretation of the photographic record. The telemetry list of the spacecraft Photo Subsystem design control specification, D2-100112, shown in Table 7.3-1, is still subject to considerable change, but indicates the scope of the required information.

The telemetry display at the DSIF site must provide the photo ground system operator with those instrumentation data which are of immediate use to him in analyzing the type and degree of adjustment required to improve or correct the received signal on a near real time basis. For example, it will be possible to command adjustments to the horizontal image size, the line scan tube focus, the photo video gain and the horizontal centering in the spacecraft scanner, to adjust the camera exposure time, or to shut down the camera or scanner readout equipment until the cause of anomolous operation has been diagnosed. Corresponding instrumentation points from the list of Table 7.3-1 should be included in the telemetry data immediately available to him. The form and location of the display to be available to the photo subsystem operator will be resolved in the detailed design of the command control and performance telemetry equipment racks.

| ITEM NUMBER | MEASUREMENT TYPE | DESCRIPTION | PRIMARY DIGITAL | ANALOG | SAMPLING RATE | TOTAL BITS | TRANSDUCER TYPE | UNIT | RANGE | ACCURACY | TELEMETRY POINT | TEST POINT | TIME OF TEST |
|-------------|----------------------|---|-----------------|--------|---------------|------------|---------------------|------------|------------|----------|-----------------|------------|--------------|
| FTL-1 | Displacement | Take-up contents | | | 2-1/2 min | 8 | Potentiometer | Feet | 0-20 | 5% | X | | 1 |
| FTL-2 | Displacement | Looper Contents (Camera) | | | 2-1/2 min | 8 | Potentiometer | Feet | 0-21 | 5% | X | | 1 |
| FTL-3 | Displacement | Looper Contents (Readout) | | | 2-1/2 min | 8 | Potentiometer | Inches | 0-18 | 5% | X | | 1 |
| CTL-5 | Rate | V/H Ratio | | | 2-1/2 min | 8 | V/H Sensor | Rad/sec | 0-26 | - | X | | 1 |
| CTL-7 | Count | Flatten Operations | X | | 2-1/2 min | 5 | Electronic Counter | Counts | 0-31 | - | X | | 3 |
| CTL-6 | Count | Shutter Operations (26") | X | | 2-1/2 min | 5 | Electronic Counter | Counts | 0-31 | - | X | | 3 |
| CTL-8 | Command Verification | V/A On-Off | X | | 2-1/2 min | 1 | Voltage Divider | State | On-Off | - | X | | 1 |
| CTL-9 | Command Verification | Camera On | X | | 2-1/2 min | 2 | Logic | Counts | 0-7 | - | X | | 3 |
| CTL-10 | Condition | Camera Program Setting | X | | 2-1/2 min | 2 | Logic | Counts | 0-7 | - | X | | 3 |
| CTL-11 | Condition | Camera Shutter Setting | X | | 2-1/2 min | 2 | Logic | Counts | 0-7 | - | X | | 3 |
| CTL-12 | Temperature | V/H Sensor | | | 2-1/2 min | 8 | Thermistor | Deg. F. | 40-160 | (5) | X | | 2 |
| CTL-13 | Temperature | Camera Temp | | | 2-1/2 min | 8 | Thermistor | Deg. F. | 40-160 | (5) | X | | 2 |
| CTL-14 | Temperature | Window | | | 2-1/2 min | 8 | Thermistor | Deg. F. | 40-160 | (5) | X | | 2 |
| CTL-15 | Command Verification | Fast/Slow Rate + Shutter Setting Advance | X | | 2-1/2 min | 1 | Bistable | State | On-Off | - | X | | 1 |
| FTL-18 | Condition | Reset Clear | X | | 2-1/2 min | 1 | Switch | State | On-Off | - | X | | 1 |
| FTL-19 | Condition | Reset Take-up | X | | 2-1/2 min | 1 | Cam. Operated Sv. | State | On-Off | - | X | | 1 |
| FTL-20 | Temperature | Processor | | | 2-1/2 min | 8 | Thermistor | Deg. F. | 40-160 | (5) | X | | 1 |
| FTL-21 | Temperature | Dryer | X | | 2-1/2 min | 8 | Thermistor | Deg. F. | 40-160 | (5) | X | | 1 |
| FTL-22 | Command Verification | Reset Out | | | 2-1/2 min | 1 | Switch | State | On-Off | - | X | | 1 |
| FTL-23 | Voltage Level | +10 VDC Converter Voltage | | | 2-1/2 min | 8 | Voltage Divider | Volts dc | 0-25 | (24) | X | | 1 |
| FTL-24 | Current | ESR Cathode Current | | | 2-1/2 min | 8 | Voltage Divider | Micro-Amps | 0-25 | (1.4) | X | | 1 |
| FTL-26 | Voltage | High Voltage Supply | | | 2-1/2 min | 8 | Voltage Divider | Volts | 0-21 Kilov | (54) | X | | 1 |
| FTL-27 | Voltage | Video Output Peak Voltage | | | 2-1/2 min | 8 | Peak Detector | Volts DC | 0-5 | (1.4) | X | | 1 |
| FTL-28 | Command Verification | Readout Electronics On or Off | X | | 2-1/2 min | 1 | Voltage Divider | State | On-Off | - | X | | 1 |
| FTL-29 | Command Verification | Video Wind Forward On | X | | 2-1/2 min | 1 | Voltage Divider | State | On-Off | - | X | | 1 |
| FTL-30 | Command Verification | Readout Drive On-Off | X | | 2-1/2 min | 1 | Bistable | State | On-Off | - | X | | 1 |
| FTL-31 | Command Verification | ECR Size and ECR Centering | X | | 2-1/2 min | 8 | Voltage Divider | Volts | 0-100 | (1.4) | X | | 1 |
| FTL-32 | Voltage Level | PM Supply Voltage | | | 2-1/2 min | 1 | Voltage Divider | State | On-Off | - | X | | 1 |
| FTL-33 | Pressure | Photo Video Gain Incr. or Decr. and Lat Focus | X | | 2-1/2 min | 8 | Humidity Transducer | PSIA | 0-5 | (5) | X | | 1 |
| FTL-34 | Relative Humidity | P/S Pressure | | | 2-1/2 min | 3 | Humidity Transducer | O/o | 40-60% | (5) | X | | 1 |
| FTL-35 | Humidity | Photo System Humidity - Lower | | | 2-1/2 min | 8 | Humidity Transducer | O/o | 40-60% | (5) | X | | 2 |
| FTL-36 | Temperature | Photo System Humidity - Upper | | | 2-1/2 min | 8 | Thermistor | Deg. F. | 40-170 | (5) | X | | 1 |
| FTL-37 | Temperature | Readout Temp. | | | 2-1/2 min | 8 | Thermistor | Deg. F. | 40-170 | (5) | X | | 1 |
| FTL-38 | Temperature | Thermal Pin Plate | | | 2-1/2 min | 8 | Thermistor | Deg. F. | 40-170 | (5) | X | | 1 |
| FTL-39 | Temperature | P/S Environment Temp. | | | 2-1/2 min | 8 | Thermistor | Deg. F. | 40-170 | (5) | X | | 1 |
| FTL-40 | Temperature | Upper Shell Temp. | | | 2-1/2 min | 8 | Thermistor | Deg. F. | 40-170 | (5) | X | | 1 |
| FTL-41 | Command Verification | Solar Eclipse On-Off | X | | 2-1/2 min | 1 | Bistable | State | On-Off | - | X | | 1 |
| FTL-42 | Condition | End of Film Supply | X | | 2-1/2 min | 1 | Switch | State | On-Off | - | X | | 1 |

* Varies with H (altitude) from 0.4% to 2%

TOTAL 114